Pressure Effects on Black Liquor Gasification

A Thesis
Presented to
The Academic Faculty

by

Christopher M. Young

In Partial Fulfillment
of the Requirements for the Degree
Doctor of Philosophy

School of Chemical and Biomolecular Engineering
Georgia Institute of Technology
August 2006

Pressure Effects on Black Liquor Gasification

Approved by:

Dr. W.J. Frederick Jr.
(ChBE), Adviser

Dr. Kristiina Iisa
(ChBE), Adviser

Dr. Scott Sinquefield
(IPST)

Dr. Tim Patterson
(ME)

Dr. Pradeep Agrawal
(ChBE)

Dr. H. Jeff Empie
(ChBE)

Date Approved: June 28, 2006

...faith is being sure of what we hope for and certain of what we do not see.

Hebrews 11:1 (NIV)

To my wife,

Sara Ann,

who has stuck with me through thick and thin.

ACKNOWLEDGEMENTS

First, I thank God for shepherding me through this chapter in my life. There were many times when the odds seemed insurmountable, but God remained faithful and guided me through the trials.

There are many people who have directly and indirectly helped me in the successful completion of this work. I gratefully acknowledge the support of my advisers, Drs. Jim Frederick and Kristiina Iisa. Their experience and knowledge in the area of black liquor gasification consistently humbled me, yet challenged me to learn more. The technical expertise of Dr. Scott Sinquefield and Alan Ball is also gratefully acknowledged. I am very grateful to Dr. Arnold Stancell for his time and effort during my first semester at Georgia Tech. Major Hank White has been a good friend by always being ready to listen and offer conversation.

I would also like to thank my family, especially my parents. Their advice and wisdom have greatly contributed to what I have done here.

Most importantly I want to acknowledge the support of my wife. Not only has she has talked me down off the roof countless times, but she has kept the rest of our life in order while I have focused on this project. I could not have done this without her.

TABLE OF CONTENTS

LIST OF TABLES

LIST OF FIGURES

LIST OF ABBREVIATIONS

AES   Atomic Emission Spectroscopy.

B&W   Babcock and Wilcox.

CPPA   Canadian Pulp and Paper Association.

EFR   Entrained Flow Reactor.

ICP   Inductively Coupled Plasma.

ID   Inner Diameter.

IPST   Institute of Paper Science and Technology.

LIW   Loss In Weight.

MTCI   Manufacturing & Technology Conversion International, Inc.

NIST   National Institute of Standards.

NLM   Normal Liters per Minute (0^oC).

OD   Outer Diameter.

PDTF   Pressurized Drop Tube Furnace.

PEFR   Pressurized Entrained Flow Reactor.

PTGA   Pressurized Thermogravimetric Analysis.

SEM   Scanning Electron Microscope.

TAPPI   Technical Association of the Pulp and Paper Industry.

TGA   Thermogravimetric Analysis.

UIC   Universal Instruments Corporation.

XRD   X-ray Diffraction.

SUMMARY

Gasification of black liquor is an alternative to the combustion of black liquor, which is currently the dominant form of chemical recovery in the paper industry. Gasification of black liquor offers the possibility of higher thermal efficiencies than combustion, reducing manufacturing costs and creating new revenue streams through a forest biorefinery. Pressurizing the gasification reactor further enhances the efficiency advantage of gasification over combustion.

This study uses a pressurized entrained flow reactor (PEFR) to study black liquor gasification behavior under pressures, temperatures, and heating rates similar to those of next-generation high-temperature black liquor gasifiers. The effects of pressure on black liquor char morphology, gasification rates, pyrolysis carbon yields, and sulfur phase distribution were studied. These characteristics were investigated in three main groups of experiments at 900°C: pyrolysis (100% N_2), gasification with constant partial pressure (H_2O and CO_2), and gasification with constant mole fraction (10% CO_2, 2% H_2O, 1.7% CO, 0.3% H_2) under five, ten, and fifteen bar total pressure.

It was found that pressure had an impact on the char physical characteristics immediately after the char entered the reactor. Increasing pressure had the effect of decreasing the porosity of pyrolysis chars. Pressure also affected particle destruction and reagglomeration mechanisms. Surface areas of gasification chars decreased with increasing pressures, but only at low carbon conversions.

The rate of carbon conversion in gasification was shown to be a function of the gas composition near the particle, with higher levels of inhibiting gases slowing carbon conversion. The same phenomenon of product gas inhibition observed in gasification was used to explain carbon conversions in pyrolysis reactions.

Sulfur distribution between condensed and gas phases was unaffected by increasing total

pressure in the residence times investigated. Significant amounts of sulfur are lost during initial devolatilization. With water present this gas phase sulfur forms H_2S and does not return to the condensed phase.

CHAPTER I

INTRODUCTION

Mankind has been producing paper-like materials for thousands of years. The Chinese used the inner bark of mulberry trees as a source of pulp, while Egyptians used papyrus reeds as a feedstock for their paper. By the time people began settling North America paper mainly came from the alkaline digestion of old cotton rags. The first paper mill in the United States was opened in Germantown, Pennsylvania in 1690 [7].

Modern paper making derives its fiber almost exclusively from trees via some type of pulping process. In pulping, individual cellulose fibers are obtained from the tree or other cellulose source, where the fibers exist in a matrix of cellulose and lignin. Lignin consists of complex organic molecules that exist in and between individual cellulose fibers in vegetable matter and serves to hold the cellulose together.

A variety of pulping processes exist which use mechanical energy, chemical reactions, or a combination of both to produce pulp. An extreme example of mechanical pulping is stone ground wood pulping, which works by pushing a tree into a rotating stone with ribs grooved in its side. At the chemical end of the spectrum dissolving pulps are produced in which 60-70% of the initial mass of the tree is dissolved, leaving only pure cellulose behind. This pulp is then used in a variety of products from imitation crab meat to screwdriver handles. A summary of different types of pulping processes is shown in Table 1.

Generally, mechanical pulps have higher yields than those produced by chemical means. Mechanical pulps are subject to color reversion, which means they darken over time or when exposed to light. This is due to the fact that the mechanical pulping process does not remove lignin from the fiber. Mechanical pulps tend to have lower strength and higher opacity than chemical pulps.

Chemical pulps have lower yields than mechanical pulps due to the dissolution of lignin and hemicelluloses by the pulping chemical. Chemical pulps are darker than mechanical

1

Table 1: Pulping method comparison [7, 71]

Classification	Pulping Method	Yield %	Uses	Examples
Mechanical	mechanical, thermal	85-95	newsprint, magazines, books	groundwood, thermo-mechanical
Hybrid	mechanical, thermal, chemical	55-85	corrugated medium	neutral sulfite semi-chem, chemi thermo-mechanical
Chemical	thermal, chemical	40-55	tissue, linerboard, fine paper	kraft, sulfite, soda

pulps and must be bleached more to achieve the same brightness. Bleaching removes any lignin still left on the fiber after the pulp cook, which results in the fiber being resistant to color reversion. Chemical pulps are generally stronger than mechanical pulps, with pulp generated by the kraft chemical process being the strongest.

Of the different methods of chemical pulping, the kraft process is dominant. In kraft pulping, NaOH and Na_2S are used to dissolve lignin in the pulper. The NaOH acts as a pulping agent, dissolving lignin, cellulose, and hemicelluloses. A secondary function that the NaOH serves is to swell the wood chips, increasing their accessibility to the pulping chemicals. The Na_2S is also a pulping agent that much more selectively attacks lignin than the NaOH. There has been extensive research regarding the best ratio of Na_2S to NaOH for use in kraft cooking with respect to yield, lignin content, pulp strength, and other factors. Some of these studies are outlined in Volume 5 of the CPPA's Pulp and Paper Manufacture series [28].

1.1 Kraft Chemical Recovery

One of the most important aspects of kraft pulping is the chemical recovery cycle, which allows for the recovery and reuse of the pulping chemicals needed for the process. Without the ability to recover these chemicals the cost of manufacturing would be prohibitively high. Table 2 outlines the major processes, components, and chemical reactions involved in the kraft chemical recovery process.

Table 2: Kraft recovery process

Process	Components	Chem. Reactions	Description
Pulping	white liquor, wood chips	NaOH + Na$_2$S+ wood $\longrightarrow$ pulp + black liquor	Pulping chemicals (white liquor) react with wood chips and solubilize lignin. Resultant solution is called black liquor.
Combustion	black liquor, heat	black liquor + O$_2$ $\longrightarrow$ CO$_2$ + H$_2$O+ Na$_2$CO$_3$ + Na$_2$S	Organics in black liquor are combusted, producing heat. Inorganic chemicals remain as Na$_2$CO$_3$ and Na$_2$S, called smelt.
Smelt Dissolving	smelt, water		Smelt added to water to produce green liquor
Causticizing	green liquor, lime	Na$_2$CO$_3$ + H$_2$O + CaO $\longleftrightarrow$ 2NaOH + CaCO$_3$	Reversible reaction between lime (CaO) and sodium carbonate to produce sodium hydroxide. This produces white liquor, which is reused in the pulpers.
Calcining	lime mud, heat	CaCO$_3$ + heat $\longrightarrow$ CaO + CO$_2$	Heat is added to lime mud (CaCO$_3$), driving off carbon dioxide and regenerating lime for reuse in causticizing.

After pulping the combination of dissolved organics and spent pulping chemicals are called black liquor. The black liquor is separated from the pulp fibers in washers located after the pulpers. Due to the high volume of water needed to wash the pulp, the solids content of the black liquor is too low for direct combustion. Therefore, the black liquor goes through a series of evaporators in order to remove water and concentrate the solids for combustion. The combustion reaction (shown in equation 1) is highly exothermic.

$$C_xH_y + (x + 1/4y)O_2 \longrightarrow xCO_2 + y/2H_2O \tag{1}$$
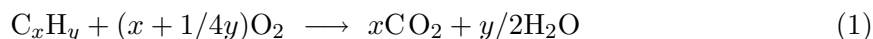
Combustion of black liquor occurs in a recovery boiler, shown in Figure 1. Black liquor at greater than 65% solids is sprayed into the boiler from its sides. The organic portion of the black liquor combusts very quickly, which provides the heat for the boiler. The hot combustion gases then travel up and across a series of heat exchangers which generate high pressure (up to 100 bar) steam. This steam is then used to generate electricity in a turbine. Low pressure steam (approximately 20 bar) from the exhaust of the turbine is then used in other parts of the mill, such as steam drying cans and pulpers.

The inorganic products which remain after the organics are combusted fall downward in the boiler. These inorganic salts are collectively referred to as smelt and consists mainly of Na_2S, Na_2SO_4, and Na_2CO_3. The residence time of the smelt is controlled by the smelt bed height, with smelt removal coming from the bottom of the bed. As the sulfate ions move from the surface of the smelt bed to the interior, reduction of $SO_4{}^{2-}$ to S^{2-} occurs. The smelt must remain in the reactor long enough in order for this reduction reaction to occur so that the Na_2S can again be used in the white liquor.

After the smelt leaves the boiler it is added to water and cleaned either in a filter or clarifier. The resultant solution is called "green liquor" and consists primarily of Na_2S, Na_2CO_3, and water. In order to regenerate the caustic necessary for pulping, lime (CaO) is added to the green liquor in a stirred tank reactor called a slaker. The slaking reaction is an equilibrium reaction between the lime and sodium carbonate, shown in equation 2.

$$Na_2CO_3 + CaO + H_2O \longleftrightarrow 2NaOH + CaCO_3 \tag{2}$$
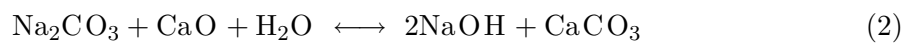
The slaking reaction forms sodium hydroxide and calcium carbonate, a precipitate. The
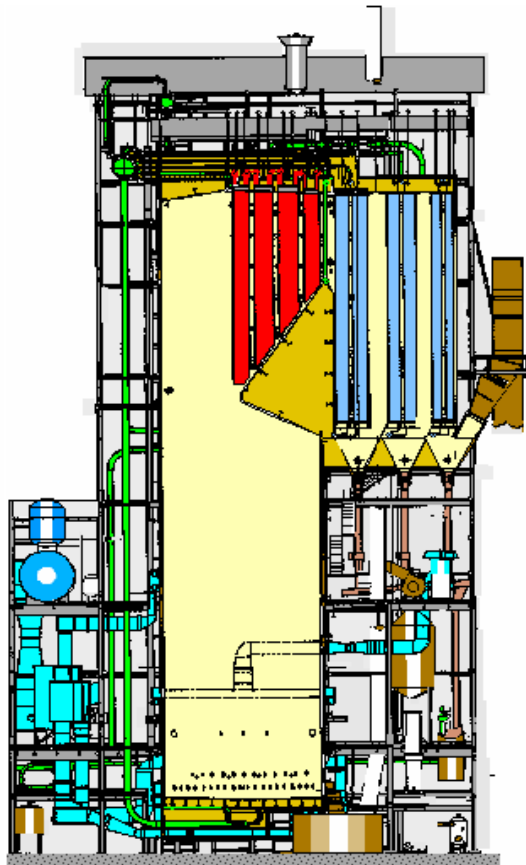
Figure 1: Black liquor recovery boiler
Source: Jaakko Poyry

liquor is once again processed to remove $CaCO_3$, after which it is again called white liquor. The white liquor is then reused in the pulpers.

The solid calcium carbonate is then further processed to regenerate the lime used in the slaking reaction. This reaction, shown in equation 3, regenerates lime by heating the calcium carbonate to high temperatures in a lime kiln, driving off CO_2.

$$CaCO_3 \xrightarrow{heat} CaO + CO_2 \qquad (3)$$

The heat for this reaction is typically provided by the combustion of fossil fuels.

There are several limitations of the traditional kraft recovery process. Pressure drops across the power turbine are not as great as those common in electrical generating plants due to the necessity of using the exhaust steam at other places in the mill. This need results in relatively small amounts of electricity and excess thermal energy being produced in recovery boilers. Calcination requires the combustion of fossil fuels in the lime kiln to provide the heat necessary to drive off carbon dioxide from the carbonate. Recovery boilers need water cooled walls to prevent corrosion from the smelt. Leaks in the water tubes can cause smelt explosions that destroy boilers. Recovery boilers are also very capital intensive, with new boilers costing hundreds of millions of dollars. These shortcomings, along with others, of the traditional recovery process have caused people to look for alternative methods for many years.

1.2 Alternative Recovery Methods

Several chemical recovery alternatives have been investigated over the years in an attempt to overcome the previously mentioned shortcomings of the black liquor recovery boiler. In an excellent paper by Whitty and Verrill [92], twenty of these concepts are reviewed. The authors placed the concepts into four broad categories, namely:

- Solid phase-non gasification

- Liquid phase coking

- Low temperature gasification

- High temperature gasification

The solid phase non-gasification processes typically consisted of fluidized bed reactors operated at temperatures below the melting points of the inorganic salts in the black liquor, with the liquor either combusted or pyrolyzed. The liquid phase coking processes work by pumping low solids black liquor to very high pressure and pyrolyzing them at elevated temperatures in a reactor. This generates a combustible gas, a liquid phase that contains the pulping chemicals, and a solid phase of carbon that can be combusted or converted to activated carbon. Due to various problems the non-gasification processes were viewed as being non-competitive with recovery boilers and abandoned by the early 1980's.

Gasification is a technology in which substoichiometric amounts of oxygen are added to a carbon source with the intention of generating a gas. The oxygen source is typically air, oxygen, or steam. The gasification reactions that occur are shown in equations 4 and 5.

$$C_s + CO_2 \longrightarrow 2CO \tag{4}$$

$$C_s + H_2O \longrightarrow CO + H_2 \tag{5}$$

The gas generated by these reactions has a high concentration of hydrogen and carbon monoxide. Depending on the final use this gas is referred to as fuel gas or synthesis gas. If the gasification gas is combusted (in a boiler or turbine, for example) it is referred to as fuel gas. If the gas is used a a building block for further chemicals it is referred to as synthesis gas, or syngas.

Development of low-temperature black liquor gasifiers began in the mid 1980's and continues today [92]. The low temperature process that is closest to commercialization is one developed by MTCI. A schematic of their gasifier design is shown in Figure 2. In the MTCI gasifier, black liquor is sprayed onto a fluidized bed that is fluidized by steam. This fluidization steam also serves as the oxygen source for gasification. The process runs at approximately 600^oC, with its temperature being limited by the melting point of the bed solids. Particle residence time in the reactor is on the order of 50 hours. Bed solids are removed from the bottom of the reactor and combined with water to generate green liquor.

The product gas travels through a cyclone to remove any entrained particulates. It is then combusted in a pulse combuster, with the heat being transferred into the fluidized bed via tube banks that run through the reactor.
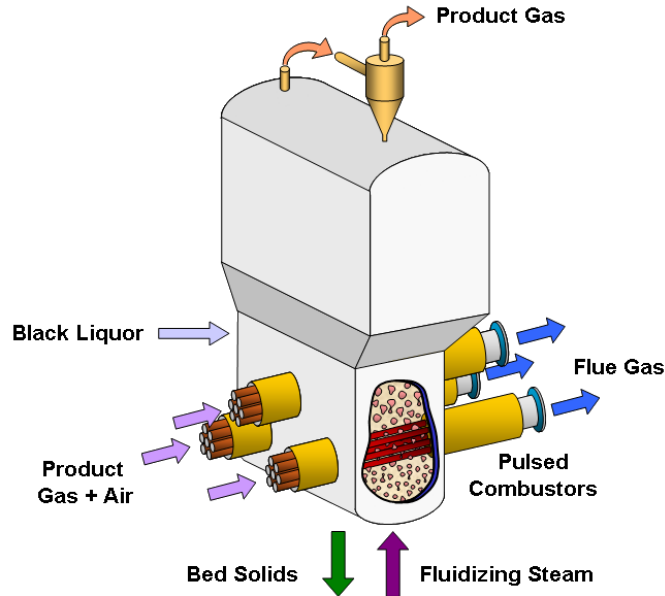
Figure 2: Fluidized bed black liquor gasifier
Source: MTCI

There are currently two reactors of the type shown in Figure 2 in full scale operation. Neither installation, however, is in a kraft mill. Development of the technology is ongoing as operational challenges are identified and overcome. Significant issues that are currently being investigated with this technology revolve around the production of tars and suitable materials for the pulse combustors.

High temperature gasification has been investigated since the early 1960's by a wide range of companies [92]. As with the low temperature gasification route, development continues today, with the main design developed by Chemrec. The Chemrec gasifier (shown in Figure 3) is an entrained flow gasifier, with the liquor being injected axially from the top of the reactor. Atomization steam is added to the liquor, and substoichiometric amounts of air are added either tangentially or axially with the liquor. At the top of the reactor the black liquor combusts with the oxygen present from the air, providing heat, CO_2, and H_2O for the endothermic gasification reactions. As the liquor travels away from the top
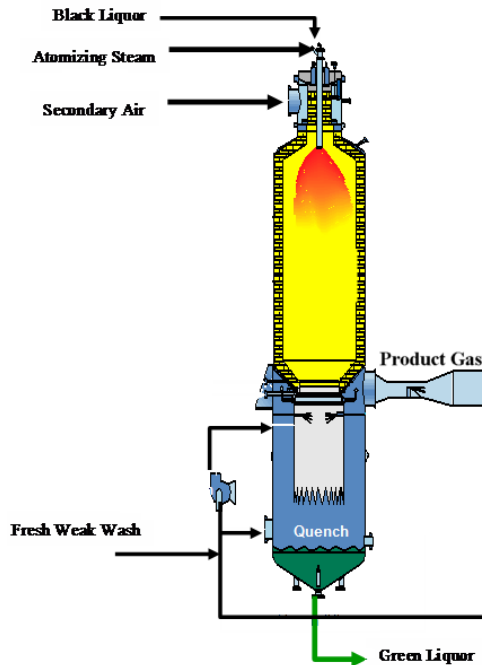
Figure 3: Entrained flow black liquor gasifier
Source: Weyerhaeuser

of the reactor the free oxygen is consumed and gasification with the combustion products begins. Operating temperatures are around 950^oC, and residence times for the liquor are on the order of two seconds. The smelt that is left over from the gasification passes through the bottom of the refractory-lined upper section of the reactor and into a quench zone, where it is combined with water to form green liquor. The product gas exits the reactor tangentially at the bottom of the refractory zone and is cleaned prior to combustion.

Weyerhaeuser has been operating an atmospheric pressure, air blown reactor of the type shown in Figure 3 for several years at a kraft mill in North Carolina. The major operational issue with this technology so far has been materials-related. Due to the fact that the operating temperature of this gasifier is 300^oC above the melting temperature of the salts in the black liquor, they are able to penetrate the refractory that lines the upper section of the reactor. Freezing of the salts inside the refractory causes spalling and loss of the liner over time. Considerable effort is currently underway to identify suitable materials for this application.

1.3 Pressurized Black Liquor Gasification

Pressurizing the gasification reactor has several advantages, from operational to capital. Since a black liquor gasifier has two products, syngas and green liquor, its pressurization creates problems unique from coal or biomass gasification, which only have to produce a syngas.

From a capital expense perspective, increasing the pressure inside the gasifier could significantly decrease material costs. The current black liquor gasifiers that are installed in North America operate at slightly over atmospheric pressure. Due to the low concentration of gases at this pressure, the size of these reactors must be large in order to have sufficient residence time for the reactions. This contributes to thermal inefficiency due to convective heat loss from the reactors as well as increased capital costs from the additional materials needed. While additional material would be required for increasing the thickness of the reactor walls to contain the pressure, the overall volume could potentially be greatly reduced by pressurizing the reactor, depending on the effects of pressure on gasification kinetics. Carbon gasification rates are positively related to the pressures of the reactant gases in equations 4 and 5 and negatively related to the pressures of the product gases. These reactions have been observed to exhibit Langmuir-Hinshelwood type behavior [37, 38, 39, 57], with the currently accepted rate expressions for equations 4 and 5 shown in equations 6 and 7 respectively,

$$-r = \frac{K_1[\mathrm{CO_2}]}{[\mathrm{CO_2}] + K_2[\mathrm{CO}]} \tag{6}$$

$$-r = \frac{K_3}{1 + \frac{K_4[\mathrm{H_2}]}{[\mathrm{H_2O}]} + K_5[\mathrm{CO}]} \tag{7}$$

where $-r$ is the rate of carbon loss due to gasification and K_1 through K_5 are constants. Depending on the relative value of the constants in equations 6 and 7, the rate of carbon gasification can either go up, down, or remain the same with increasing pressure. Currently very little is understood regarding the effect of pressure on gasification rate, especially at higher temperatures.

In order for the syngas to be combusted or used as a building block for further chemicals it must be under pressure. If the gasifier is pressurized, the only work needed is to pressurize

a relatively small amount of cool oxidizing gas. If the point of pressurization is after the reactor, however, not only is the syngas hot after leaving the gasifier, but a much greater total number of moles of gas needs to be pressurized due to the creation of gases via equations 4 and 5. The larger number of moles and higher gas temperatures combine to greatly increase the volume required for compression. This results in a significant energy penalty for pressurizing after the gasifier.

An additional concern particular to black liquor gasification is the phase distribution of sulfur. In the presence of water and carbon dioxide the form of sulfur at equilibrium is dictated by equation 8 [48].

$$Na_2S + CO_2 + H_2O \longleftrightarrow Na_2CO_3 + H_2S \tag{8}$$

In equation 8, two moles of gas on the left are in equilibrium with one mole of gas on the right. Increasing the pressure of this equilibrium will have the effect of shifting it to the right via Le Châtelier's principle. As can be seen, shifting the equilibrium of equation 8 to the right has the added consequence of forming more carbonate. This additional carbonate must be removed at significant cost in the lime kiln . Currently little is understood about the impact of pressure on the reaction of sulfur in pressurized black liquor gasification.

CHAPTER II

LITERATURE REVIEW

2.1 Alkali Catalysed Carbon Gasification

Research interest in alkali catalyzed coal char gasification swelled in the late 1970s and early 1980s. Several mechanisms for the alkali catalysis of coal char were suggested during this time, many of which are outlined in a review paper authored by Wood and Sancier in 1984 [93]. Common among most of these mechanisms was the presence of a metal-oxygen-carbon complex which increased the rate of carbon gasification.

Freek Kapteijn and Jacob A. Moulijn were responsible for a body of work in the mid 1980s [37, 38, 39, 57] that suggested a fairly simple, two step mechanism was responsible for the alkali catalyzed gasification of carbon. In the mechanism, an alkali metal oxide is oxidized by an oxygen containing gas and then it donates the extra oxygen to a carbon atom fixed in the matrix, producing CO.

$$CO_2 + M_xO_y \longleftrightarrow CO + M_xO_{y+1} \tag{9}$$

$$M_xO_{y+1} + C_f \longrightarrow M_xO_y + CO \tag{10}$$
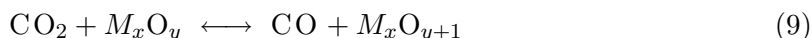
Variations on this mechanism, in which either the CO in equation 10 was immediately released to the gas phase or remained adsorbed on the carbon matrix and later released, were also introduced.

$$CO_2 + M_xO_y \longleftrightarrow CO + M_xO_{y+1} \tag{11}$$

$$M_xO_{y+1} + C_f \longleftrightarrow M_xO_y + (CO) \tag{12}$$

$$(CO) \longrightarrow CO \tag{13}$$
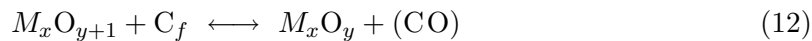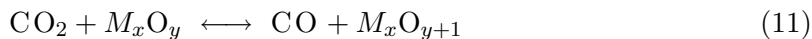
The major advantage of this mechanism was that it could be used to explain the catalytic effect with CO_2, H_2O, or O_2 as the reaction gas.

In the early 1990s Meijer, working with Kapteijn and Moulijn, developed a more complex mechanism involving active sites, oxidized active sites, and CO_2 chemisorbed sites, which was capable of explaining experimental data for CO_2 as well as H_2O gasification [52, 53]. This more complex mechanism accounted for the detrimental effects of H_2 and CO on the gasification rate and has become the accepted mechanism for carbon gasification.

$$H_2O + * \longleftrightarrow H_2 + O^* \tag{14}$$

$$CO + O^* \longleftrightarrow CO_2^* \tag{15}$$

$$CO_2^* \longleftrightarrow CO_2 + * \tag{16}$$

$$O^* + C_f \longleftrightarrow C(O) + * \tag{17}$$

$$C(O) \longrightarrow CO \tag{18}$$

2.2 Black Liquor Gasification

Li and van Heiningen conducted early research in black liquor gasification using thermogravimetric analysis (TGA) [45, 46]. They showed that CO_2 and H_2O gasify black liquor char orders of magnitude faster than Na_2CO_3 impregnated activated carbon. They also noted that the molecular ratio of sodium to carbon in black liquor was much higher than the optimal ratio for gasification rate in alkali-catalyzed carbon. Using a scanning electron microscope (SEM) and energy dispersive scanning, they showed that black liquor has atomically dispersed sodium throughout the carbon matrix. This resulted in faster gasification than the catalyst doped carbon, where the active sites tended to be located on the internal surface of the carbon matrix. Black liquor was also dried using two different techniques, one of which resulted in segregation of the black liquor solids into an organic-rich upper portion and an inorganic rich lower portion. This segregated black liquor gasified at a slower rate than the non-segregated black liquor due to its uneven distribution of sodium, further underscoring the importance of sodium distribution. Gasification of black liquor by CO_2 and H_2O were mechanistically explained using Langmuir-Hinshelwood kinetics, utilizing the

two step mechanism shown in equations 9 and 10. Activation energies were shown to be 250 kJ/mol and 210 kJ/mol for CO_2 and H_2O, respectively.

Frederick and Hupa [19, 20] expanded the body of knowledge for black liquor gasification by using a pressurized TGA (PTGA), thereby allowing partial pressures of gases to exceed atmospheric. CO was found to strongly inhibit the rate of gasification. Results with CO_2 gasification at up to 30 bars total pressure showed a significant (4-6x) decrease in gasification rate with constant CO/CO_2 ratio and increasing total pressure. Gasification rate was found to be related to CO_2 concentration to the 0.88 power, and activation energy for CO_2 gasification was shown to be 205 kJ/mol at 20 bars. Most significantly, the mechanism proposed by Li and van Heiningen [45] did not hold true for higher pressures. When rates of gasification were plotted as a function of P_{CO}, rates measured in this study deviated significantly from the extrapolated rate curve of Li and Van Heiningen. This indicated that either a more complex mechanism was required for gasification, or more than one variable was changing during the experiments.

Another study by Frederick and Hupa [18] detailed single drop gasification characteristics at atmospheric pressure in a natural convection furnace. Cameras recorded the diameter of the droplet as a function of gasification time, and it was shown that black liquor swelled by a factor of 3 or greater when gasified under CO_2 or H_2O. Swelling factor did not seem to be largely effected by initial particle diameter or temperature. Due to the relatively large (3mm) initial diameter of the black liquor droplets, only the experiments conducted at 700°C were shown to be kinetically limited. Higher temperatures resulted in increased reaction rates, and intra particle diffusion and film mass transfer resistances became significant. At 700°C, time to complete gasification by H_2O was almost three times shorter than that by CO_2, indicating a higher rate. At higher temperatures the ratio of times for complete gasification with water vapor versus CO_2 at the same partial pressures approached the difference in relative diffusivities.

Application of the three-site mechanism described in equations 14 through 18 was performed by Frederick et al.[25] in an attempt to explain CO_2 gasification of black liquor char at elevated pressures. From PTGA experiments conducted at 700°C it was determined

14

that gasification increased with P_{CO_2} to the 0.88 power up to approximately 10 bars, then became independent of P_{CO_2}, indicating a saturation of catalyst sites. Again, the presence of CO showed a strong inhibitory effect on gasification rate. Using the assumption that the reaction of the oxygen radical site with fixed carbon was the rate limiting step in the mechanism, a rate equation was established. While all constants in the rate equation were positive for all conversion points in the data, there was a strong dependence of the constants on the degree of conversion. The dependency of the constants on the degree of conversion implied that either the number of active catalyst sites or active carbon sites change with conversion.

Whitty et al. applied the three site mechanism to steam gasification of black liquor [90]. Using a PTGA and black liquor char produced at atmospheric pressure, Whitty ran experiments at up to 30 bar total pressure and between 600 and 675°C. CO and H_2 were found to inhibit the rate of gasification, with CO having a stronger effect. The rate of gasification of steam was found to be of order 0.56 with respect to P_{H_2O}, which was less than the 0.88 order found for CO_2 in previous studies. As shown before, at the same conditions (total pressure and molar concentration of oxidizing gas) steam gasification was found to be several times faster than CO_2 gasification. The data produced in this study were evaluated with eight different gasification rate expressions. The expression based on Meijer's mechanism provided the best fit. However, the expression still did not account for the decrease in rate as total pressure increased.

The first attempts at determining pressurized black liquor gasification rates with both CO_2 and H_2O as reaction gases occurred at Abo Akademi University [87, 88]. Using statistically designed experiments, Whitty et al. obtained an empirical expression for pressurized black liquor gasification as a function of CO_2, H_2O, CO, and H_2 partial pressures. Experiments were conducted to see if the reaction gases were coming to equilibrium via the water gas shift reaction prior to reaching the char, with the results indicating that they were not. A six-term empirical rate equation (with rate units of sec^{-1} and pressure in bar) was generated:

$$rate(\times 10^4) = 3.312 + 1.157 P_{H_2O} + 0.07119 P_{CO_2}^2 - 2.943 P_{H_2} - 3.869 P_{CO} + 0.6595 P_{CO}^{-1} \quad (19)$$

Interestingly, this equation predicts that at fixed gas composition gasification rate goes through a minimum and eventually increases with total pressure.

Overacker et al. [62] applied a mechanistic approach based on the Meijer mechanism to the data that was generated by Whitty et al. in the combined CO_2/H_2O study [87, 88]. As was found in Frederick et al. [25], a strong dependence of the rate equation constants on carbon conversion was found. Modifications to Meijer's equation were made to account for water gas shift equilibrium, but ultimately it was found that using unshifted gas concentrations to evaluate kinetic parameters provided the best results.

2.3 Pressure Effects on Black Liquor Gasification

Verrill et al. [78] investigated the effects of sodium concentration on pyrolysis yield, char composition, sodium loss during pyrolysis, and gasification rates for synthetically prepared black liquor. Gasification rates for the synthetic liquors were also compared with those for industrial liquor. Results from the study indicated that increasing sodium content resulted in decreased mass volatilized during pyrolysis and decreased total carbon in the char during gasification. Carbonate was found to increase with increasing liquor sodium content during gasification. A maximum rate was found at Na/C molar ratio of 0.3 for the synthetic liquors, after which gasification rates decreased with increasing Na/C molar ratio. Verrill et al. also determined that the conditions during pyrolysis strongly influenced the reactivity of the char, with increasing pressures decreasing reactivity.

The effects of pyrolysis conditions on char characteristics was investigated by Whitty and Sandelin [91], and are summarized in Table 3.

Table 3: Effect of pressure, temperature, and time on char physical characteristics

Condition	Swelling	Volatiles Yield	Gasification Rate fixed gas %
↑ Pressure	↓	No Effect	↓
↑ Temperature	No Effect	↑	Not Determined
↑ Time	No Effect	↑	Not Determined

This report also introduced the idea that the conditions prior to gasification have a

major impact on the gasification rates measured. Pyrolyzed samples were exposed to 10% CO, 90% N_2 at 1 and 20 bars and then separately gasified at 1 and 20 bars. The pressure at which the sample was heat treated had more impact on the gasification rate than the pressure at which gasification took place.

As described by Whitty et al. [89] and Saviharju et al. [68], the presence of CO prior to gasification in the PTGA studies resulted in surface changes in the char. Samples were brought to temperature under N_2 and CO in order to reduce the carbothermic degradation of sodium carbonate and subsequent sodium loss by shifting the equilibrium of the following equations to the left.

$$Na_2CO_3 + 2C \longleftrightarrow 2Na + 3CO \tag{20}$$

$$Na_2CO_3 + C \longleftrightarrow 2Na + CO + CO_2 \tag{21}$$
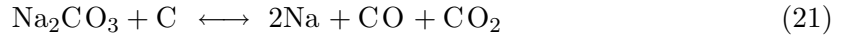
However, the presence of CO had the unintended consequence of depositing carbon on the surface of the black liquor char through the Boudouard reaction.

$$C + CO_2 \longleftrightarrow 2CO \tag{22}$$

While the mass of the deposited carbon layer was small when compared with the overall mass of the samples, it contained no alkali catalyst, resulting in much slower gasification than for the black liquor char without deposited carbon. This uncatalyzed carbon layer was deposited over the catalyst sites and significantly contributed to the overall increased gasification time of the material. Increasing the pressure resulted in more soot being deposited and slower gasification rates, especially at the beginning of the high pressure gasification runs. This effect can be seen in the pressurized gasification rate curves plotted as a function of conversion. The gasification rates are slow at the beginning and go through a maximum before declining again. As the catalytic sites were exposed, the rate of gasification increased until the amount of fixed carbon became the limiting effect, and the rates began to decrease. Li and van Heiningen did not observe this parabolic rate vs. conversion curve because at atmospheric pressures the partial pressure of CO was low enough to deposit

negligible amounts of carbon on the catalyst sites.

2.4 Sulfur Release During Black Liquor Pyrolysis and Gasification

Harper conducted an investigation in the late 1980s regarding the release of sulfur during pyrolysis of kraft black liquor [30]. Black liquors were prepared and black liquor drops were pyrolyzed in a reactor at temperatures between approximately 300 and 750°C. Sodium sulfide and sodium thiosulfate released up to 40% of their sulfur to the gas phase, while sulfites and sulfates released very little of their sulfur. Thiosulfates also released their sulfur, but at a slower rate than sulfide.

A sulfur release model was generated as part of Harper's thesis and further elaborated on by a group at the IPST [29]. Measurements were conducted of the percentage of sulfur released from pyrolysis of sulfide and thiosulfate which showed a maximum in sulfur release from these species near 500°C. The sulfur model showed that while thiosulfate and sulfide had the same peak temperature with regard to percentage sulfur release, the sulfide had a more narrow sulfur release peak with respect to temperature.

The findings of Harper were consistent with a previous study by Cameron and Grace [10] in which the reduction of sulfate in black liquor char was investigated. The extent of sulfate reduction in a mixture of black liquor char, K_2CO_3, Na_2CO_3, and Na_2SO_4 was quantified by the amount of CO_2 and CO released at 760°C. It was found that sulfate reduction was first order with respect to the amount of carbon remaining in the char. A Langmuir-Hinshelwood expression was derived for the rate using a mechanism similar to alkali-catalyzed carbon gasification. The sulfate was reduced slowly, with CO_2 continuing to be evolved for 10 minutes after the reactor had reached the desired temperature. These times were much longer than those modeled by Harper et al. [29], corresponding to their finding that sulfate lost very little sulfur during pyrolysis. Once the sulfate was reduced to sulfide, however, sulfur release could occur.

Sricharoenchaikul et al. performed a study on the transformation of sulfur species during rapid atmospheric pyrolysis of kraft black liquor [72, 75]. Both condensed and gas

phase sulfur species were determined as a function of black liquor residence time in a laminar entrained flow reactor at temperatures between 700 and 1100°C and residence times from 0.3 to 1.7 seconds. Thiosulfate was found to disappear quickly at all temperatures. Sulfite was not present in the original liquor and was thought to be produced from the decomposition of thiosulfate through reaction 23.

$$Na_2S_2O_3 \longrightarrow Na_2SO_3 + S \qquad (23)$$

The sulfate concentration of the char stayed constant at residence times up to 1.7 seconds at 700°C due to the slow reduction of sulfate (as shown by Cameron and Grace [10]). After 700°C, however, increasing the temperature increased the rate at which sulfate was reduced in the char. A slight increase in char sulfate was seen at high residence times and higher temperatures, but it was attributed to reoxidation of sulfide while handling the sample.

The gas phase sulfur species investigated in Sricharoenchaikul's work included H_2S, COS, SO_2, CS_2, and organosulfur species (various mercaptans). The organic sulfur gases were found to be the dominant gas phase species present, accounting for up to 60% of total sulfur at some conditions. The mercaptan concentrations were found to reach a peak and then to decrease again, reflecting the fact that they are transient species and not thermodynamically stable at these temperatures. Increasing the temperature reduced the time at which this peak occurred. At 700°C the maximum occurred after the last residence time of 1.7 seconds, while at 1100°C the maximum occurred before the first time of 0.3 seconds.

Hydrogen sulfide was also a major component of the gas phase sulfur, accounting for over 20% of the sulfur at some data points. As with the organic sulfur gases, increasing the temperature decreased the time at which maximum concentration of H_2S was detected. At 1000 and 1100°C the maximum concentration of H_2S was found at the first data point, meaning that the maximum concentration likely occured prior to 0.3 seconds.

Other sulfur species measured in the gas phase included CS_2, COS, and SO_2. None of these gases measured above four percent of the sulfur in the black liquor solids. These species were very unstable at higher temperatures, with all species gone from the gas phase

by one second.

Two mechanisms were thought to create the high levels of mercaptan and mercaptan derivatives found in these experiments. The first mechanism was the volatilization of organically bound sulfur in the lignin. This amount of sulfur, however, could only account for approximately half of the mercaptans found in the gas. The rest of the mercaptans are thought to have come from the insertion of elemental sulfur into the C-H bonds of hydrocarbons. Elemental sulfur could come from the reactions of thiosulfate shown in reactions 23 and 24.

$$Na_2S_2O_3 + 3CO \longrightarrow Na_2S + S + 3CO_2 \tag{24}$$
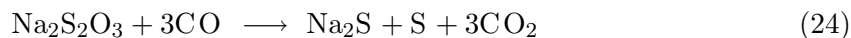
This is supported by the observed rapid disappearance of thiosulfate from the char in these experiments.

Li and van Heiningen performed a study in which the rate of H_2S generation was studied for black liquor gasification by steam [48]. The effects of temperature (from 600 to 700°C), H_2O (7-30%), and H_2 (0-20%) concentrations were investigated using thermogravimetric analysis. Sulfur species were analyzed using a gas chromatograph with a flame photometric detector. Infrared gas analyzers were used for CO_2 and CO. The main reaction of interest is shown in equation 25.

$$Na_2S + CO_2 + H_2O \longleftrightarrow Na_2CO_3 + H_2S \tag{25}$$

In order to account for the generation of CO_2 via the water gas shift reaction (shown in equation 26), the rate of H_2S generation was normalized by the rate of carbon dioxide generation.

$$H_2O + CO \rightleftharpoons CO_2 + H_2 \tag{26}$$

The researchers concluded based on their experiments that the reactions involving the generation of H_2S were controlled by equilibrium and not kinetics.

2.5 Current Work on Pressurized Gasification of Coal and Other Materials

Recent work on the influence of pressure on coal gasification has been produced by a group centered at the University of Newcastle in Australia. They have access to a pressurized

entrained flow reactor (PEFR), a pressurized drop tube furnace (PDTF), and a PTGA.

Cetin et al. recently published [12] work describing the effects of pyrolysis pressure and heating rates on biomass char characteristics using SEM, X-ray diffraction (XRD), and surface area analysis. Heating rates for the pyrolysis chars were varied by making chars in different reactors. Char produced at low heating rates resembled the parent material, while char at high heating rates underwent plastic deformation and had structures significantly different from the parent material. Increasing the pressure of pyrolysis resulted in the presence of more graphitic carbon in the pyrolysis char. Graphitic carbon is more ordered than the amorphous char carbon, resulting in carbon gasification only at the edges of the graphite crystals. The amount of graphitic carbon present (determined by XRD) explained much of the variation between gasification rates for chars prepared at different pressures and similar heating rates.

The University of Newcastle group also performed a study in which pyrolyzed coal char was created at various pressures using a PEFR and PDTF [66]. Surface area measurements were performed using N_2 and CO_2 adsorption, and gasification reaction rates were determined using a PTGA. The results indicate that while there is a significant change in the global gasification rate with different pyrolysis pressures, when normalized for surface area, the intrinsic reaction did not increase with increasing pyrolysis pressure. Chars created at high pressures and heating rates had much greater surface areas than chars that were generated at atmospheric pressures and slow heating rates. The crystalline structure of the chars was measured using XRD. It was found that heating rate, not pressure, had an effect on the crystallinity of the char carbon. High heating rate char had a lower percentage of graphitic carbon, while the lower heating rate char had a higher percentage of graphitic carbon.

In a letter to the editor of Fuel, Roberts et al. [67] shared data from PTGA experiments in which the total pressure of the system was increased at a constant partial pressure of either O_2, CO_2, or H_2O. Conversion rates were shown from a PTGA at 10% carbon conversion for 5 through 30 bar of pressure. The slopes of conversion rate vs. pressure for all three reactant gases was zero, indicating that for low temperature (900^oC) gasification

of coal there is no effect of total pressure on the rate of reaction. The authors speculated that pressure effects on gasification rates seen at higher temperatures may be related to phenomena other than surface reactions, such as diffusion limitations.

Numerous papers in coal gasification discuss the relationship between increasing pyrolysis pressure and increasing char plasticity [26, 82, 95]. The mechanism that is proposed for the development of plasticity in char particles is the breakdown of the coal aromatic structure with heat, creating aromatic radicals. These radicals can then become stabilized by hydrogen transfer and become primary tar components. Increasing the pyrolysis pressure has the effect of increasing the amount of time that the primary volatile matter is in the char structure before it is evolved into the gas phase. This decreases the viscosity of the char, decreases the minimum softening temperature, and increases the resolidification temperature [26].

Several attempts have been made to determine the effects of pressure on coal char swelling. These involve modeling the effects of pressure on the viscosity and metaplast content of coal chars [95]. It has been found that the swelling behavior is quite complex and is a function of several different factors, including:

- Specific volume of volatile gases emitted

- Decrease in volatile matter yield

- External resistance to swelling of particle

- Plasticity of char

Increasing the pyrolysis pressure will of course decrease the specific volume of volatile gases generated. There is also a trend in decreased tar (or volatile matter) yield with increasing pressure. This is thought to be related to the effect of pressure on plasticity. Increasing the pressure increases the amount of time that the tar precursors are in the carbon matrix. This increases the time available for these primary tar precursors to participate in secondary reactions, decreasing their molecular weight. Evidentiary support for this is the decrease in average molecular weights of tars with increasing total pressure and an increase in the amount of light weight carbon gases at higher pressures [82].

The presence of more light weight carbon gases at higher pressures suggests that some of the tars are able to decompose into permanent gases, while others only decrease their molecular weight. The lower molecular weight of the tar and higher level of hydrocarbon gases will increase the internal char pressure created by these gases by increasing the number of moles present inside the char particle. However, increasing the total pressure also increases the PV work required to swell the particle, as well as decreasing the specific volume of the volatile gases. All these factors must be taken into consideration, as well as the pressure effect on the plasticity of char, in order to model coal char swelling.

Coal char morphology has been classified in three distinct groups based on porosity and macro pore distribution in the char [51, 82, 95]. Group I, or cenospheric, chars are mostly hollow spheres with thin walls and very open interiors. Group II, or network, chars are largely hollow spheres with some internal networking and smaller pockets. Group III, or dense, chars consists of angular chars with low porosity and high densities. Increasing pressure increases the tendency of group I chars to be formed. This is thought to be because higher pressures allow for more fluid char and slower devolatilization of the gases, allowing the char to swell like a balloon. Lower pressures, with less fluid char and more rapid devolatilization, will result in the formation of more network and dense chars.

The formation of char is also a function of the coal components. Figure 4 shows the percent volume distribution of different coal chars by pyrolysis pressure and vitrinite content of the parent coal. Vitrinite is a primary component of coal. It is an organic portion of coal that is derived from cell walls or woody portions of plants.

Figure 5 shows SEM micrographs of coal chars generated at pressurized and atmospheric pyrolysis conditions [95]. The network-like honeycomb structure evident in subfigures (a) and (b) is reported to be typical of chars generated at high pressures. This suggests a more ordered release of gases at higher pressures. Subfigure (c) contains a hole in the surface, where rapidly evolving gases could escape at the surface of the particle.

Recently, a group of researchers in Japan utilized a combination drop tube/fixed bed reactor to determine the effects of total pressure and steam partial pressure on the gasification behavior of a Victorian brown coal [5]. A steam/N_2 mixture was fed through a

23
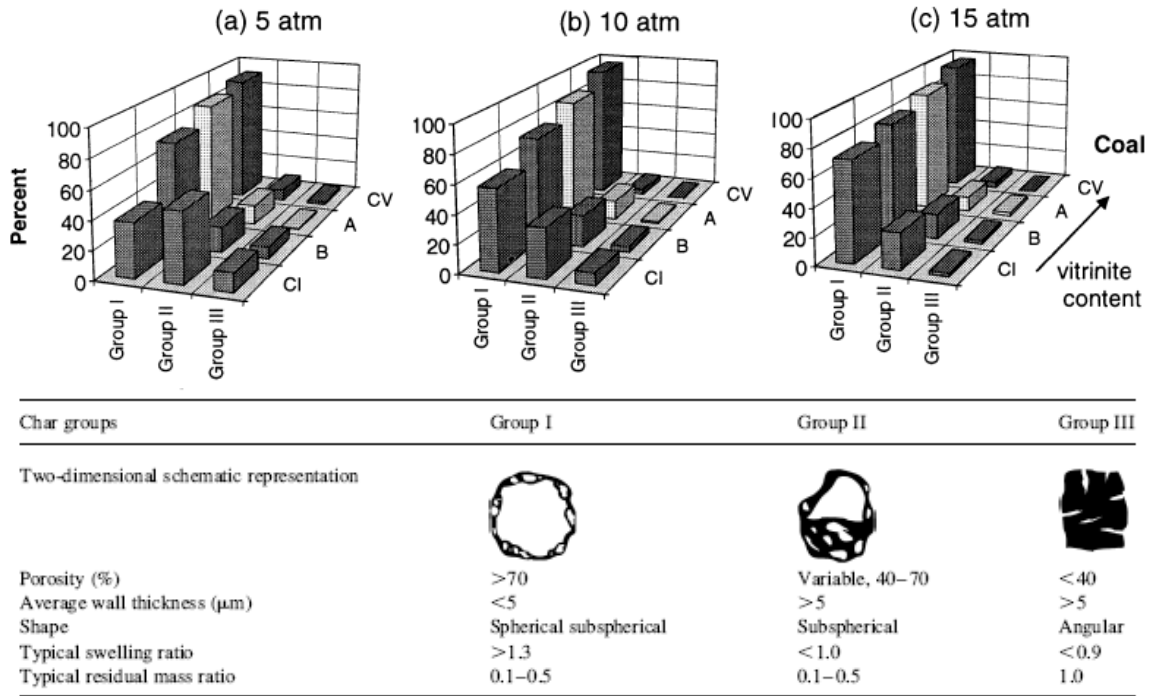
Figure 4: Influence of pressure and composition on coal char morphology
Source: [82]

(a) Pressurized   (b) Pressurized   (c) Atmospheric
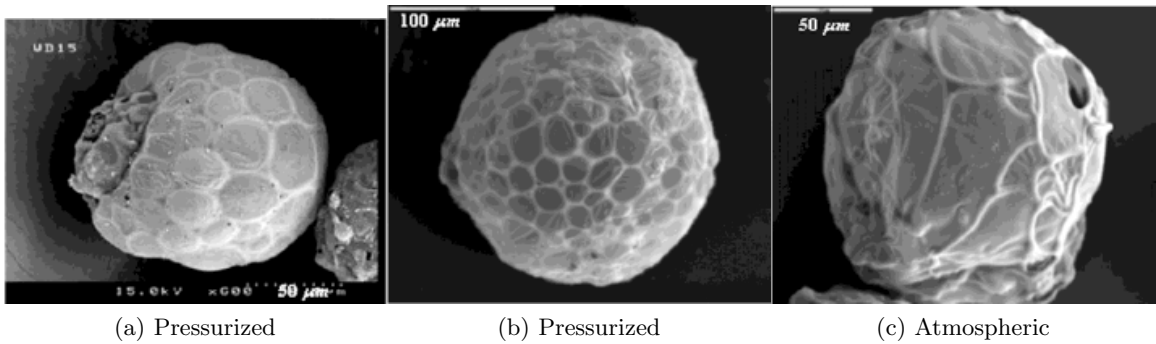
Figure 5: Coal char physical appearance after pressurized and atmospheric pyrolysis
Source: [95]

tube and across a filter plate. Once stable reaction conditions were reached, a sample of coal was released from a pressurized sample holder upstream of the filter plate. The sample holder was pressurized at five bar above the pressure of the reactor, and the release had the effect of shooting the coal onto the filter plate. The coal was then gasified by the gas passing the plate for a specified amount of time. It was found that two parallel gasification reactions were occurring: one catalyzed and one not. The catalyzed reaction was due to the

presence of trace amounts of Ca, Na, and Mg present in the coal. The catalyzed reaction rate was found to be a function of the amount of catalyst present, which was being lost due to volatilization and deactivation. The catalytic activity of the alkaline and alkaline earth metals was also a function of the heating rate, total pressure, and partial pressure of steam. The non-catalytic gasification was first order with respect to the amount of unconverted carbon. The researchers also acid washed the coal, thereby removing any catalytic alkaline earth metals, and compared the gasification rates with unwashed coal. The result was that the unwashed coal had much higher gasification rates until approximately 10% carbon conversion, after which the rate was the same as the washed coal.

In 2006 Harris et al. [31] published work on the gasification behavior of coals at high temperatures and pressure using a reactor very similar to the one used in this thesis. Harris added oxygen to his reactor in stoichiometric ratios of 50% to 200% (with 100% being enough oxygen added to convert all of the coal carbon to CO). It was found that increasing temperatures and increasing volatility of coal increased the "gasification efficiency" of the reactor. Gasification efficiency was defined as the ratio of CO/H_2 to CO_2/H_2O produced in the syngas. With respect to stoichiometric ratio, gasification efficiency went through a maximum near 100-110% and then decreased, as the excess oxygen available allowed for the formation of CO_2 and H_2O.

Since oxygen was added to the reactor in stoichiometric ratios, the gas concentration changed as a function of coal conversion as it traveled down the reactor. The equilibrium gas concentration of water gas shift species was calculated for the system as a function of conversion. These equilibria were then compared with actual gas concentrations measured at known carbon conversions. The results showed that the actual gas phase concentrations of the water gas shift species were very close to the equilibrium values at 1373K and 1673K, shown in Figure 6.
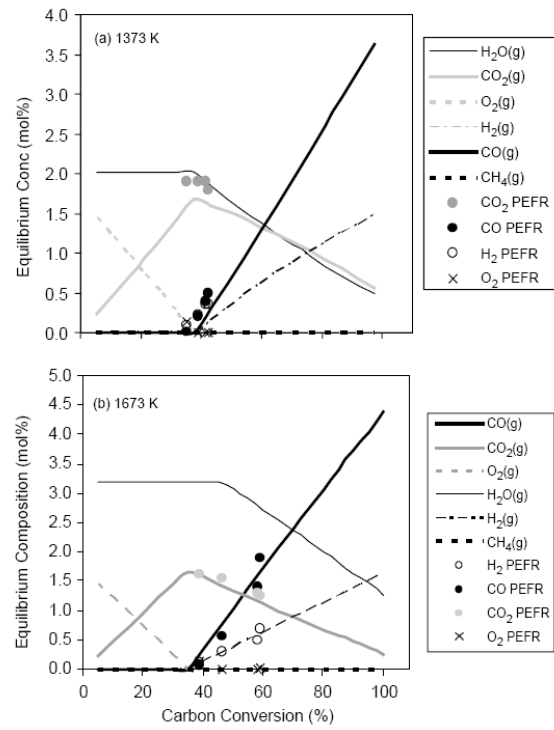
Figure 6: Actual and equilibrium water gas shift species concentrations for coal char gasification. P=20 bar, O_2 and N_2, O:C ratio 1:1

Source: [31]

CHAPTER III

SPECIFIC THESIS OBJECTIVES

The main technique that has been used to study gasification kinetics is thermogravimetric analysis (TGA). In TGA, a microbalance containing a sample to be gasified is heated to reaction temperature and exposed to a mixture of gases. The gasification rate is determined by calculating the rate of mass loss from the microbalance signal, with the assumption that all mass lost is due to the gasification reaction. Due to the alkali-catalyzed nature of black liquor gasification, however, this technique is unusable above approximately 750^oC due to mass transfer limitations. Several studies [12, 68, 89] have also shown the importance of pyrolysis char structure on subsequent gasification characteristics. The heating rate of black liquor has a large impact on the resultant char morphology. The slow heating rates employed in TGA are not representative of those found in industrial gasifiers.

Another technique that can be used to determine gasification kinetics are entrained flow reactors (EFR). EFRs are not subject to the mass transfer limitations associated with TGA, so kinetic investigations can be conducted at much higher temperatures. The heating rates of EFRs are also similar to those of industrial high temperature gasifiers, resulting in char morphology and kinetic data much more relevant to industrial applications. EFRs do not produce a continuous weight vs. time curve as TGA, but rather samples must be collected and separately analyzed at different residence times. The advantage of this discreet char sampling of the EFR over TGA, however, is that carbon conversion can be directly calculated instead of assumed from the weight signal.

The added variable of pressure significantly adds to the complexity of apparatus required for high temperature kinetic investigations. Consequently no data currently exists regarding the effects of pressure on the gasification characteristics of black liquor at high temperatures and heating rates relevant to black liquor gasification. Accordingly, the specific objectives of this thesis are to determine and mechanistically explain the effect of pressure on:

1. Pyrolysis and gasification char physical and chemical characteristics

2. High heating rate pyrolysis char carbon conversion

3. The rate of black liquor carbon gasification by H_2O and CO_2

4. Black liquor sulfur phase distributions under H_2O and CO_2 gasification

CHAPTER IV

EXPERIMENTAL AND ANALYTIC PROCEDURE

4.1 Experimental Overview

The black liquor used in this study was obtained from the New Bern, NC pulp mill owned by Weyerhaeuser. The liquor was received as approximately 50% solids, and spray dried under nitrogen at approximately 33% solids. After spray drying the liquor was sieved in standard 10 inches sieves. The main size fraction used in the study was 75-90 μm, with a smaller size of 38-53 μm used to experimentally determine the effect of particle size on conversion rates.

Table 4 outlines the experiments performed for this study. They can be clustered into three broad experimental groups: pyrolysis, constant partial pressure gasification, and constant mole fraction gasification.

Table 4: Experimental overview

Group	Description
Pyrolysis	5, 10, and 15 bar total pressure; 100% N_2; residence time between 0.9 and 3.5 seconds
Constant Partial Pressure Gasification	5, 10 and 15 bar total pressure; 0.25 bar H_2O, 0.5 bar CO_2; residence time between 0.6 and 3.5 seconds
Constant Mole Fraction Gasification	5, 10, and 15 bar total pressure; 10% CO_2, 2% H_2O, 1.7% CO, 0.3% H_2; residence time between 0.9 and 3.5 seconds

When discussing the high temperature black liquor reactions it is important to define the terms devolatilization, pyrolysis, and gasification.

For the purposes of this work, devolatilization refers to the initial mass lost after the black liquor enters the reactor. This mass is converted to various components such as

alcohols, aldehydes, and ketones, which are not thermodynamically stable and further decompose [74]. Studies have shown that this occurs in less than 0.1 seconds at 900^oC [74].

Pyrolysis reactions are defined as the char reactions occurring after the initial devolatilization of the black liquor. These reaction include, but are not limited to, the reduction of carbonates, sulfates and thiosulfates, and other reactions due to the thermal degradation of the lignin present in the black liquor. These reactions are slower than the initial devolatilization, occurring during the residence times investigated in this study. If any thermal decomposition of the black liquor results in carbon dioxide (for example the reduction of sulfate), then this CO_2 is referred to as secondary CO_2 and any reaction involving it will be considered pyrolysis as well. Due to physical limitations of the reactor, residence times of less than approximately 0.6 seconds were not obtained. Therefore it is not possible to differentiate between devolatilization and early pyrolysis reactions.

Gasification reactions are defined as the reactions between carbon from the black liquor and the CO_2 and H_2O that were separately introduced to the reactor. The presence of these gasification gases will impact the progression of the previously mentioned pyrolysis reactions. For example, CO_2 in the gas phase will suppress the reduction of carbonate, thereby decreasing the amount of secondary CO_2 generated.

Every char that was generated was analyzed for carbon, carbonate, and various metals. A smaller number were analyzed by various physical methods as described below. By using vanadium as a tie element, a char yield was determined for each char according to equation 27

$$CY = \frac{[V]_{bl}}{[V]_{char}} \tag{27}$$

where CY is the char yield, $[V]_{bl}$ is the vanadium concentration of black liquor used to generate that specific char, and $[V]_{char}$ is the vanadium concentration of the char. From the char yield and metals, total carbon, or carbonate data, the amount of any remaining material in the char was determined as a percentage of that material in the feed black liquor. This is shown in equation 28,

$$\%M = CY \times \frac{[M]_{char}}{[M]_{bl}} \tag{28}$$

30

where $\%M$ is the percent of material remaining, CY is the char yield, and $[M]$ is the concentration of the material in either the char or black liquor.

The pyrolysis experiments were conduced under 100% nitrogen in order to study the effect of pressure on carbon conversion due to the oxidation of carbon from the oxygen inherent in the black liquor. The black liquor used in this analysis was determined to contain 34% by weight oxygen, which results in an equilibrium conversion of almost 75% of solid carbon to CO (see Figure 16).

In addition to pyrolysis experiments performed at multiple residence times, a series of pyrolysis experiments were conducted at a short residence time of 0.9 seconds. These experiments were used to determine the effects of pressure on the physical characteristics of the char, under the assumption that the physical effects of pressure would manifest themselves in the char immediately after the black liquor enters the reactor, swells, and devolatilizes. The char will continue to change as it travels down the reactor, but these changes will be a function of conversion, not a function of the pressure. These chars were put through a suite of tests, including mercury porosimetry, particle size analysis, SEM and optical microscopy, and surface area analysis.

The constant partial pressure experiments were conducted in order to elicit the true effect of pressure on gasification rates, since the partial pressures of reacting gases would be constant at all conditions. While there was no upper limit on the partial pressure of CO_2, 0.25 bars of pressure for H_2O was the practical limit for the reactor due to condensation issues in the exit piping. In addition to being chemically analyzed as described above, fifteen constant partial pressure gasification chars were analyzed by nitrogen adsorption for their surface area. Five chars at each pressure were selected so that the widest possible range of conversions was tested.

The constant mole fraction experiments were conducted due to industrial interest. Production gasifiers do not have the luxury of independently changing reaction gas partial pressures, they can only manipulate the total pressure and stoichiometric oxygen ratio entering the reactor. In order to address the effect of the water gas shift reaction, which shifts toward equilibrium as function of the reaction gas partial pressures, sufficient CO

and H_2 were added so that the entire system was at equilibrium prior to any gasification reactions. As with the constant partial pressure experiments, the limiting factor for water concentration was the saturation pressure. Therefore these experiments could not have an H_2O content exceeding 2%.

4.2 Black Liquor Preparation

4.2.1 Spray Drying

The liquor used in this study was obtained from the Weyerhaeuser mill located in New Bern, North Carolina. Table 5 shows analysis results for a sample of liquor that was taken on December 17, 2005. The nominal concentration of the liquor was assumed to be 50% solids, and all consistency calculations for for spray drying were based on this assumption.

Table 5: Weyerhaeuser black liquor analysis [77]

Test	Value	Comment
130° Solids	48.6%	As Recieved
HHV (BTU/lb)	6060	TAPPI Solids Basis
Total S	6.47%	TAPPI Solids Basis
S^{2-}	3.26%	TAPPI Solids Basis
$SO_4{}^{2-}$	3.67%	TAPPI Solids Basis
Cl	0.17%	TAPPI Solids Basis
C	35.1%	TAPPI Solids Basis
H	3.2%	TAPPI Solids Basis
N	0.1%	TAPPI Solids Basis
K	1.14%	TAPPI Solids Basis
Na	19.6%	TAPPI Solids Basis
OH^-	2.56%	TAPPI Solids Basis
$CO_3{}^{2-}$	3.70%	TAPPI Solids Basis

The spray dryer used for preparing the liquor is a Lab Spray-1 model made by Anhydro. The spray dryer configuration utilizing the stationary nozzle was used to generate the spray dried liquors for these experiments. Of the two orifice sizes available, the larger size was used, measuring 1016 μm in diameter. A magnetically coupled gear pump with variable frequency drive was used to feed the black liquor. A complete list of settings used can be found in Table 6. Further details on the operational procedure and setup of the spray dryer can be found in Appendix C.

Table 6: Spray dryer settings

Setting	Range
Heater	4-6 kVa
N$_2$ to Atomizer	10-12 psi
BL Pump Output	4-12%
Atomizer	Stationary, Large Orifice

4.2.2 Sieving Conditions

The dried black liquor was removed from the collection cup of the spray dryer and stored in 2-liter glass jars until ready to sieve. Sieving was conducted using standard 10" sieves of 106, 90, 75, and 63 μm mesh sizes. The four sieves were placed in a forced-air oven at 105° C for at least 5 minutes prior to sieving to ensure dryness. The sieves were immediately placed in the shaking rack after removal from the oven, and black liquor was added to the 106 μm sieve to a depth of approximately one inch. A stainless steel lid was then placed on top of the sieves, as well as a plexiglass shield to keep the sieves tight in the rack. The liquor was allowed to sieve for 5 minutes at the "high" setting on the rocker switch and at 55% on the rheostat. The liquor was then brushed out of each sieve onto a teflon pan, and then transferred to another 2-liter jar for storage until used in the experiments. In between each use the sieves were washed, towel dried, and placed back in the oven for several mintues to ensure dryness.

Another important variable when sieving the liquor is the dryness of the black liquor. The unsieved black liquor will pick up small quantities of water even with brief exposure to the atmosphere. The presence of this water will cause the liquor to behave like a Geldart Class C powder [64] when turning the glass storage jar, meaning that the liquor will tend to fall in clumps together instead of flowing like sand. If the liquor behaves like this then it is quite possible to get uneven distributions of the liquor across the sieves. The best way to avoid this is to place the open jar of unsieved liquor in a quiescent oven while the sieves are drying in the forced air oven. Remove the liquor from the oven using gloves and immediately pour it into the hot sieves placed on the rack.

4.3 Pressurized Entrained Flow Reactor Operation

The pressurized entrained flow reactor (PEFR) is by far the most complex piece of equipment used in this study. See figure 7 for a cross sectional diagram of the PEFR. Details regarding the design and construction of the PEFR can be found in reference [69].
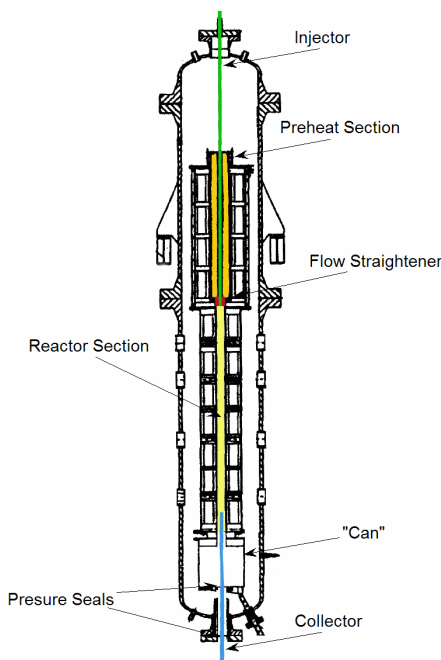
Figure 7: Cross section of the Pressurized Entrained Flow Reactor (PEFR)

The spray dried black liquor and a carrier gas (hereafter referred to as primary nitrogen) enter the reactor via a liquid cooled injector, shown in green. The secondary gases, consisting of N_2, H_2O, CO_2, H_2, and CO enter the reactor via gas headers located at the top of the preheat section, shown in orange in Figure 7. As the secondary gases travel down the preheater section, four electric kilns heat the gases up to the reaction temperature. At the end of the preheat section, the hot secondary gases travel through a cordeirite honeycomb flow straightener (100 cells/in^2). This imparts a flat velocity profile to the gas as it enters the reactor section, shown in yellow in Figure 7. The reactor section is also heated by seven separate electric kilns, and the radiant heat from the walls of the reactor, as well as the already hot secondary gases, combine to rapidly heat the primary nitrogen and black liquor particles to the reaction temperature.

Table 7: PEFR reactor dimensions [69]

Dimension	Value	units
Pre-heat Diameter	155	mm
Pre-heat Length	1.372	m
Reactor Diameter	82.5	mm
Reactor Length	2.0	m
Injector OD	34	mm
Injector ID	14	mm
Collector OD	50	mm
Collector ID	12.7	mm

The concentric placement of the injector in the preheat section, along with the proper ratio of primary and secondary gases, serve to keep the particles located in the center of the reactor. The particles then travel down the center of the reactor and are collected by a liquid cooled collector, shown in Figure 7 in blue. The collector is located on a set of jacks and can be moved up and down in the reactor. This is the primary method by which residence time is varied. An additional flow of cool nitrogen is added in the top of the collector in order to rapidly quench any reactions after the particles and gas enter the collector. The mixture of particles and gas then enter a cyclone that separates the char particles from the gas. The cyclone is designed to have a 50% size cut of 2-4 μm at these flow conditions. The gas exiting the cyclone then passes through a glass fiber fume filter, which removes fine particles such as condensation aerosols down to 0.01 μm from the gas.

Hundreds of hours of observation were made regarding the operability of the reactor. Many of these observations can be found in Appendix A, which lists specific troubleshooting tips for reactor operation. On August 4th, 2005 the reactor was taken apart to replace a damaged reactor tube. The data shows a marked difference before and after the reactor tube replacement. While the trends stayed the same, they were shifted with respect to residence time. All data shown in the main body of this thesis was generated after the reactor tube was replaced.

4.3.1　Important Modifications

The main difficulty in operating the PEFR is plugging of the black liquor injector at the tip, where the black liquor enters the reactor. Since the injector must be liquid-cooled there is a large difference between the inner and outer diameters (see Table 7). This creates a dead zone at the beginning of the reactor between the secondary gas and the primary gas, creating a zone of separated flow. Also, the reaction conditions are above the melting point of the inorganic salts in the black liquor, making them sticky. The separated flow zone near the tip of the injector combined with the sticky nature of the black liquor char makes control of the entrance conditions critical to successful PEFR operation.

Pressure Seal Removal

From March 25, 2005 until the reactor was taken apart in mid-May 2005, the reactor was limited to approximately 8 minutes of feeding before a plug formed at the tip of the injector. After removing the collector, visual inspection of the reactor revealed that the plug was asymmetric and tended to grow toward the same side of the reactor time after time. The injector was removed and repositioned several times in the flow straightener in an attempt to fix the irregular flow, but to no avail. Only after dismantling the main pressure vessel and lowering it did we discover that hot gases were leaking out of the reactor core and into the main pressure vessel. The gases were then re-entering the reactor at the bottom of the reactor section, where the bottom "can" bolts onto the end of the reactor, finally leaving the system through the collector.

During the May 2005 rebuild of the reactor the secondary, interior sliding pressure seal (which the collector passes through, located in the bottom of the can) was removed due to char buildup in it. The removal of this second pressure seal had the additional benefit of improving the flow pattern of the reactor. At the end of a set of experiments the pressure in the vessel needs to be reduced. This is done by venting the pressure at a port in the exterior shell of the reactor. The presence of the second pressure seal resulted in the hot gas still present in the reactor core having to exit either at the flange where the can bolts to the reactor section or at the flange that connects the preheat section to the reactor section. A synthetic gasket sealant is applied to both of these flanges, but the gases are at temperatures

much higher than what the gasket sealant can withstand (which is approximately 600ºF). The same phenomenon of gas penetrating the reactor core through the flanges would occur when pressurizing the reactor as well. The repeated pressurizing and depressurizing of the reactor created a situation where the path of least resistance for the reaction gases was out the flange connecting the preheat and reactor sections and returning to the collector by passing back through the flange connecting the can to the bottom of the reactor section.

Removal of the second pressure seal at the bottom of the can allows the hot gases in the reaction section to exhaust through the annulus between the collector and the hole in the bottom can. There is very little differential pressure created while pressurizing or depressurizing the reactor. This allows the high temperature sealant placed in between the flanges to remain intact, and maintains a desirable flow pattern down the axis of the reaction section. This mechanism is supported by evidence of gases leaving and entering the reactor at the respective flanges and the fact that 165 runs have now been performed since removal of the second pressure seal with no reduction in the time before plugging the injector.

Loss in Weight Feeder

Another important modification that improved the runnability of the reactor is the introduction of the loss in weight (LIW) feeder. The LIW feeder consists of a clear plastic tube with two concentric hollow brass shafts in the center. The exterior shaft has fingers that agitate the black liquor as it is rotated by a 12 volt DC motor. Turning the motor forward causes the exterior shaft to rotate while keeping the inner shaft stationary, exposing holes in the inner shaft. The exterior shaft continues to rotate until it hits a pin fastened to the interior shaft, after which the two shafts rotate as one. Feed rate can be slightly modified by changing the voltage on the DC motor, but the best way to increase the feed rate is to drill larger holes in the center shaft. The entire LIW feeder is placed on a strain gauge, which has a readout in the Labview screen in the control room. The LIW feeder gives direct verification that liquor is entering the system by the weight readout on the control screen, which is a significant improvement over the previous auger design, which had no such readout. The ability to directly read the weight at the beginning and end of each run

makes for much more accurate mass closures on days when multiple runs are performed.

Water Gas Header

In early October 2005 the water vapor addition at the top of the preheat section was changed from a point-source to an unused semi-circular gas header. These changes were made to more evenly distribute the water vapor across the cross section of the reactor. It is suspected that water vapor distribution may have been a problem after observing increasing condensation problems in the cyclone as the total pressure decreased, even though the partial pressure of water in the cyclone decreased (due to the constraint that quench nitrogen flow could not exceed 100 NLM). See Table 8.

Table 8: Cyclone saturation temperature for constant partial pressure experiments

Pressure (bar)	H_2O (Mole %)	Reactor P_{H_2O} (bar)	Quench Ratio (% Total Gas)	Cyclone P_{H_2O} (bar)	Cyclone T_{sat} (^oF)[11]
5	5.0	0.249	88	0.132	124
10	2.5	0.244	66	0.147	128
15	1.7	0.246	44	0.171	134

The condensation problems could be explained by uneven water distribution in the reactor section, causing a locally high concentration of water that would condense on the liquid cooled collector. The higher mole percentage of water and lower gas phase Reynolds number present at the lower pressures would increase this problem.

Another reason why it is suspected that water distribution may be a problem was the initial data for sulfur phase distribution. Figure 8 illustrates the increased variability of percent sulfur remaining in char with increasing pressure. The five bar data (with the exception of one point) follows a clearly defined trend. The ten bar data exhibits more scatter, and the fifteen bar data is quite scattered with respect to percent sulfur remaining.

Carbon conversion, carbonate concentration, and distribution of all other elements seemed to make sense for these points, but the sulfur phase distribution did not seem to follow any trend. This could also be explained by poor water distribution, which would preferentially affect the sulfur distribution due to the reaction of some sulfur species with water, which creates H_2S. The higher pressure experiments run under constant partial
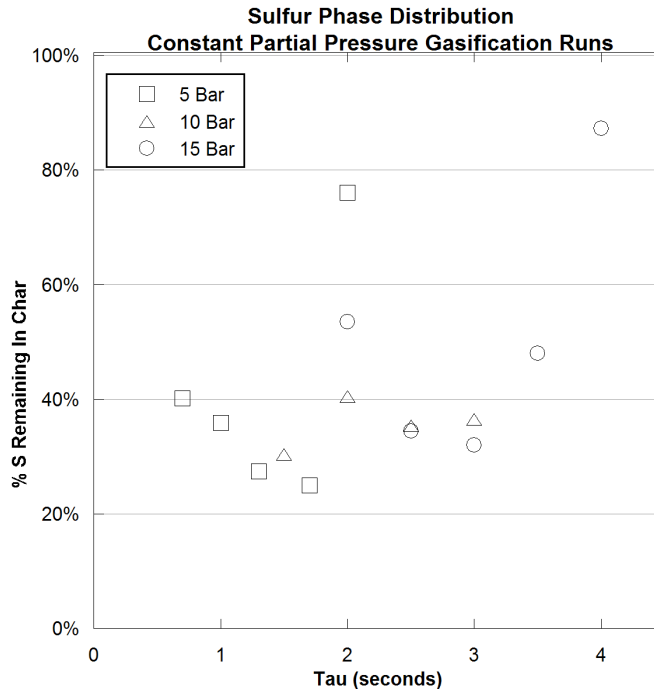
Figure 8: Sulfur phase distribution prior to changing water gas injection. $900^{o}C$, 0.25 bar H_2O, 0.5 bar CO_2, balance N_2

pressures of reacting gases have both a lower mole percentage of water and lower gas diffusivities. If the char particles were not exposed to water vapor as they traveled down the reactor the sulfur would return to the condensed phase, since the primary sulfur species present at equilibrium without the presence of water is Na_2S. After changing the water injection from a point source to a gas header the sulfur data was more consistent, with an easily distinguished equilibrium. This will be discussed in more detail later Chapter 8.

Velocity Ratio

The last important modification that was made to the reactor was the ability to change the primary to secondary gas velocity ratio. Prior to May 2005 the velocity ratio was fixed at 3.0, based on observations made by Flaxman [15] and previous runs with another black liquor, provided by Babcock and Wilcox. It was observed, however, that the New Bern liquor used in the study had different plugging characteristics than the B&W liquor, which had been used quite extensively in the reactor. This is not surprising given the large amount of experimental evidence regarding the dependence of black liquor swelling on composition [24, 56].

Based on observations while running the PEFR and by evidence given in this thesis, the black liquor char is in a plastic state immediately after entering the reactor. The plastic surface of the char will conform and adhere to any surface that it comes in contact with. By being able to independently change the velocity ratio it was possible to identify a ratio for this specific liquor that minimized its contact with the walls of the injector tip. This gave run times of up to one hour while allowing four to five grams of char to be captured in the cyclone during each experiment.

4.3.2 PEFR Daily Operation

The daily operation of the PEFR required the use of extensive checklists to ensure quality data and safe operation. A detailed list of tasks can be found in Appendix C

4.4 Surface Area Measurements

The surface area for pyrolysis and gasification chars was determined using a Micromeritics Gemini II 2370 surface area analyzer, in conjunction with a Micromeritics degasser. The BET method [9] of surface area analysis was used, in which the pressure of nitrogen, the volume of nitrogen adsorbed (in cm^3/gram), and the saturation pressure of nitrogen are plotted as a function of relative pressure, so that

$$X = \frac{P}{P_o} \tag{29}$$

$$Y = \frac{P}{V(P_o - P)} \tag{30}$$

where P is the partial pressure of nitrogen at a sample point, P_o is the saturation pressure of nitrogen, and V is the volume per gram of nitrogen adsorbed on the char. The surface area can then be calculated from the slope and Y intercept (which have the units of $\frac{gram}{cm^3 \ STP}$) of the line using

$$S.A._{BET} = \frac{(0.162 \frac{nm^2}{N_2 \ molecule})(6.023 \times 10^{23} \frac{molecule}{mole})}{(22,414 \frac{cm^3 \ STP}{mole})(10^{18} \frac{nm^2}{m^2})(Slope + Y_{int})} \tag{31}$$

Further details regarding these calculations can be found in Appendix A of the instrument operation manual [54].

Investigative experiments were conducted with excess PEFR char in order to determine optimum operating conditions of the system. Variables investigated included:

- Degassing temperature

- Degassing time

- Free space measurement

- Surface area mode (scan or equilibration)

- Equilibration time

- Amount of char

The studies showed that the surface area of the char did not vary much in the degas temperature range of 150^oC to 350^oC. The time required for complete degassing, however, increased as the degas temperature decreased. If the volume of N_2 adsorbed decreased at increasing partial pressures of N_2, it was assumed that the sample was not fully degassed and these points were not used.

Other parameters used in the analysis can be found in Table 9. Daily operational procedures can be found in Appendix C.

Table 9: Surface area analysis conditions

Parameter	Value	Units
Minimum Relative Pressure	0.1	
Maximum Relative Pressure	0.3	
Number of points	5	
Degas Temperature	300-350	^oC
Degas Time	> 60	minutes
Evacuation Time	1.0	minutes
Evacuation Rate	300	mm Hg/min
Analysis Mode	Equilibration	
Equilibration Time	5.0	seconds

The surface area of each char was determined at least three times. If the experiment had more than one point in which the volume of N_2 adsorbed decreased as the pressure of

N_2 was increased, that experiment was not included in the calculation of the surface area. See Appendix A for troubleshooting tips regarding the use of the instrument. See Appendix B for example surface area calculations.

4.5   Scanning Electron Microscope

Scanning electron microscopes (SEM) use a stream of electrons to illuminate a sample, which causes secondary electrons to be emitted. These secondary electrons are then collected and used to produce images of both high resolution and good depth of field. The SEM used in this study was the Hitachi X800 Field Emission Gun Scanning Electron Microscope located in room 170 of the Love Building. It is a medium resolution microscope that is very user friendly to operate. Electron microscopy is better than optical microscopy for high magnification applications. Any microscopy technique will be limited in resolution by the wavelength of the source. This is because as the size of objects near the wavelength of the source it becomes impossible to focus on the object. The short wavelength of an electron beam relative to light allows for much smaller objects to be studied in detail.

Char samples were prepared by sprinkling the char particles onto a 1/2" inch diameter double stick conductive carbon tab that was adhered to a 13mm sample mount. The special conductive tape minimizes charging, or buildup of negative charge due to the insulative properties of a sample. It is important that the sample have good contact with the carbon tape, and care must be taken to ensure good adhesion of the sample while also not damaging the char structure. If a sample contains many oxides or is otherwise non conductive, it must be sputtered with gold to increase conductance. The char generated in the study was sufficiently conductive to not require this step. The black liquor did have a greater tendency to charge, but it was possible to take several detailed pictures by decreasing the accelerating voltage, which also reduces charging. In order to minimize the fouling of the optics in the electron microscope, gloves were used whenever handling the sample after it was stuck to the carbon tab. Detailed instructions regarding the operation of the S-800 can be found on the Georgia Tech Material Science Department website [6]. Table 10 lists specific settings for this study.

Table 10: SEM settings

Parameter	Value	Units
Accelerating voltage, char	10.0	kV
Accelerating voltage, liquor	4.0	kV
Aperture size	100-200	μm
Magnification	250-10,000	

4.6 Mercury Porosimetry

Mercury porosimetry is an analytical method that uses the natural characteristics of mercury (non-wetting, high surface tension) to determine the macro-pore size distribution of a solid. A non-wetting liquid will penetrate a capillary if sufficient outside pressure is applied to the system. Washburn defined the relationship between pressure and pore size as $pr = -2\sigma\ cos\theta$ [85], where p is pressure, r is pore radius σ is surface tension, and θ is the contact angle.

Ritter and Drake [65] were the first to use this principle in conjunction with mercury to characterize the macro porous structure of solids. By increasing the pressure in fixed increments a profile of pore volume vs. pore diameter can be determined. Sufficient time must be given between pressure increases in order to allow the mercury to stop flowing, as shown by the Hagen-Poiseuille law, $Q = V/t = (\pi r^4)(8\eta)(\Delta P/l)$, where Q is the flow rate of the liquid, V the volume of liquid, t the time, r the capillary radius, η the liquid viscosity, and ΔP/l the pressure drop down the capillary [85].

Incrementally increasing the pressure of mercury to determine pore characterization is called intrusion analysis. As the name suggests, the mercury will penetrate the particle from the outside toward the center. If the pore contains a constriction or is otherwise non-cylindrical, the mercury will not penetrate past this constriction until sufficient pressure is applied to the system. Mercury extrusion analysis works in exactly the opposite fashion as intrusion. By decreasing the pressure on the system, mercury will recede from pores. A constriction in the pore will result in some mercury being retained in the particle on the interior side of the constriction. If the pores are perfect cylinders, a plot of intrusion volume and extrusion volume as a function of pore diameter would be exactly the same. In reality,

however, intrusion and extrusion volumes will often display a hysteresis. The magnitude of this hysteresis is illustrative in determining the number of pores which contain a constriction.

Table 11: Mercury porosimetry data

Data	Units	Comments
Total Intrusion Volume	mL/g	Directly measured
Total Pore Area	m^2/g	Assumes cylindrical pores
Median Pore Diameter	μm	Diameter at which 50% of Hg in particle
Average Pore Diameter(4V/A)	μm	Intrusion Volume divided by Pore Area
Bulk density (ρ_b)	g/mL	Determined before any pores are filled
Particle Density (ρ_p)	g/mL	Determined after open pores are filled
Porosity (ϵ)	%	1 - ρ_b/ρ_p

Mercury intrusion/extrusion analysis was performed by Micromeritics Analytical Services using an AutoPore IV 9500 porosimeter. Three pyrolysis chars and a sample of spray dried black liquor were analyzed. The pyrolysis chars were formed at 5, 10, and 15 bars total pressure, with the collector positioned 200 millimeters away from the injector. In addition to pore sizes, several other characteristics of the char were determined by the experiments, shown in Table 11.

As shown in Table 11, the total pore area and average pore diameter are determined by assuming a cylindrical pore. In actuality the char particles have extremely non-cylindrical pores, so these data were not used for analysis of the char. More information regarding the pore size and structure will be given in Chapter 5.

Other parameters used by Micromeritics in their mercury intrusion and extrusion analysis are listed in Table 12. Details regarding specific calculations provided in the report generated by Micromeritics can be found in Appendix D of reference [55]

4.7 Laser Light Scattering

Laser light scattering is a technique that uses a laser of a single wavelength to determine the size of particles in a dilute solution based on the tendency of the solution to scatter the light. Light scatter is the sum of the effects of reflection, refraction, and diffraction of the solution [84]. By knowing the wavelength of light, λ, the intensity of the original light source, I_o, the index of refraction of the particle, n, and the scattered light intensity I_{sc} and

Table 12: Mercury porosimetry experimental parameters

Parameter	Value	Units
Advancing/Receding Contact Angle	130	degrees
Hg Surface Tension	485	dynes
Hg Density	13.5335	g/mL
Evacuation Pressure	50	μm Hg
Evacuation Time	5	minutes
Hg Filling Pressure	0.55	psia
Equilibration Time	10	seconds
Sample Weight	0.05-0.18	grams

it's angle θ, it is possible to determine the size of particles in a solution via the relationship $I_{sc} = I_o \times f(\theta, \lambda, d, n)$. This theory, first described by Gustav Mie, is the underlying principle by which these particle sizes were determined.

Particle size distributions were determined by Micromeritics Analytical Services. The instrument used was a Saturn DigiSizer 5200, which can measure particle sizes from 1000 to 0.1μm. The intensity of the scattered light is determined by the instrument at various angles. Scattered light intensity for various particle sizes are then calculated via the Mie theory. The particle size distribution used in the Mie theory calculation is varied until agreement with the experimentally determined scattering pattern is achieved.

The report provided by Micromeritics gives a particle volume frequency distribution as a function of particle diameter. Table 13 gives the input parameters and information provided in the report. The mean diameter is a weighted average of the volume distribution and average particle diameter. The median diameter denotes volume median, at which 50% is greater than the median, and 50% is less than the median.

4.8   Other Analytical Methods

4.8.1   Inductively Coupled Plasma-Atomic Emission Spectroscopy

Char samples were analyzed by the IPST analytical laboratory for sodium, potassium, sulfur, calcium, and vanadium using inductively coupled plasma atomic emission spectroscopy (ICP-AES). The samples were first digested using EPA method 3050B [2], which uses heated 50% HNO_3 and 30% H_2O_2 to digest the char and dissolve all metals. The samples were

Table 13: Light scattering experimental parameters and information

Parameter/Data	Value	Units
Material	Carbon/Isopropanol	
Flow Rate	120	sec
Ultrasonic Intensity	100	%
Ultrasonic Time	60	seconds
Sample Concentration	0.02-0.04	%
Mean Volume Diameter		μm
Median Volume Diameter		μm

analyzed following EPA method 6010B [3]. Two dilutions were made for each char sample in order to ensure linearity across the wide ranges of concentrations analyzed. A large number of samples were analyzed over nine months which required that a consistent procedure be used from batch to batch. In addition to EPA method 6010b, Table 14 outlines conditions specific to this analysis.

Table 14: ICP-AES analysis conditions

Item	Value	Units
Method	EPA 6010b	
Digestion amount	100	mg, total solid
Digestion final volume	25	mL
Na,S dilution	20	times
Ca,K,V dilution	1	times

The liquor used in this study has an unusually high concentration (approx. 200ppm) of vanadium as a result of fuel oil being burned in the mill. This high concentration of vanadium allowed for the use of it as a tie element in this study in lieu of calcium. Vanadium remains in the solid phase at 900°C (see Figure 20), making it a valid choice for a tie element. Also, it is more evenly dispersed than calcium in the black liquor, as shown in Figure 9, where the variation of vanadium concentration across 32 black liquor samples is much less than the variation in the calcium concentration across the same samples.

A possible explanation for the more even distribution of vanadium than calcium could be that calcium can be present either as organically bound or as $CaCO_3$, which can settle
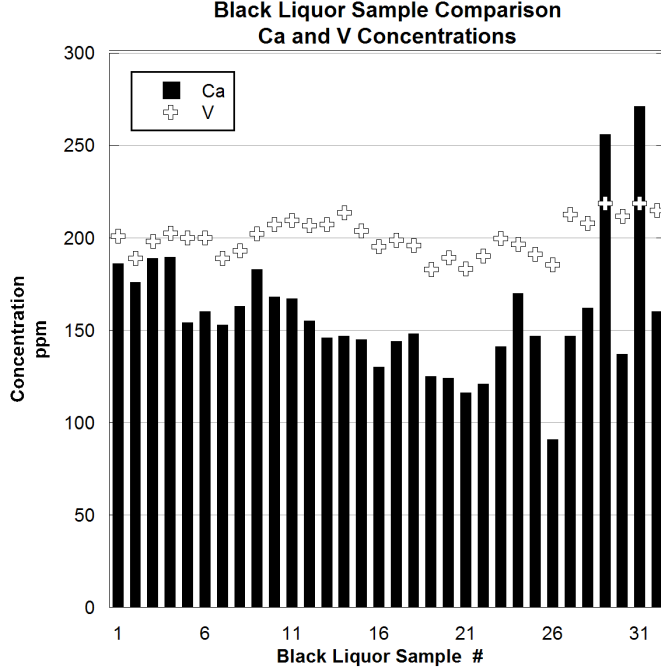
Figure 9: Tie element comparison

out and cause concentration gradients if the samples are not handled properly. The organically bound calcium would correspond to the soluble fraction and the carbonate would be associated with an insoluble fraction, as defined by Frederick and Grace [17]. Work by Lansdell [41] indicates that the insoluble fraction can be up to 70% of the total calcium in black liquors obtained from mills.

Wallberg et al. [83] found that multivalent cations such as Mn and Fe have a very high retention rate in black liquor ultrafiltration. This was attributed to their ability to form complexes with the organic ions present in black liquor. This observation was also made by Westervelt [86], who noted the tendency of transition metals to easily form chelates in black liquor. Since Vanadium is also a transition metal, with similar electron structure as Mn, the same mechanism could be used to explain it's even distribution in the black liquor.

Also, the potential for environmental contamination from calcium is much greater than for vanadium. Calcium can easily contaminate dilutant water and is known to be a trace contaminant in the plastics used in the IPST analytical lab.

Finally, the uncertainty of the vanadium concentration peaks from the AES data (as

measured by relative standard deviation) are typically two to four times less than the uncertainty of the calcium peaks. All these facts combine to explain the differences in variability between vanadium and calcium shown in Figure 9.

4.8.2 Carbonate

Carbonate was measured using two different methods: coulometric and headspace gas chromatography. Both methods were comparable, as illustrated by Figure 10.
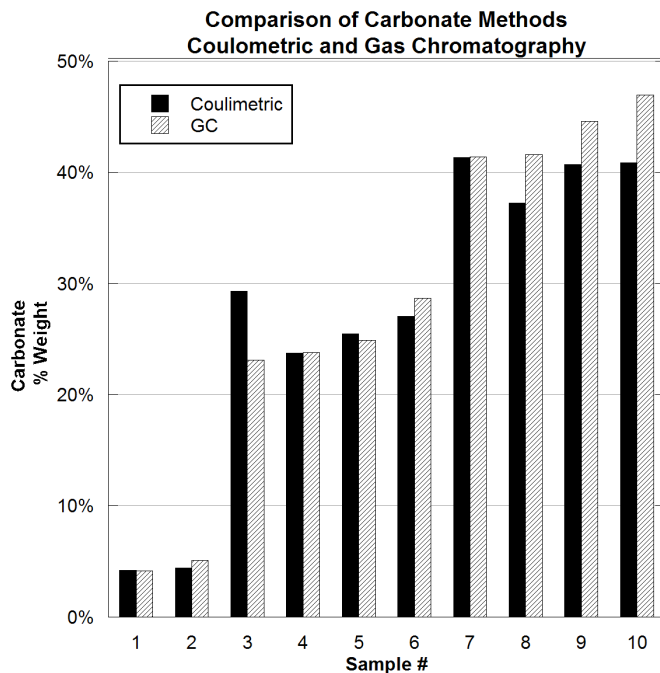
Figure 10: Carbonate analysis comparison

The headspace gas chromatograph method [13] utilizes the acidic decomposition of $CO_3{}^{2-}$ into CO_2 by measuring the CO_2 concentration in the headspace above a sample. A measured amount of char or black liquor was added to a known volume of water and vigorously agitated so that all the carbonate would be dissolved. An aliquot was extracted using a syringe and added to an excess amount of 2 molar H_2SO_4, producing CO_2. The concentration of this CO_2 is then measured in the chromatograph. Table 15 contains actual conditions used in these experiments.

The coulometric technique uses a UIC model CM 140 Total Inorganic Carbon Analyzer, which uses an acid digestion to dissolve inorganic carbon and release CO_2 and other gases.

Table 15: GC-HS carbonate analysis conditions

Parameter	Value	Units
Char Weight	0.2-0.3	grams
Liquor Weight	0.05-0.1	grams
H_2O volume	1.0	mL
Aliquot volume	100	μL
Standard Concentration	0.1	Molar Na_2CO_3

These gases are then passed through scrubbers that preferentially eliminate gases other than CO_2. The CO_2 gas then passes to UIC model 5014 CO_2 coulometer, which reacts with a solution and decreases its pH. The coulometer then uses electricity to restore the solution to its original pH.

4.8.3 Total Carbon

Total carbon was analyzed by the IPST analytical lab using a UIC Model 120 Total Carbon Analyzer, which heats a sample in an oxidizing environment, oxidizing all carbon to CO_2 and evolving numerous other non-carbon containing gases. These other gases are scrubbed away using several chemical scrubbers, and the CO_2 then continues to a UIC model 5014 CO_2 coulometer, previously described in the carbonate section. Total carbon is determined via coulometric titration. A comparison of total carbon results obtained by the IPST analytical lab and contracted Huffman Laboratories of Golden, Colorado can be seen in Figure 11. Very similar results were obtained, with all results within 3%.

4.9 Residence Time Determination

Residence times were determined for the experiments by using the computational fluid dynamics package of Gambit and Fluent. First, a three dimensional grid of the PEFR was created in Gambit. In order to reduce computational time only one quarter of the cross-section for the reactor was modeled, with symmetry boundary conditions used on the radial planes. 0.3 meters of the injector were modeled so that the primary gas would have a parabolic velocity profile upon entering the reactor, and only the first 1.2 meters of the reactor was modeled, which corresponds to the farthest collector position used in the study.
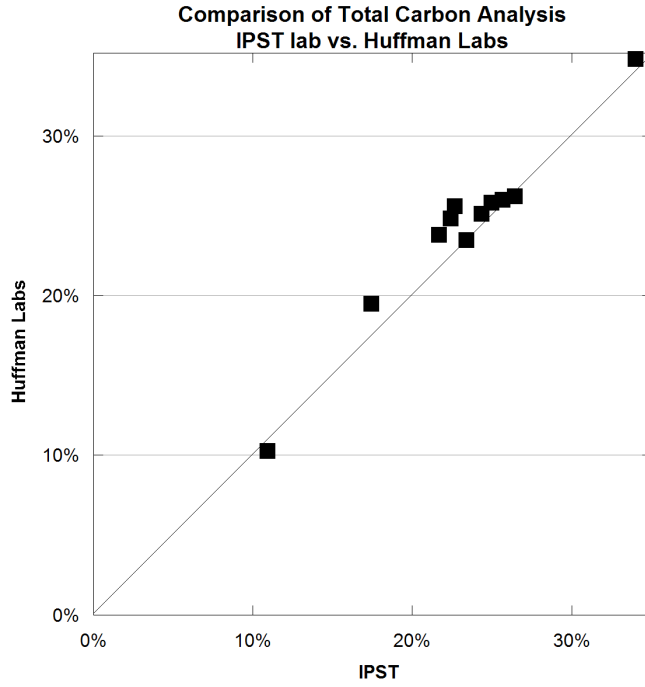
Figure 11: Total carbon analysis comparison

A picture of the reactor geometry is shown in Figure 12.
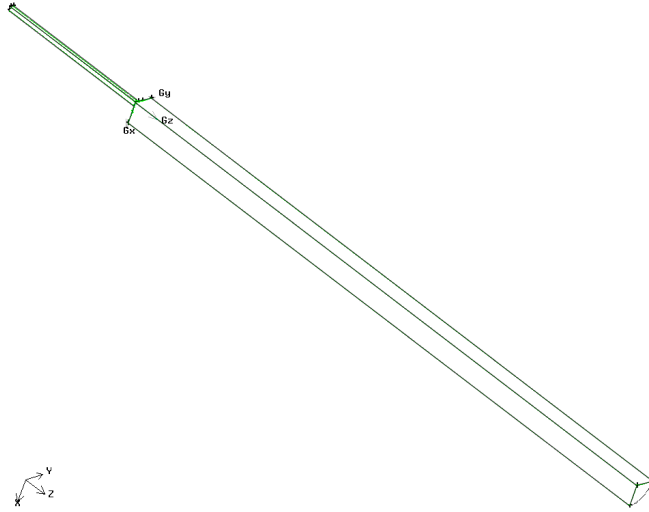
Figure 12: View of PEFR geometry

The grid was structured so that the grid sizes were smaller near the center and the beginning of the reactor, the areas of maximum interest. Figure 13 shows a detailed picture of the beginning of the reaction section, where the injector meets the larger reactor section.

Subfigure *a* shows the different zones present at the beginning of the reactor: blue for the injector, yellow for the secondary gas inlet, and red for the reactor wall. Subfigure *b* shows the grid structure for the same area.

(a) Entrance Zones   (b) Entrance Grid
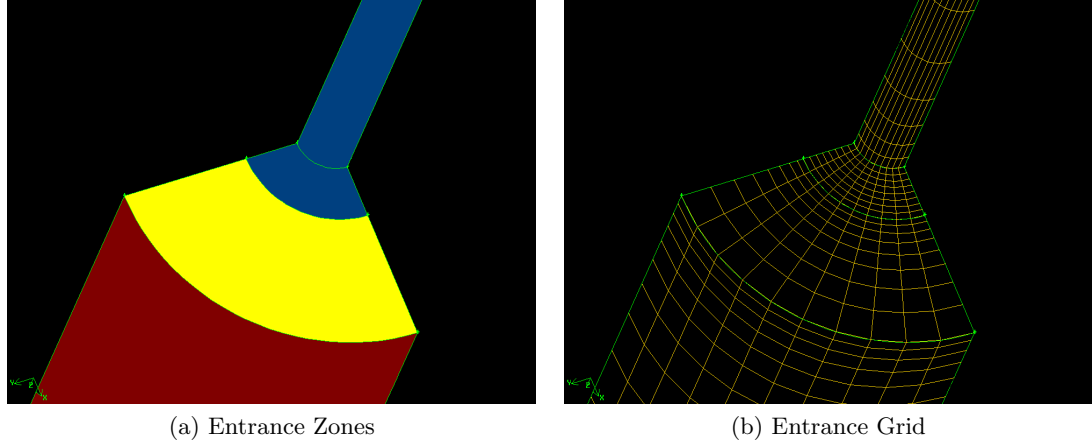
Figure 13: Reactor geometry detail: Reactor Entrance

Table 16 has the PEFR dimensions that were used to model the reactor, and Table 17 has a list of the boundary conditions used in the model.

Table 16: 3-D PEFR model dimensions

Parameter	Value	Units
Injector ID	14	mm
Injector OD	34	mm
Injector Length	300	mm
Reactor ID	82	mm
Reactor Length	1200	mm

Table 17: 3-D PEFR model boundary conditions

Zone	Type	Condition
Primary Inlet	Mass Flow Inlet	Per experiment, T = 300K
Secondary Inlet	Mass Flow Inlet	Per experiment, T = 1173K
Injector Wall	Wall	T = 300K
Injector End	Wall	T = 300K
Reactor Wall	Wall	T = 1173K
Outlet	Pressure Exhaust	$T_{backflow} = 1173K$
X-plane	Symmetry	
Y-plane	Symmetry	

Once the geometry was created the three dimensional mesh was imported into Fluent 6.1.22 for modeling. The set points and conditions (temperature, pressure, mass flows) used for the constant partial pressure runs were used to determine residence times. Once the gas phase flows and temperatures were established, particles were injected into the model at the beginning of the injector. The particle diameters and densities corresponded to the characteristics of the short residence time pyrolysis chars generated at each pressure. The mixture of reaction gases was assumed to have viscosity and thermal conductivity close to that of nitrogen, the main component. The viscosity and thermal conductivity used a four-point temperature profile with linear interpolation in the model. See Table 18 for specific model inputs for the simulations.

Table 18: 3-D PEFR model inputs

Input	Value				Units
	5 Bar 20cm/s	5 Bar 30cm/s	10 Bar	15 Bar	
1° Mass Flow	$3.65{\times}10^{-5}$	$5.47{\times}10^{-5}$	$7.30{\times}10^{-5}$	$1.04{\times}10^{-4}$	kg/s
2° Mass Flow	$3.68{\times}10^{-4}$	$5.51{\times}10^{-4}$	$7.20{\times}10^{-4}$	$1.08{\times}10^{-3}$	kg/s
2° Mass Fraction CO_2	16.6%	16.6%	8.5%	5.7%	
2° Mass Fraction H_2O	3.4%	3.4%	1.7%	1.1%	
D_{ab} CO_2	$3.61{\times}10^{-5}$	$3.61{\times}10^{-5}$	$1.79{\times}10^{-5}$	$1.19{\times}10^{-5}$	m^2/s
D_{ab} H_2O	$5.77{\times}10^{-5}$	$5.77{\times}10^{-5}$	$2.91{\times}10^{-5}$	$1.94{\times}10^{-5}$	m^2/s
Particle Density	30.3	30.3	54.6	65.6	kg/m^3
Particle Diameter	30.2	30.2	40.1	47.7	μm
Model ID #	1	2	3	4	

Table 19 shows which model numbers, as shown in Table 18, correspond to which experiments. Even though the gas composition changed between the types of experiments performed, the total number of moles input at the primary and secondary inlets remained constant at the various pressure/velocity combinations. The conservative assumption was therefore made that even though changing the gas composition slightly changes the Reynold's number, a model using the correct molar addition rate of gases would accurately represent residence times regardless of input gas composition.

Table 19: 3-D PEFR model number and experiment correlation

Total P. Bar	Avg. Vel. cm/s	Model ID#		
		Const. P. Press.	Const. Mole Frac.	Pyrolysis
5	20	1		
5	30	2	2	2
10	20	3	3	3
15	20	4	4	4

4.10 Process Considerations

It is important when studying heterogeneous kinetics that no step other than the intrinsic chemical kinetics limit the rate of reaction. Therefore, particle sizes, reaction conditions, gas compositions, and many other items must be considered prior to conducting experiments. Engineers have developed several dimensionless numbers that attempt to characterize systems based on the relative importance of these items. Table 20 gives a partial summary of the dimensionless numbers and other information that has been considered for these experiments. Also included is a brief description of each number.

Preliminary estimates of these values were obtained prior to the thesis proposal in order to verify that the experiments were in a kinetically limited regime. After the experiments were completed these estimates were updated with experimentally determined values. These calculations were made separately for 5, 10, and 15 bars of pressure by using the characteristics of the short residence time pyrolysis chars, which were generated at each pressure. Detailed calculations for these numbers can be found in Appendix B.

Particle Reynolds Number

This number was determined by first assuming a spherical geometry for the particle. The terminal velocity of the particle was calculated by equating the drag force on the particle with the force of gravity [58].

$$F_{drag} = 6\pi\mu_g r v_{terminal} \tag{32}$$

$$F_{grav} = \frac{4}{3}\pi r^3 (\rho_{part} - \rho_{gas})g \tag{33}$$

$$v_{terminal} = \frac{2r^2(\rho_{part} - \rho_{gas})g}{9\mu_g} \tag{34}$$

Table 20: Process considerations for system

Item	Description
Particle Reynolds Number	Ratio of inertial to viscous forces
Schmidt Number	Ratio of momentum to mass diffusivity
Sherwood Number	Used to calculate mass transfer coefficients
Prater Number	Indicates magnitude of non-isothermality due to reaction
Biot Number	Relates the heat transfer inside and at the surface of a body
Weisz Modulus	Indicates magnitude of intra-particle concentration gradients
Thiele Modulus	Indicates importance of internal diffusion to overall rate of reaction
Effectiveness Factor	Ratio of actual rate of reaction to external surface rate of reaction
M.T. Limited Burnout Time	Time to complete reaction assuming film mass transfer limited
Film ΔT	Film temperature gradient assuming film mass transfer limited rate of reaction
Intra-particle ΔT	Particle temperature gradient assuming film mass transfer limited rate of reaction
Oxidizing gas to C_f ratio	Molar ratio of CO_2 and H_2O to C_f in experiments

ρ_{part}, the char bulk density, was determined from mercury intrusion data, r the mean volume radius determined by laser light scattering, and μ_g and ρ_g the viscosity and density, respectively, of N_2 at 900°C from NIST [1].

The Reynolds number was then calculated by

$$Re_p = \frac{v_{terminal}\rho_g L}{\mu_g} \tag{35}$$

where L was the mean volume diameter determined by laser light scattering.

Schmidt Number

The Schmidt number was calculated by the equation

$$Sc = \frac{\nu_g}{D_{a,mix}} \tag{36}$$

where ν_g is the kinematic viscosity of N_2 at 900°C from NIST.

$D_{a,mix}$ is calculated in a two-step approach. First, binary diffusion coefficients for water-nitrogen, water-carbon dioxide, and carbon dioxide-nitrogen are calculated for experimental

conditions. Second, these coefficients are adjusted for a ternary mixture. The binary diffusion coefficients are calculated by adjusting experimentally determined inter diffusion coefficients for binary systems (located in Table 2.5 of Hines and Maddox [32]) to the system temperature and pressure via equation 2.16 in Hines and Maddox,

$$D_{ab,T_2,P_2} = D_{ab,T_1,P_1} \frac{P_1}{P_2} \left(\frac{T_2}{T_1}\right)^{3/2} \frac{\Omega_{T_1}}{\Omega_{T_2}}$$

where P_1 and T_1 are at 1 atmosphere and approximately 300K, P_2 and T_2 are at experimental conditions, and Ω is the Lennard-Jones collision integral for the specified temperature.

Once D_{ab} for water-nitrogen, water-carbon dioxide, and carbon dioxide-nitrogen are determined they are inserted into equation 2-55 of Hines and Maddox [32]

$$D_{a,mix} = (1 - X_a) \div \left(\sum_{j=2}^{n} \frac{X_j}{D_{aj}}\right) \tag{37}$$

where n is 3 and X is the mole fraction of the component in the system.

Sherwood Number

The Sherwood number is calculated by the relationship

$$Sh = 2 + 0.552(Re_p)^{1/2}(Sc)^{1/3} \tag{38}$$

which can be found in Eq. 6.149 of Hines and Maddox [32], where Re_p is the particle Reynolds number and Sc is the Schmidt number.

Prater Number

The Prater number, symbolized as B_i, is calculated via the relationship

$$B_i = \frac{(-\Delta H_{r_i})D_{i,eff}C_{i,surf}}{k_{part}T_{surf}} \tag{39}$$

where i represents either water or carbon dioxide, C_{surf} is the concentration of the component at the particle surface, assumed to be equal to the gas phase concentration, and T_{surf} is the surface temperature of the particle, which will be discussed later. k_{part} is the thermal conductivity of the particle, which was calculated by the equation

$$k_{part} = (1 - \epsilon)k_{bl} + \epsilon k_g \tag{40}$$

where ϵ is the experimentally determined porosity, k_g is the thermal conductivity of nitrogen at 900^oC from NIST [1], and k_{bl} is the thermal conductivity of anthracite coal as found in Appendix 2 of Kreith and Bohn [40]. ΔH_r is the heat of reaction of carbon gasification at 900^oC. This was calculated by first determining the standard heat of reaction by equation 4.15 in Smith, Van Ness, and Abbott [70]

$$\Delta H_0^o = \sum_i \nu_i \Delta H_{fi}^o \tag{41}$$

where ΔH_0^o is the standard heat of reaction, ν is the stoichiometric coefficient in the gasification reaction, and ΔH_{fi}^o is the the standard heat of formation of each component in the gasification reaction. The heat of reaction is then adjusted to 900^oC via equation 4.18 of Sm. V.N. and Ab.,

$$\Delta H^o = \Delta H_0^o + R \int_{T_o}^{T} \frac{\Delta C_p^o}{R} dT \tag{42}$$

where ΔH^o and ΔH_0^o are the heats of reaction at reaction conditions and the reference temperature, respectively. Values for $\Delta C_p^o/R$ were determined from Appendix C of reference [70]. $D_{i,eff}$ is the effective diffusivity of the component inside the particle, calculated by combining equations 2-62 through 2-64 in Hines and Maddox [32]

$$D_{i,eff} = \frac{\epsilon}{\tau} \left[\frac{1}{\frac{1}{D_{i,k}} + \frac{1}{D_{i,mix}}} \right] \tag{43}$$

where ϵ is the experimentally determined porosity, τ is the particle tortuosity (assumed to be 7), $D_{i,mix}$ as previously described, and $D_{i,k}$ the Knudsen diffusivity of the component i in the particle. $D_{i,k}$ was determined by Hines and Maddox equation 2.61

$$D_{i,k} = 97.0r \left(\frac{T}{M_i} \right)^{1/2} \tag{44}$$

where T is the reaction temperature in Kelvin, M_i is the molecular weight, r is the average pore radius, and $D_{i,k}$ is in units of m^2/s. The average pore radius was calculated via H&M equation 2.62

$$r = \frac{2\epsilon}{S\rho_b} \tag{45}$$

where ϵ and ρ_b are porosity and bulk density as determined by mercury porosimetry, and S is the specific surface area of the particle as determined by nitrogen adsorption. Since

the surface area changed as a function of carbon conversion, the maximum surface area for each char was used to determine pore radius.

Prater numbers were calculated for water and carbon dioxide separately and combined to give an overall Prater number for the particles.

Biot Number

The Biot number is calculated via equation 2.81 in Kreith and Bohn [40]

$$Bi = \frac{hL_c}{k_{part}} \tag{46}$$

where k_{part} is the thermal conductivity of the particle as described above and L_c is the characteristic length of the particle, equal to volume/surface area. Assuming spherical geometry, L_c reduces to r/3, where r is the mean volume radius as determined by laser light scattering. h is the convective heat transfer to the particle, and is calculated by equation 7.10 from Kreith and Bohn [40]

$$h = C_{p,g} V_{term} \rho_g \left(\frac{2.2}{Re_p} + \frac{0.48}{\sqrt{Re_p}} \right) \tag{47}$$

where $C_{p,g}$ and ρ_g are the heat capacity and density of nitrogen from NIST and V_{term} is the terminal velocity of the particle. A convective heat transfer equation could not be found that was valid in the extremely low Reynolds number range for these particles. This equation is valid for Reynolds numbers between 1 and 25, so a value of 1 was used for these calculations.

Weisz Modulus

There are several monikers that are applied to the same equation which uses experimentally determined data to quantify the magnitude of internal diffusion resistance in a particle. Levenspiel [42] alternately refers to this as the Weisz Modulus, Wagner Modulus, or Wheeler-Weisz-Wagner Modulus

$$M_w = L^2 \frac{(-r_a'''/C_a)_{obs}}{D_e} \tag{48}$$

where $-r_a'''$ is the volumetric rate of reaction, C_a is the concentration in the gas phase, L is r/3 for spherical particles, and D_e is the effective diffusivity in the particle. Fogler [16]

refs to this value as the Weisz-Prater Criterion (Eq.12-61)

$$C_{wp} = \frac{-r'_{a,obs}\rho_c R^2}{D_e C_{a_s}}$$

(49)

where $-r'_{a,obs}$ is a mass based rate of reaction, ρ_c is the density of the catalyst, R is the radius of the catalyst, D_e is the effective diffusivity inside the catalyst, and C_{a_s} is the concentration at the surface of the particle.

For this study a modified Weisz modulus has been used, based on the previous work of Li and Van Heiningen [44]

$$M_w = \frac{r\rho_{c_f}L^2}{M_c C_{gas} D_{eff}}$$

(50)

in which r is the rate of fixed carbon conversion as determined by the slope of the conversion vs. time plots for the constant partial pressure gasification experiments, M_c is the molecular weight of carbon, and L is r/3 of the char particle. ρ_{c_f} is the density of fixed carbon in the char, which is determined by the initial concentration of fixed carbon in the black liquor based on the average of 32 samples tested and the experimentally determined density of the pyrolysis chars. C_{gas} is the total molar concentration of oxidizing gases in the system. D_{eff} is 1/3 the effective diffusivity of H_2O plus 2/3 the effective diffusivity of CO_2, since the partial pressure of carbon dioxide was twice that of water. The terminology used will be Weisz Modulus, which reflects Levenspiel's choice to use a characteristic length that is the same as the lengths used in other calculations.

Thiele Modulus

The Thiele modulus was calculated by combining equations 12-58 and 12-61 in Fogler [16]

$$C_{wp} = 3(\phi_1 coth\phi_1 - 1)$$

(51)

which equates the Weisz-Prater Criterion C_{wp} to the Thiele Modulus, ϕ_1. The value of ϕ_1 can be directly calculated from the value of the Weisz-Prater Criterion, which is equivalent to the Weisz Modulus.

Effectiveness Factor

The effectiveness factor of the particles is calculated by equation 18.24 of Levenspiel [42]

$$M_w = M_T^2 \epsilon$$

(52)

58

where M_w is the Weisz Modulus, M_T is the Thiele Modulus (equivalent to ϕ_1 in Fogler), and ϵ is the effectiveness factor (equivalent to η in Fogler). The effectiveness factor can be calculated directly from this equation.

Mass Transfer Limited Time to Burnout

The mass transfer limited time to burnout was calculated by the first determining the mass transfer limited gasification rate,

$$r_{MT\ limited} = 4\pi r^2 (k_{c_{H_2O}} C_{H_2O} + k_{c_{CO_2}} C_{CO_2}) \tag{53}$$

where k_c is the mass transfer coefficient, r is the mean radius as determined by light scattering, and C is the constant partial pressure concentration of the oxidizing gases in the bulk phase.

The mass transfer limited rate was then used to calculate the time to gasify all the carbon in a particle, shown in equation 54,

$$t_{burnout} = \frac{4/3\pi r^3 \rho_b \rho_{c_f} \times 1000}{r_{MT\ limited}} \tag{54}$$

where r is the mean radius as determined by light scattering, ρ_b is the bulk density of the char as determined by mercury porosimetry, and ρ_{c_f} is the concentration of fixed carbon in the black liquor in moles per gram of BLS.

Film ΔT

The film temperature gradient was calculated by performing a steady state heat balance on an individual black liquor particle by stating that

$$(heat\ consumed\ by\ gasification) + (heat\ from\ convection) + (heat\ from\ radiation) = 0 \tag{55}$$

The heat consumed from gasification was determined by

$$q_r = \sum_{i=1}^{2} [\Delta H_i^o \times r_{mt,i}] \tag{56}$$

where ΔH^o is the previously described heat of reaction at experimental conditions and r_{mt} is the mass transfer limited rate of reaction, based on the amount of carbon present and the previously described mass transfer limited time to burnout, and i is CO_2 or H_2O.

The heat from convection was calculated by

$$q_c = h_c S(T_s - T_g) \tag{57}$$

where h_c is the convective heat transfer coefficient (described in Biot Number), S is the surface area of the char using the volume average diameter and spherical geometry, T_s is the surface temperature of the char particle, and T_g is the gas temperature surrounding the particle.

The heat from radiation was calculated from equation 1.18 of Kreith and Bohn [40]

$$q_{rad} = A_{rad} \mathbf{F} \epsilon_{rad} [T_s^4 - T_{rad}^4] \tag{58}$$

where A_{rad} is the area of radiation (assumed to be 100mm of reactor tube length), $\mathbf{F}$ is the view-factor between the particle and the radiating surface (assumed to be 1.0), ϵ_{rad} is the emittance of the radiating body (assumed to be 0.8), T_s is the particle surface temperature, and T_{rad} is the radiating temperature (assumed to be 900°C).

The resulting equation,

$$\sum [\Delta H^o \times r_{mt}] + h_c S(T_s - T_g) + A_{rad} \mathbf{F} \epsilon_{rad} [T_s^4 - T_{rad}^4] = 0 \tag{59}$$

was solved by assuming a gas phase temperature, T_g, and iteratively solving for T_s.

Intra-particle ΔT

The intra-particle temperature difference was calculated by performing a steady state spherical shell balance around a char particle.

$$(Energy\ in) - (energy\ out) + (energy\ consumed) = \frac{d(energy)}{dt} = 0 \tag{60}$$

After performing the shell balance and applying the appropriate boundary conditions

$$BC\ \#1: \ \frac{dT}{dr} = 0 \ @ \ r = 0 \tag{61}$$

$$BC\ \#2: \ T = T_s \ @ \ r = R \tag{62}$$

the following equation results:

$$T = T_s + \frac{Q}{6k}(R^2 - r^2) \tag{63}$$

where T_s is the surface temperature as previously determined, Q is the volumetric heat generation term calculated by dividing the mass transfer limited heat of reaction, q_r, by the volume of a char particle, k is the thermal conductivity of the char particle (as previously discussed), R is the volume average radius of the char particles, and T is the temperature at any point r inside the particle.

Oxidizing Gas to Fixed Carbon Ratio

In order to determine chemical kinetics in the PEFR it must be run as a differential reactor. This means that a sufficient excess of oxidizing gases must be present in the reactor so that their concentration remains unchanged as the black liquor particles react. This excess, however, must be balanced with the fact that the equilibrium species present at the experimental conditions must be representative of actual gasifiers, and will be discussed in Chapter 4. The ratio was calculated by

$$\frac{Q_{CO_2} + Q_{H_2O}}{Q_{bl}\rho_{c_f}} \tag{64}$$

where Q_{CO_2} and Q_{H_2O} are the molar feed rates, known from the mass flow controllers, Q_{bl} is the mass feed rate of black liquor the system (approximately 1.2 grams/minute), and ρ_{c_f} is the previously discussed molar concentration of fixed carbon in the black liquor solids.

Calculated and generally accepted critical values for the above system considerations are located in Table 21. If the values for the system considerations are on the correct side of the critical value then they can be considered to have an insignificant impact on the process.

Table 21: Calculated values for dimensionless numbers

Item	Critical Value	Actual Value			Units
		5 Bar	10 Bar	15 Bar	
Re_p	-	3.07×10^{-4}	2.58×10^{-3}	7.78×10^{-3}	
Sc_{H_2O/CO_2}	-	0.56/0.89	0.55/0.90	0.56/0.91	
Sh_{H_2O/CO_2}	-	2.01/2.01	2.02/2.03	2.04/2.04	
Prater Number	$<$ $\mid 0.1 \mid$	-0.07	-0.03	-0.02	
Biot Number	< 1	9.69×10^{-5}	7.93×10^{-4}	2.27×10^{-3}	
Weisz Modulus	< 0.15	1.67×10^{-4}	4.44×10^{-4}	1.01×10^{-3}	
Thiele Modulus	< 0.4	0.013	0.021	0.032	
Effectiveness Factor	> 0.95	0.999	0.999	0.999	
M.T. Limited Burnout Time	-	3.13×10^{-5}	1.97×10^{-4}	5.00×10^{-4}	sec
Film ΔT	-	0.15	0.10	0.08	^oC
Intra-particle ΔT	-	12.11	6.27	4.44	^oC
Oxidizing gas to C_f ratio	10:1	22:1	15:1	15:1	

The extremely low particle Reynolds numbers are indicative of their low slip velocities in these experiments. The lower values of the Schmidt number for water than carbon dioxide reflect the greater mass diffusivity of water due to its lower molecular weight. At these low Reynolds and Schmidt numbers the value of the Sherwood number is independent of species.

The negative value of the Prater number is due to the endothermic gasification reaction. All values are smaller than the critical value, which means the particles can be treated as having no radial temperature gradients. The Biot number is also used for temperature calculations, but does not take the heat of reaction into account. The low values of the Biot number indicate that heat transfers more quickly through the particle than from the gas to the particle. Just as with the Prater number, this indicates negligible radial temperature gradients at experimental conditions.

The Weisz modulus, Theile modulus, and effectiveness factors are all used to evaluate

the importance of pore diffusion on the rate of reaction. The Weisz and Theile moduli are both less than their respective critical values, indicating that the rate of reaction is much slower than the rate of diffusion inside the particle. An effectiveness factor of unity indicates that the reaction in a particle occurs as fast as if the entire reaction happened at the surface. This is another way of expressing that the kinetics of the reaction are slower than the diffusion in the particle.

The mass transfer limited burnout time is four orders of magnitude faster than the time to burnout indicated by the experimental results. This tells us that mass transfer to the surface of the particle is not a limiting factor in the rate. The film and intra-particle temperature gradients were calculated with the mass transfer limited reaction rates, which are significantly faster than what was actually seen. Even with this conservative assumption, film and intra-particle temperatures gradients were still very low. This means that we can assume isothermality throughout the particle.

The high ratio of oxidizing gases to fixed carbon indicates that the oxidizing gas concentration will vary little as the carbon reacts with it. Therefore the assumption can be made of constant gas phase concentrations, and the reactor can be treated as a differential reactor.

CHAPTER V

EQUILIBRIUM CALCULATIONS

The experiments that were performed in the PEFR had gas-to-solids ratios that were much higher than those of production gasifiers. The main reason for this is because in order to determine kinetic behavior of gasification the PEFR must be run as a differential (as opposed to an integral) reactor. This means that a sufficient excess of reacting gases (with respect to the gasifiable carbon added via the black liquor) must be present in the system so that their concentration remains relatively constant as they react with the black liquor. A constant concentration of H_2O and CO_2 can then be assumed when calculating kinetic values.

Production gasifiers, on the other hand, are run like integral reactors. In a production high temperature black liquor gasifier, substoichiometric amounts of oxidizing gases (either air or O_2) are added to the entrance of the gasifier along with the black liquor. These oxidizing gases then combust a portion of the carbon and hydrogen present in the black liquor, providing CO_2, H_2O, and heat for the endothermic gasification reaction. The concentration of CO_2 and H_2O does vary with position in the gasifier; however particle residence time is long enough for complete conversion of carbon. Additional air or O_2 would increase the amount of carbon that would be converted to CO_2, increase the temperature of the reactor, and decrease the amount of carbon converted to CO. This would decrease the amount of CO and H_2 created, thereby defeating the purpose of gasification.

Since the PEFR is run with a different ratio of oxidizing gases to solids it is important to make sure that the products of the reaction are similar to those of actual gasifiers. The way that this was investigated was by evaluating the equilibrium species present for each of the experiments that were performed. The EQUILIB program of FACTSAGE 5.3.1, a thermodynamic software package, was used for these calculations. After inputting masses and defining conditions, EQUILIB minimizes the Gibbs free energy of the system via the

equation

$$\frac{G}{RT} = \sum n_i \left[\left(\frac{g^o}{RT} \right)_i + ln(a_i) \right] \tag{65}$$

where G is the global free energy, R is the gas constant, T is temperature, n_i is the moles of substance i, g^o is the chemical potential, and a is the activity. Other examples of black liquor gasification equilibrium modeling can be found by Backman and Hupa [4], Zeng [97], and Sricharoenchikul [76].

Phase distributions for elements were determined for all of the experimental conditions investigated. A basis of one minute was used to convert the gas and black liquor feed rates into mass inputs for the program. It is important to note that these calculations represent the species that would be present assuming equilibrium has been reached, irrespective of the kinetics or pathways involved in creating those species. Therefore, the actual species that may be present in the system could differ significantly from the equilibrium species. Nevertheless, given the differences between the PEFR and actual gasifiers, it is important to ensure that representative equilibria are achieved.

5.1   *Procedure in FACTSAGE*

Seven gasification and three pyrolysis equilibria were calculated, as shown in Table 22. The actual molar addition rates of all gases were used in the calculations. This is especially important for the gasification equilibria because the ratio of H_2O to S is important to the phase distribution of sulfur at equilibrium. Black liquor was input to the program as a single stream component of $C_{14.48}H_{15.73}O_{10.6}N_{.04}SNa_{4.23}K_{.14}Cl_{.02}$. This was the elemental analysis of the feed black liquor provided by Weyerhaeuser [77], with oxygen determined by difference. A constant addition rate of 1.2 grams per minute was assumed in all calculations. All equilibrium calculations for the experiments were performed at 900^oC.

Table 22: Equilibrium calculation and experiment correlation

ID	P	Gas		Comments
#	Bar	Moles	Composition (Mole%)	
G1	5	3.33	85% N_2, 10% CO_2, 5% H_2O	5 Bar, 20cm/s, const. partial pressure
G2	5	5	85% N_2, 10% CO_2, 5% H_2O	5 Bar, 30cm/s, const. partial pressure
G3	10	6.66	92.5% N_2, 5% CO_2, 2.5% H_2O	10 Bar, 20cm/s, const. partial pressure
G4	15	10	95% N_2, 3.33% CO_2, 1.67% H_2O	15 Bar, 20cm/s, const. partial pressure
G5	5	5	86% N_2, 10% CO_2, 2% H_2O, 1.72% CO, 0.27% H_2	5 Bar, 30cm/s, const. mole fraction
G6	10	6.66	86% N_2, 10% CO_2, 2% H_2O, 1.72% CO, 0.27% H_2	10 Bar, 20cm/s, const. mole fraction
G7	15	10	86% N_2, 10% CO_2, 2% H_2O, 1.72% CO, 0.27% H_2	15 Bar, 20cm/s, const. mole fraction
P1	5	5	100% N_2	5 Bar Pyrolysis
P2	10	6.66	100% N_2	10 Bar Pyrolysis
P3	15	10	100% N_2	15 Bar Pyrolysis

Screening runs were performed to determine which species would be present at equilibrium. All species that contained greater than 0.01% of a specific element were retained in further calculations. 23 gas phase, 10 liquid phase, and 5 solid phase species were included in the calculations, as shown in Table 23. An ideal solution of K_2S, Na_2S, K_2CO_3, and Na_2CO_3 was created to more accurately predict the destination of sulfur at equilibrium. The binary solution of sodium salts is known to exist, and previous researchers have used mixtures of K_2CO_3, Na_2CO_3, and Na_2S to determine the kinetics of Na_2SO_4 reduction in black liquor [10]. It is generally accepted that the quaternary solution exists as well. However, little is known about the quaternary thermodynamic properties at this time. It was therefore assumed to have ideal characteristics.

Table 23: Species included in equilibrium calculations. * indicates ideal solution

Gas Phase	Liquid Phase	Solid Phase
H_2	Na_2CO_3*	Na_2CO_3
CH_4	Na_2S*	Na_2S
N_2	Na_2SO_3	K_2SO_4
NH_3	Na_2SO_4	K_2S
H_2O	NaCl	
CO	K_2CO_3*	
CO_2	K_2S*	
Na	K_2SO_3	
NaOH	K_2SO_4	
S_2	KCl	
H_2S		
H_2S_2		
CS_2		
SO_2		
COS		
HCl		
NaCl		
$(NaCl)_2$		
K		
KCN		
KOH		
KCl		
$(KCl)_2$		

5.2 Water Gas Shift Reaction

The water gas shift reaction must be considered whenever gasification is occurring with water vapor and carbon dioxide. In the water gas shift reaction, CO and H_2O react to form CO_2 and H_2 in a reversible reaction shown in equation 66.

$$H_2O + CO \rightleftharpoons CO_2 + H_2 \tag{66}$$

While insensitive to pressure due to the equimolar amounts of gas on either side of the equation, the equilibrium concentration is sensitive to temperature, especially in the range of concern for black liquor gasification. This is easily visualized in Figure 14, which shows the equilibrium concentration of equimolar amounts of H_2O, CO_2, H_2, and CO as a function of temperature. Methane is also formed at the lower range of temperatures in Figure 14, but it is not included in the figure.
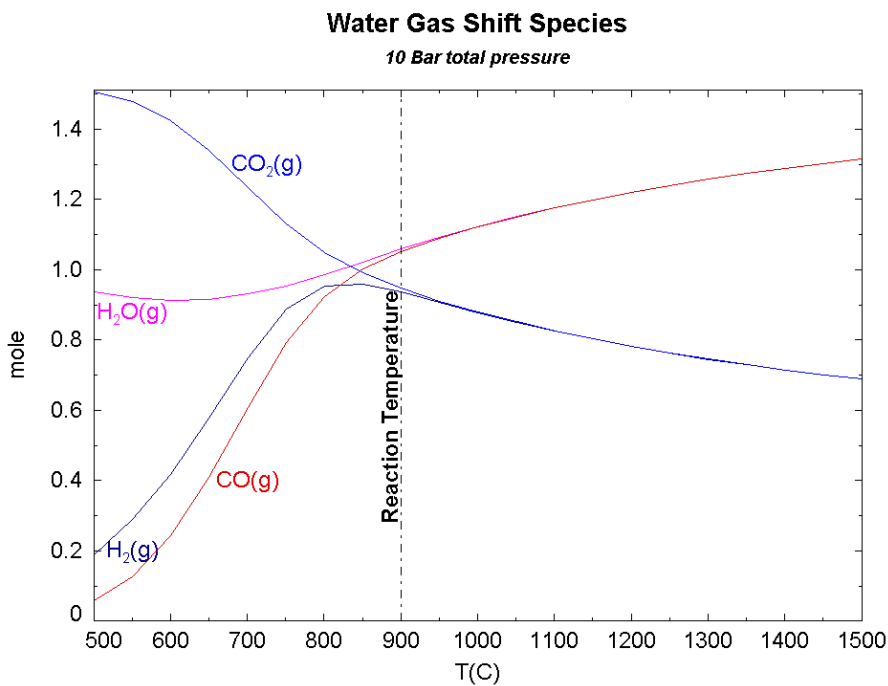
Figure 14: Water gas shift species as a function of temperature. Inputs: 1 mole each of CO_2, H_2O, H_2, and CO; 10 bar total pressure

The relationship between the species involved in the water gas reaction is best characterized by the equilibrium constant, K_{eq}, of the competing forward and reverse equilbria,

shown in equations 67 through 69.

$$H_2O + CO \xrightarrow{k} CO_2 + H_2 \tag{67}$$

$$CO_2 + H_2 \xrightarrow{k'} H_2O + CO \tag{68}$$

$$K_{eq} = \frac{k}{k'} = \frac{[H_2O][CO]}{[H_2][CO_2]} \tag{69}$$

Figure 15 shows a plot of the equilibrium constant for the water gas shift reaction. As can be seen in Figure 15, the equilibrium constant at 900^0C is approximately 0.8.
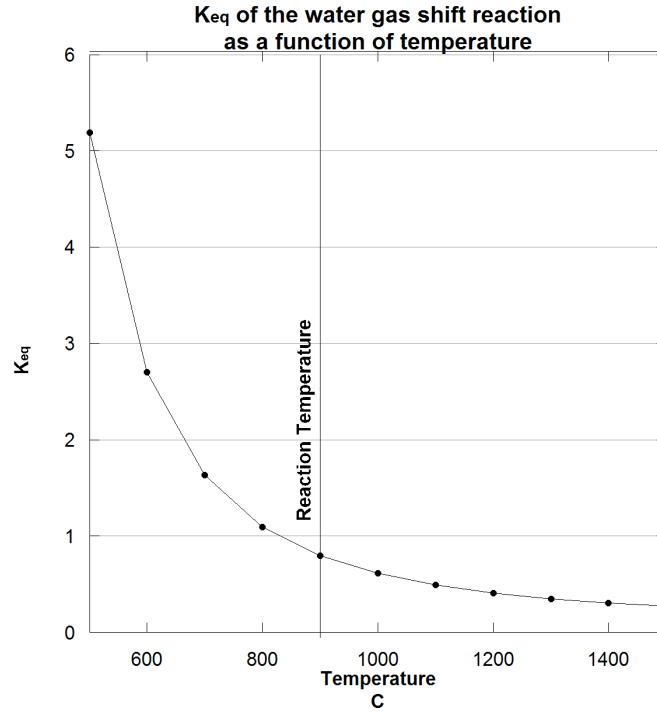
Figure 15: K_{eq} for the water gas shift reaction

The rates of the forward and reverse equilbria, k and k', respectively, will be a function of the product gases, expressed by equations 70 and 71,

$$k = f(P_{H_2O}P_{CO}) \tag{70}$$

$$k' = f'(P_{H_2}P_{CO_2}) \tag{71}$$

where f and f' are temperature dependent functions and P represents the partial pressure of the specified gases. For the constant partial pressure experiments all of the values found

69

in equations 70 and 71 are the same. Therefore the entire system will shift toward the water gas equilibrium at the same rate.

For the constant mole fraction experiments, however, the partial pressure of the gases increase with increasing pressure, possibly changing the rate at which the system approaches water gas equilibrium. Therefore, sufficient amounts of CO and H_2 were added to the constant mole fraction experiments to put the entire system at equilibrium, minimizing the effect of pressure on the rate of water gas shift for these reactions.

5.3   Equilibrium Distribution of Elements at Pyrolysis Conditions

Three equilibrium calculations were performed for pyrolysis at 5, 10, and 15 bars of total pressure and 900^oC. The pyrolysis reactions that occur involve the components of the black liquor only, with nitrogen gas present primarily as a carrier through the reactor. An interesting result of this is that the high oxygen content of the black liquor ($C_{14.48}H_{15.73}O_{10.6}N_{.04}SNa_{4.23}K_{.14}Cl_{.02}$) results in the almost 75% of the carbon being converted to CO at equilibrium, as shown in Figure 16. At all pressures, over 99% of the carbon present in the system exists as either CO or $C_{(s)}$, with the remaining 1% consisting of trace amounts of CH_4, CO_2, and KCN.
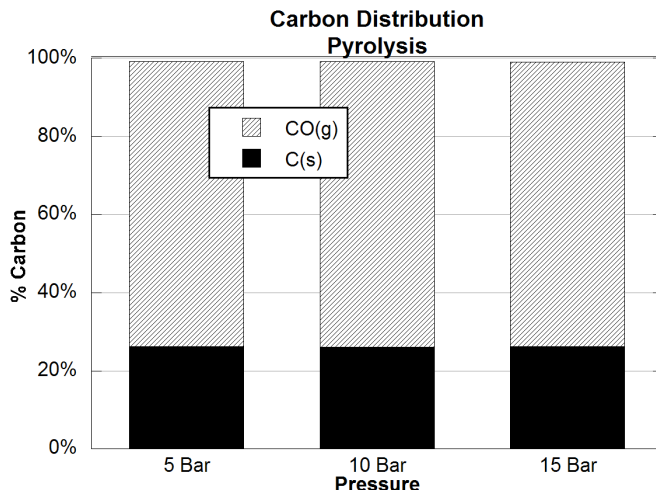
Figure 16: Equilibrium carbon species for pyrolysis experiments. T = 900^oC, 1.2 grams BLS, gas addition given in Table 22.

70

Sulfur was present exclusively as Na_2S for all the pyrolysis pressures. Since this liquor is spray dried and the carrier gas is 100% N_2, no water or carbon dioxide was input to the system. Since very little CO_2 or H_2O was present in the system, the equilibrium amount of H_2S, as shown by equation 72, was low.

$$Na_2S + CO_2 + H_2O \longleftrightarrow Na_2CO_3 + H_2S \tag{72}$$

The hydrogen present in the liquor exists primarily as H_2 because of the oxygen constrained nature of the system. With a oxygen to carbon ratio of 0.73:1 in the liquor, very little oxygen is left over after the formation of CO. The domination of the reduced species in the water gas shift equilibrium (see Equation 66) is the reason why the sulfur remains as Na_2S.

5.4 Equilibrium Distribution of Elements at Gasification Conditions

While in the pyrolysis equilibria carbon is split between the gas and condensed phase and sulfur is only in one, nearly the opposite is true for gasification. Due to the fact that there is at least a 15:1 mole ratio between oxidizing gases and fixed carbon in the black liquor, almost 99% of the carbon input (including reaction gas CO_2 and CO) exists as either CO or CO_2 at equilibrium, with the remaining 1% present primarily as Na_2CO_3. No carbon remains in its elemental form in the gasification equilibria.

The presence of water and carbon dioxide at gasification conditions cause the formation of a significant amount of Na_2S, as shown in Figures 17 and 18. The higher amounts of oxygen present in the system from CO_2 and H_2O allow COS to be formed as well. Figure 17 shows the equilibrium sulfur phase distribution for the constant partial pressure gasification experiments. The predicted equilibrium distribution of sulfur for the 5 bar 20 cm/s, 10 bar, and 15 bar experiments are very similar. The reason for this is twofold. First, the partial pressure of CO_2 and H_2O is constant for all the experiments, causing the equilibrium concentration of Na_2S according to equation 72 to remain constant with increasing total pressure. Second, the molar ratios of CO_2, H_2O, and fixed carbon added to the system were constant for these three sets of experiments. The slight increase in gas phase sulfur in the 5 Bar 30 cm/s graph is due to the slightly higher gas to solids ratio for that experiment, as

71
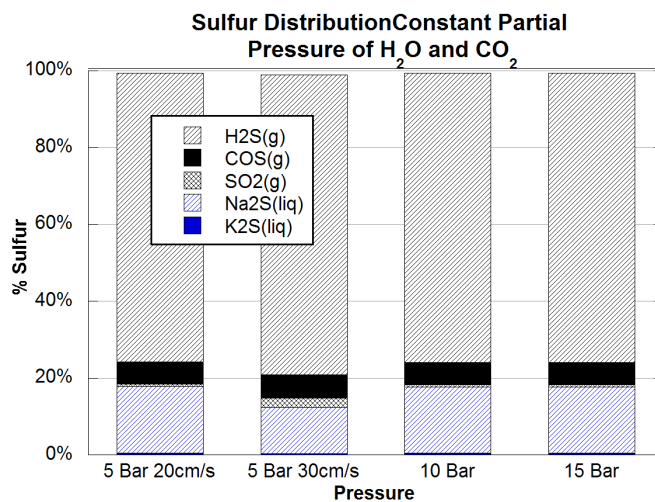
Figure 17: Equilibrium sulfur species for constant partial pressure gasification experiments. T = 900°C, 1.2 grams BLS, gas addition given in Table 22.
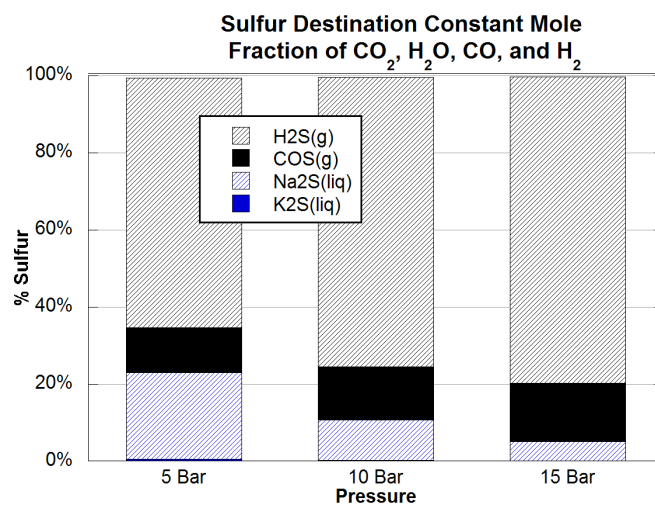
Figure 18: Equilibrium sulfur species for constant mole fraction gasification experiments. T = 900°C, 1.2 grams BLS, gas addition given in Table 22.

shown in Table 21. This results in a higher ratio of H_2O:S, which results in more H_2S at equilibrium.

Figure 18 shows the equilibrium sulfur phase distribution for the constant mole fraction gasification experiments, as outlined in Table 22. For these experiments increasing the pressure increases the amount of sulfur that is present in the gas phase at equilibrium. Again, the reason for this increase is twofold. First, increasing the total pressure at a constant mole fraction will increase the partial pressure of both CO_2 and H_2O, shifting the equilibrium of equation 72 to the right. Second, as shown in Table 22, the constant mole fraction experiments have increasing molar flow rates of gas at increasing pressure. This results in more CO_2 and H_2O being added to the system at a constant amount of sulfur from the black liquor. This results in more H_2S being produced.

A 50% increase in the oxidizing gas to sulfur ratio (as shown by the 5 bar, 30cm/s graph in Figure 17) at a constant partial pressure results in a 360% increase in the amount of SO_2 at equilibrium, indicating the sensitivity of the system to these ratios at the conditions investigated. Despite this sensitivity, in all seven gasification equilibrium calculations the dominant sulfur species present in the gas phase is H_2S. This is representative of the gas phase sulfur seen in production black liquor gasifiers.

5.5 Equilibrium Distriution of Tie Elements at Reaction Conditions

Tie elements are species that are used for mass balance calculations in many high temperature reactions. They are necessary when it is not possible to measure all the materials leaving the system, which is the case for these experiments. Mass is lost by black liquor adhering to the injector, collector, and exhaust piping, among other places. Also, all of the mass converted to the gas phase was not accounted for in these experiments. A tie element allows for the calculation of a char yield (equation 27), which accounts for the mass lost due to the gasification reaction. This char yield is the used to determine the percentage material in the black liquor that remains in the char (equation 28).

Tie elements should remain completely in one phase at the reaction conditions, so that the assumption can be made that all of the tie element that enters the reactor leaves the reactor in the one phase. Calcium is commonly used as a tie element due to its ubiquity and stability to very high temperatures, as shown in Figure 19.
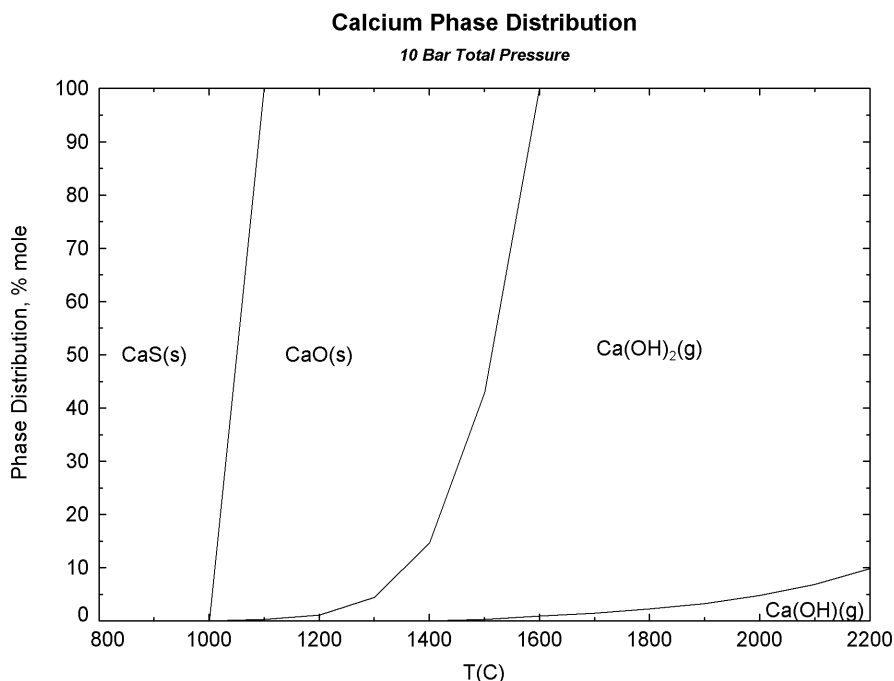
Figure 19: Calcium phase distribution as a function of temperature. P = 10 bar, 1.2 grams BLS, $6x10^{-6}$ moles Ca, gas addition #G3 in Table 22.

Luckily, the black liquor acquired for this study had a very high concentration of vanadium due to the co-firing of #6 fuel oil in the process. Due to several factors previously discussed the vanadium had a much more consistent concentration in the feed black liquor (see Figure 9) than calcium. Figure 20 shows that vanadium remains completely in a condensed solid or liquid phase until approximately $1500^{o}C$, which is $600^{o}C$ higher than the experimental conditions. Therefore, from a thermodynamic standpoint, vanadium is a valid material to use as a tie element.

Vanadium Phase Distribution

10 Bar Total Pressure
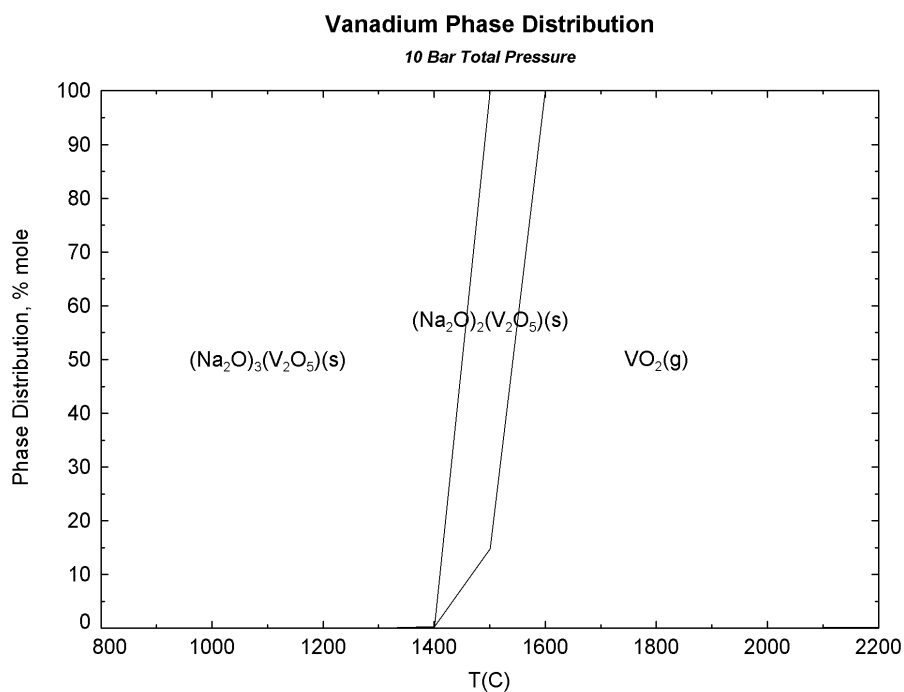
Figure 20: Vanadium phase distribution as a function of temperature. P= 10 bar, 1.2 grams BLS, $6x10^{-6}$ moles V, gas addition #G3 in Table 22.

CHAPTER VI

PHYSICAL CHARACTERISTICS

The effect of pressure on the physical characteristics of black liquor char is an important consideration in the overall effect of pressure on pyrolysis and gasification. Changing pressure can impact characteristics such as porosity, particle size, and pore diameter of the resultant char. Given the large differences in mass diffusion rates between liquids and gases, these changes can significantly impact the diffusive characteristics of the resultant chars.

Given the work by Cetin et al. [12] indicating the importance of heating rate on char morphology, coupled with numerous studies describing the swelling of black liquor during pyrolysis [21, 23, 24, 33], it was concluded that a series of experiments would be performed in which short residence time (approximately 0.9 seconds) pyrolysis chars would be generated. These short residence time pyrolysis chars would then go through a suite of physical characterizations under the assumption that the primary effect of pressure on char physical characteristics would manifest itself at the entrance of the reactor, where the black liquor devolatilizes, swells, and begins pyrolysis. As the char travels down the reactor further physical changes will happen due to ongoing pyrolysis and gasification reactions. Table 24 contains a list of physical tests and corresponding experimental conditions under which the char was formed.

6.1 Microscopy Images

Figure 21 shows SEM micrographs of the black liquor used in the study. The smooth spheres are indicative of the spray drying technique that was used to generate them.

Figure 22 contains SEM micrographs of the short residence time pyrolysis chars generated. As can be seen in the figure, all chars have relatively smooth surfaces with little porosity. Clustering of individual spheres can be seen in the 5 bar char, as well as the tendency toward more individual spheres in the 15 bar char. Subfigures (e) and (f) contain
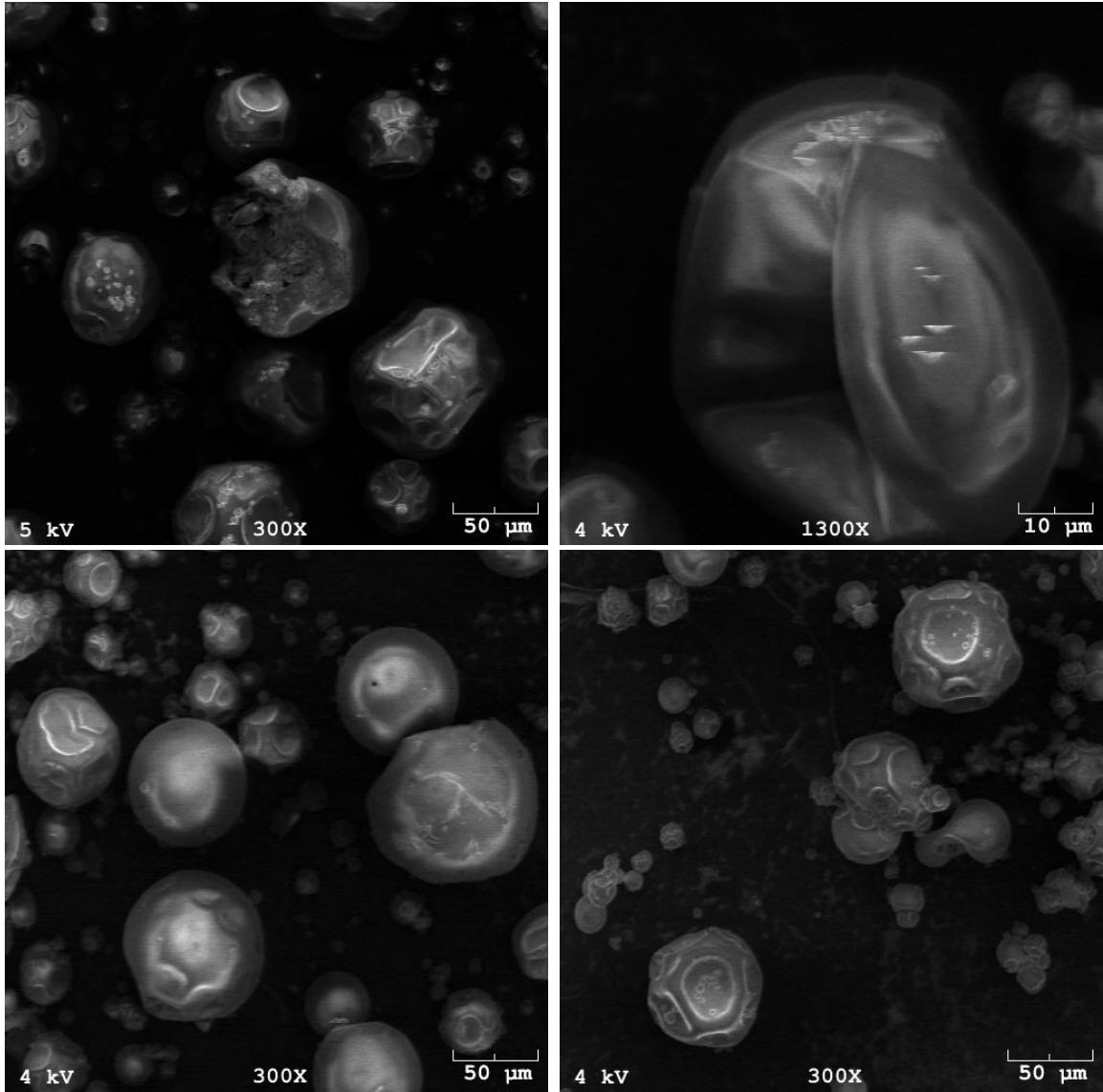
Figure 21: SEM micrographs of 63-75 μm black liquor, spray dried under nitrogen.

Table 24: Physical test and experiment correlation

Test	Method	Material Tested
Particle Size	Light Scattering	Short Residence Time Pyrolysis Char and Black Liquor
Pore Size	Hg Porosimetry	Short Residence Time Pyrolysis Char and Black Liquor
Density	Hg Porosimetry	Short Residence Time Pyrolysis Char and Black Liquor
Porosity	Hg Porosimetry	Short Residence Time Pyrolysis Char and Black Liquor
Surface Area	N_2 Adsorption	Short Residence Time Pyrolysis Char and Constant Partial Pressure Gasification Char
Morphology	SEM	Short Residence Time Pyrolysis Char and Constant Partial Pressure Gasification Char

pictures of hollow spheres of 15 bar char. These hollow spheres were found at all pressures, but the tendency of the 15 bar char to contain individual spheres resulted in the best examples being found in that char. The char morphology is quite different than that of the black liquor which created these chars. The continuous, unbroken appearance of the pyrolysis chars, despite the dramatically different morphology, implies that these chars are plastic during their initial devolatilization and swelling. This is consistent with the body of work involving coal gasification, where the plasticity of char has been well documented [26, 82, 95]. If the chars were not conformable in nature these char particles would appear broken and fractured instead of smooth, continuous spheres. Also, note the similarity between the char in Figure 22 and the pressurized pyrolysis coal char shown in Figure 5. The similarities in behavior and appearance between pressurized black liquor and coal chars implies that there could be some application of the knowledge of pressure on coal char morphology to black liquor.

Figures 23 through 25 show the evolution of the surface area of the 15 bar constant partial pressure gasification char, shown in Figure 39. Note the spheres found in the 36% conversion gasification char in Figure 23, and the similar morphology of the short residence time pyrolysis chars in Figure 22. The rougher spherical surface in the gasification char implies that gas phase CO_2 and H_2O have been removing carbon from the spherical surface,
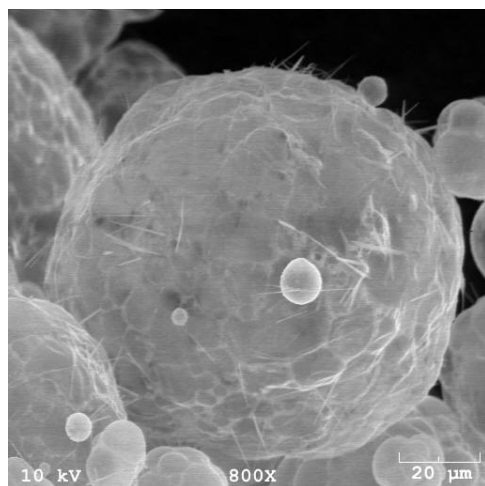
(a) 5 Bar
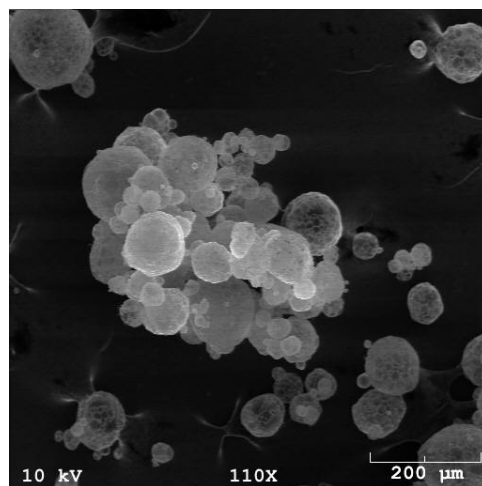
(b) 5 Bar
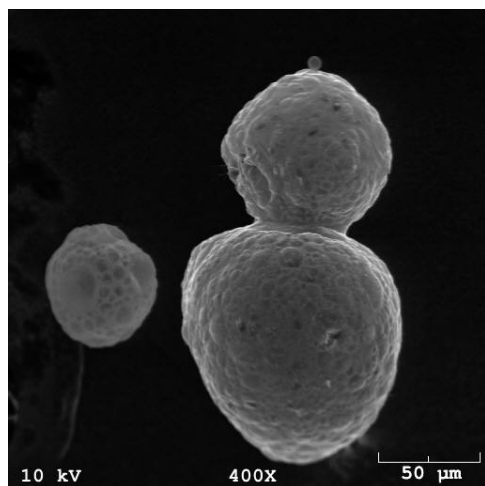
(c) 10 Bar
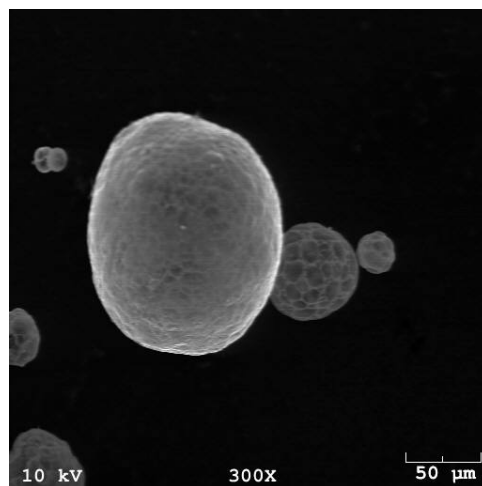
(d) 10 Bar
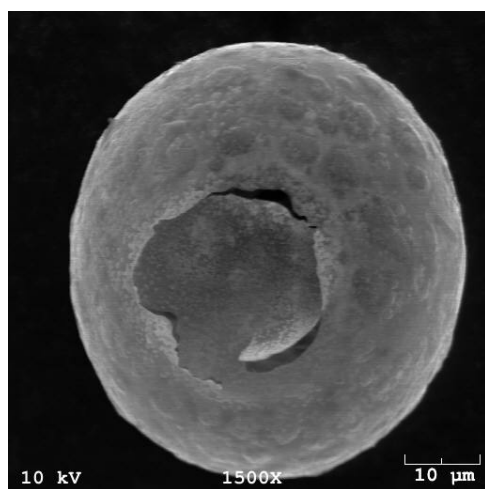
(e) 15 Bar
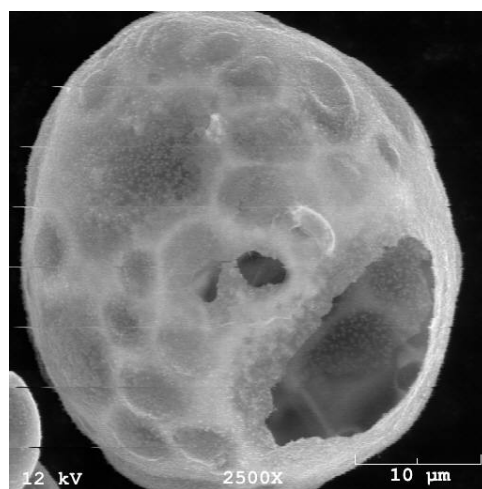
(f) 15 Bar

Figure 22: SEM micrographs of short residence time pyrolysis chars generated in PEFR at 900°C, 100%N$_2$.

where the short residence time pyrolysis chars do not have such surface texture. Also note the presence of char particles that have partially merged together, such as in Figures 22 (c) and Figure 23, which again indicates an initial plastic nature to the char particles. Further evidence of this plastic nature will be discussed later in the chapter.

Increasing the conversion to 71% (shown in Figure 24) significantly increases the porosity and texture of the surface. Figure 24 shows a highly textured, porous char with fine structures. The presence of these fine structures seems to indicate the loss of the previously mentioned plastic nature of the char as the conversion increases, possibly due to thermal degradation of the carbon matrix into more rigid moieties. This corresponds to coal char behavior as well, which is also plastic for a limited time during pyrolysis or gasification [26].

As conversion approaches 100% (shown in Figure 25) the particles again become spherical and less textured. Increasing carbon conversion from 71% to 96% resulted in the removal of the rigid carbon "skeleton" in Figure 24 by gasification. The remaining char is consists mainly of inorganic salts, which are liquid at these temperatures. The surface of the particles is rougher than those in Figure 23, likely due to the high concentration of sodium carbonate, which would form crystals such as those seen here.

All of the particles shown in Figures 21 through 25 were investigated further with porosimetry, light scattering, and surface area techniques (as shown in Table 24). These data will be used to further explain the observations seen in these figures.

For comparative purposes, Figure 26 shows SEM micrographs of coal char gasified by CO_2 at 900^oC and various conversions [51]. Figures 23 through 25 show the morphological changes that black liquor goes through as a function of conversion at 900^oC. Note the huge differences in morphology changes between the two types of char. This is mainly due to the high presence of sodium in the black liquor. Not only does sodium catalyze the gasification reaction, it lowers the melting temperature of the inorganic salts in the char. This allows the black liquor char to return to a relatively low surface area sphere as conversion approaches 100%. The coal char, which has solid salts at 900^oC, is unable to minimize its surface area. What results is an increasingly skeletal particle such as the one shown in Figure 26 (c).
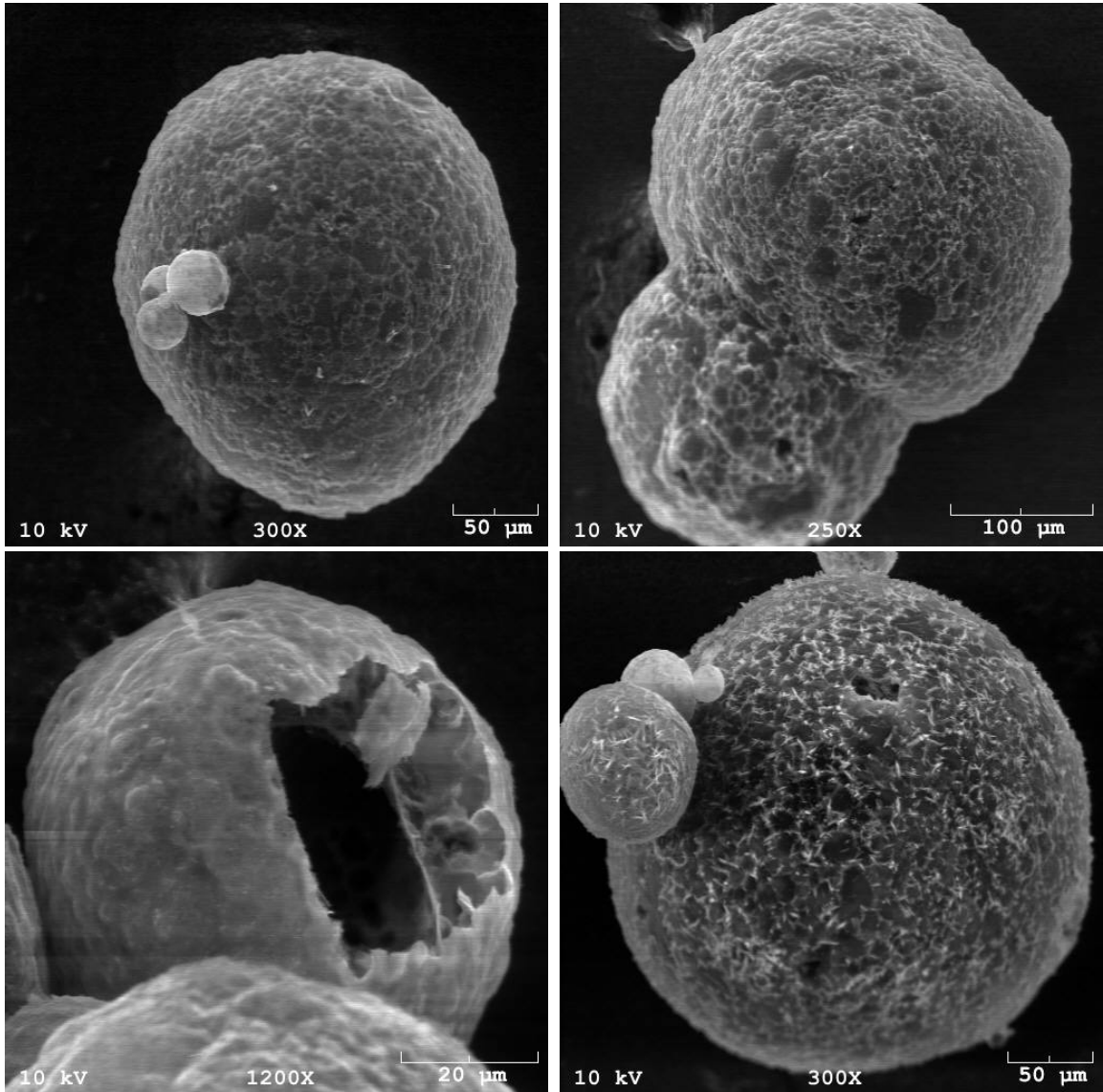
Figure 23: SEM micrographs of 15 bar gasification char, 36% conversion, 4.1 m^2/g. Generated in PEFR at 900°C under 0.25 bar H_2O, 0.5 bar CO_2, balance N_2.
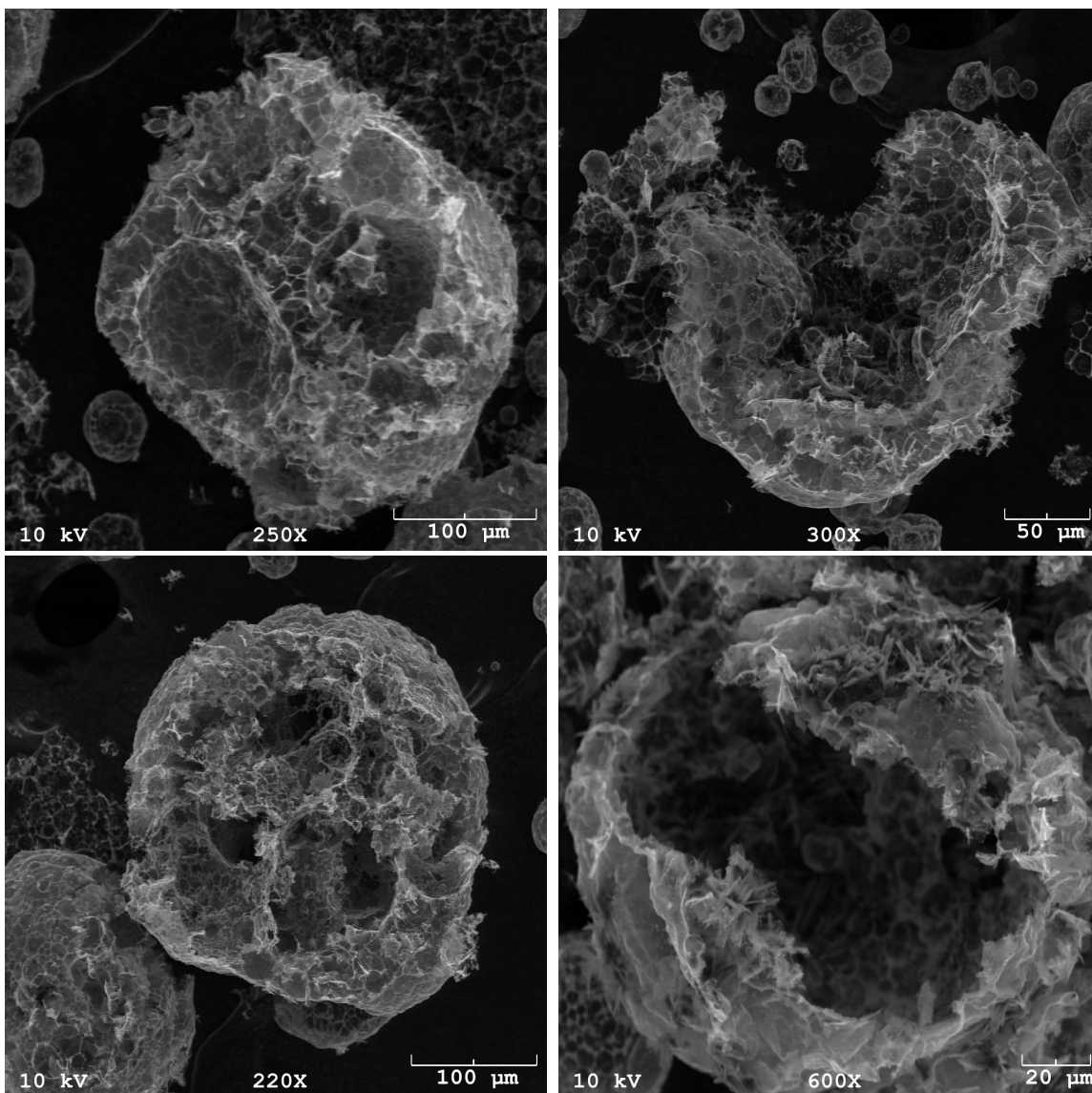
Figure 24: SEM micrographs of 15 bar gasification char, 71% conversion, 115.0 m^2/g. Generated in PEFR at 900^oC under 0.25 bar H_2O, 0.5 bar CO_2, balance N_2.
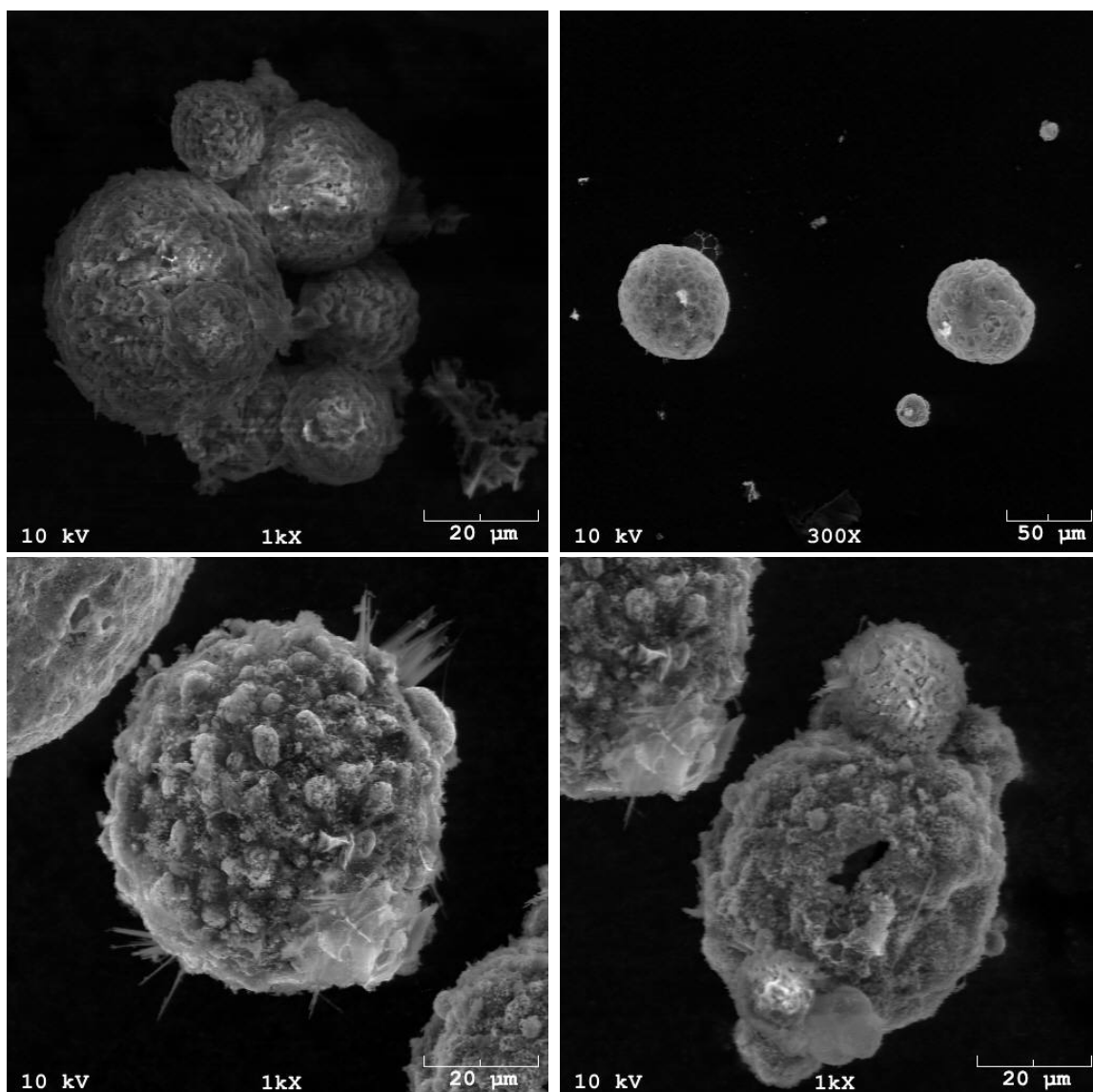
Figure 25: SEM micrographs of 15 bar gasification char, 96% conversion, 7.5 m^2/g. Generated in PEFR at 900°C under 0.25 bar H_2O, 0.5 bar CO_2, balance N_2.
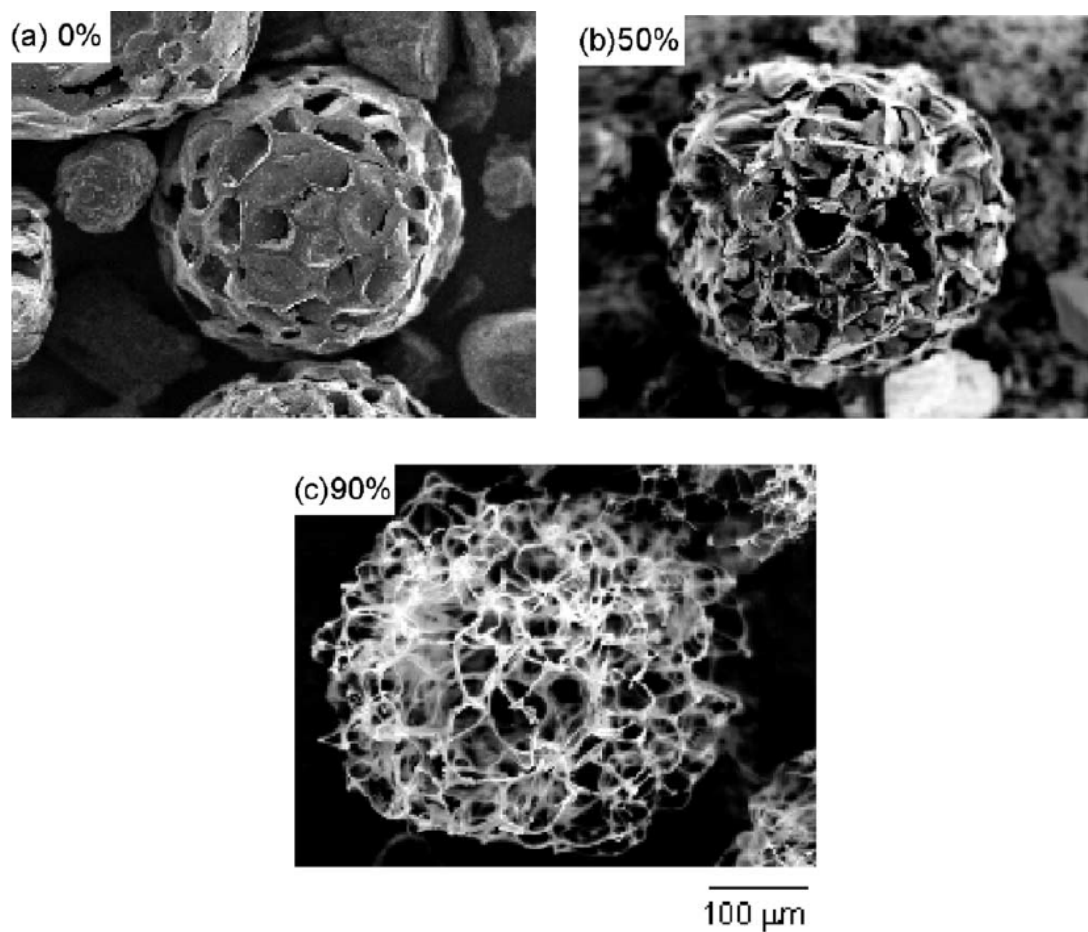
Figure 26: Coal gasification char at various conversions. TGA, 900°C, CO_2

Source: [51]

6.2 Particle Size Distribution

6.2.1 Pyrolysis Char
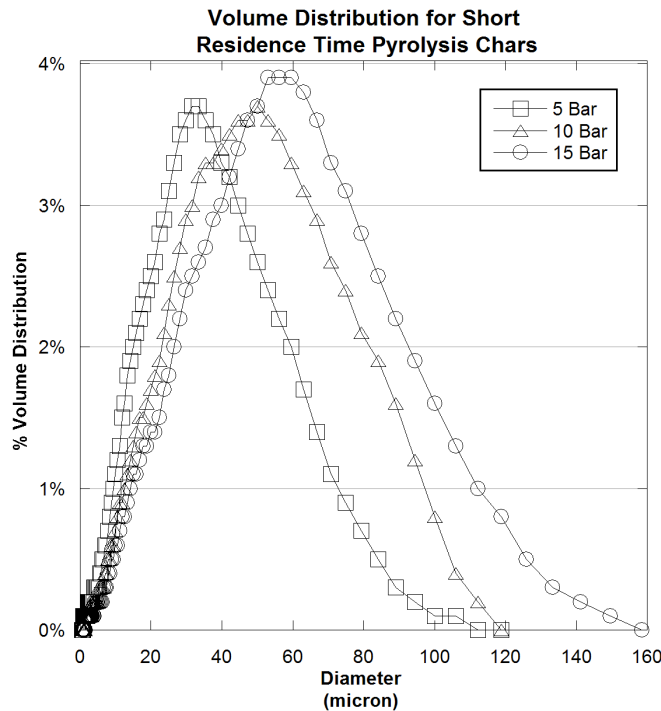
Figure 27: Volume distribution of short residence time pyrolysis chars chars, as determined by light scattering. Generated in PEFR at 900°C, 100%N$_2$, 0.9 second residence time.

Figure 27 shows the volume distribution of 5, 10 and 15 bar short residence time pyrolysis chars. These chars were generated by placing the collector of the PEFR 0.2 meters from the entrance of the reactor and using a constant 20 cm/s of superficial gas velocity through the reactor. The first thing to notice about Figure 27 is that increasing the pressure at which the char is formed increases the average diameter of the char. Second, increasing the pressure widens the particle size distribution, evidenced by the increasing width of the volume distribution curves.

Hundreds of short residence time pyrolysis char particles were examined. It was noted that chars which were formed at higher pressures had a much greater tendency to have both larger individual spheres and large amorphous particles, such as the ones shown in Figure 29. The char formed at 5 bars of pressure (shown in Figure 28 and Figure 22 (a) and (b)) tended to exist as small spheres that were clustered together, suggesting minimal collision
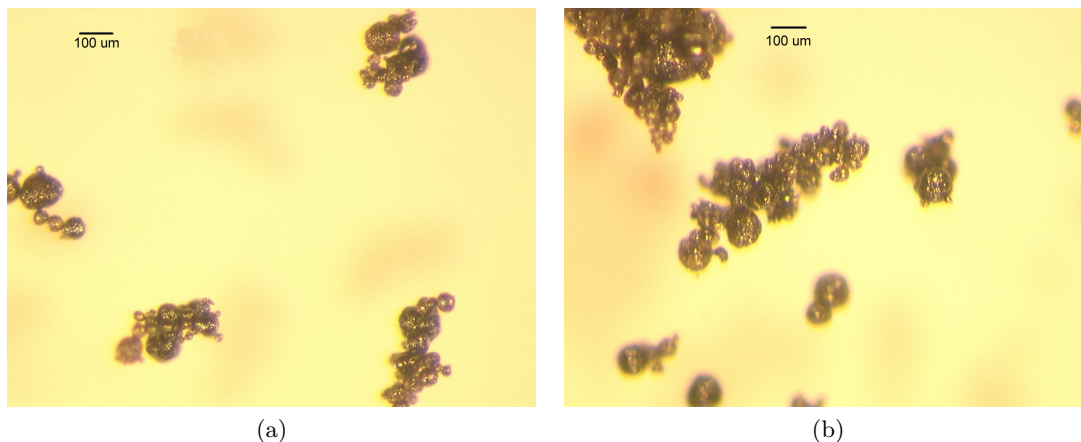
Figure 28: Optical picture of 5 bar short residence time pyrolysis char. Generated in PEFR at 900°C, $100\%N_2$, 0.9 second residence time.
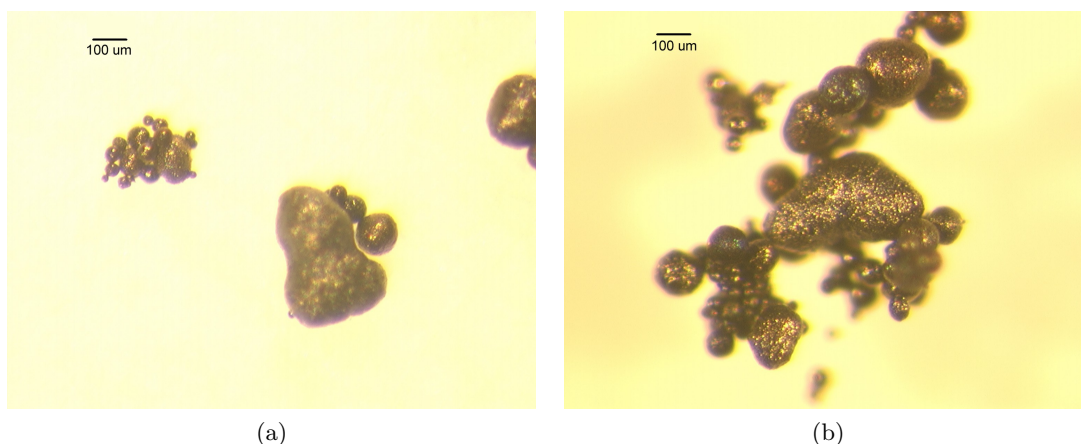
Figure 29: Optical picture of 15 bar short residence time pyrolysis char. Generated in PEFR at 900°C, $100\%N_2$, 0.9 second residence time.

when the particles were present in the reactor and in a plastic state. These clusters probably formed as the particles entered the collector. The constriction of the collector would cause the particles to become very close to each other as they enter. The particles have a sticky surface when they are at high temperatures. The rapid cooling of the particles to below their softening temperature by the quench gas would cause them to be unable to coalesce into larger particles.

This phenomenon of particle collision and coalescence will continue until the quench gas, located at the tip of the collector, cools the particles to below their melting temperature. The result of cooling the particle to below its melting temperature before it has had a

chance to return to a spherical shape are large, amorphous, non-spherical char particles, such as those shown in Figure 29.

Both the increasing average size and increasing distribution of sizes with increasing pressure is due in part to the increasing Reynolds number of the gas phase. The large difference between the interior and outer diameter of the injector (14 and 34 mm respectively, see Table 16) creates a boundary condition of zero velocity at the tip of the injector, where the black liquor enters the reactor. This step-change of velocity, from primary gas to injector end to secondary gas, will induce a zone of separated flow at the entrance of the reactor. This is clearly shown in Figure 30, which is a plot of gas velocity vectors in the 3-D PEFR model colored by radial velocity magnitude.
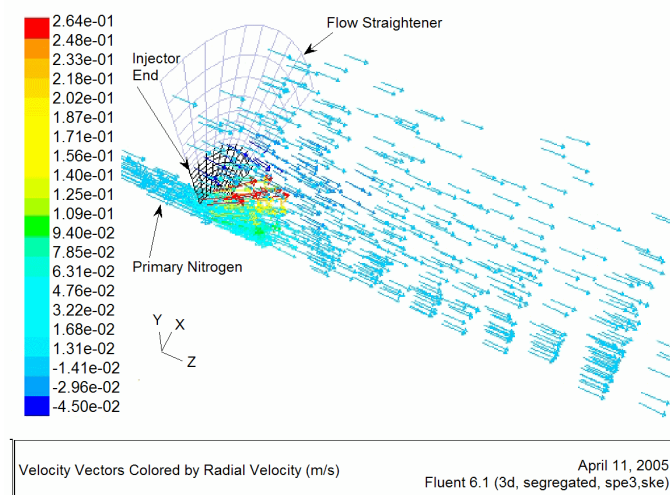
Figure 30: Gas velocity vectors at entrance of reactor from 3-D PEFR model, colored by radial velocity. Boundary conditions shown in Table 17, inputs from Model ID #2, Table 18.

At the tip of the injector, shown as the dark boundary at the end of the reactor, no gas enters the reactor due to obstruction by the injector. The primary gas is shown traveling down the injector and expanding outward as it enters the main body of the reactor. The secondary gases are shown entering the reactor through the flow straightener, shown as the light boundary at the end of the reactor. The zone of separated flow is indicated by the vectors of the secondary gases at the interface of the flow straightener and injector end, shown moving radially inward at approximately 4 cm/s, and the the expansion of the

primary gas outward at approximately 25 cm/s. See Table 17 and Figure 13) for further description of the 3-D PEFR boundary zones, grids, and inputs.

Increasing the pressure from 5 to 15 bars will increase the density of the gas threefold. At a constant gas velocity this will also increase the gas phase Reynolds number threefold, vis á vis equation 73,

$$Re_g = \frac{v\rho L}{\mu} \qquad (73)$$

where v is velocity, ρ is density, and μ is viscosity. This increase in gas Reynolds number would increase the size of the zone of separated flow exhibited in Figure 30. The high heating rate, pressure, and temperature combine to make the char becomes plastic in this zone. As the zone of separated flow increases in size, the tendency of these particles to collide increases as well. Since the char particles are plastic at this point the collided particles will stick together and move to a more spherical shape in an attempt to minimize surface energy.

Another reason why the black liquor char particle size and size distributions increase at higher pressures is due to the increased plasticity of the carbon matrix in the char. Coal chars have been shown to become more fluid or plastic with increasing pressure [26, 95]. This is thought to occur due to the increased time that aromatic radicals are present in the char matrix before becoming primary tars. The same may be true of black liquor chars as well. This would cause an increase in the ability of individual char particles to flow together, resulting in a larger average diameter and wider size distribution.

6.2.2 Black Liquor

Two size fractions of black liquor were used in the experiments to experimentally determine the effect of particle size on gasification rate. The main size used in the experiments was between 75 and 90 μm, with a smaller size cut of 38-53 μm used for a limited number of runs. Unfortunately there was no liquor of the 75-90μm size fraction left by the time samples were sent to the analytical lab for size distribution measurement, therefore the next smaller size fraction of 63-75 μm was sent. Figure 31 shows the volume size distribution of the measured black liquors, with an estimate of where the 75-90 μm size fraction may lie. The actual particle size distributions have a significant volume fraction present that

is below the nominal size range. This is due to the fact that the black liquor behaves like a Geldart class C powder (flour-like in nature) while sieving. This behavior will create clusters of small particles that will be unable to pass through the sieve.
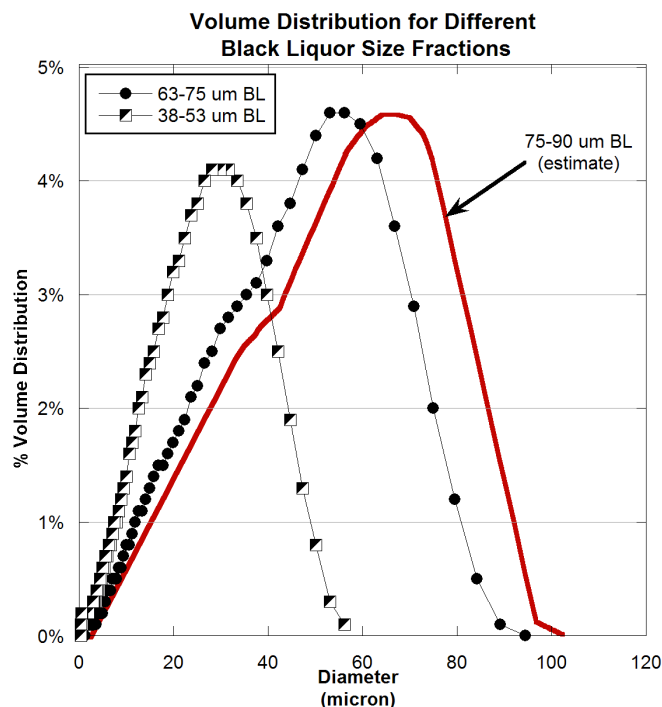
Figure 31: Size comparison of black liquors used in experiments

6.2.3 Black Liquor Size Reduction

Another interesting phenomenon that seems to be occurring is the size reduction and subsequent reagglomeration of the initial black liquor particles. The reagglomeration mechanism is the same as discussed in the previous section. At a fixed distance from the injector, the size of the separated flow zone, characterized by the Reynolds number, would affect the probability of char particles impacting and agglomerating.

Evidence of this physical reduction in size of the particles is shown in Figure 32, where the volume size distributions of 5 bar short residence time pyrolysis char is compared with a size distribution of 63-75 μm black liquor. Since the short residence time pyrolysis char was generated with a 75-90 μm fraction of liquor, the estimate of where the 75-90 μm size cut would lie is on the figure as well.

89
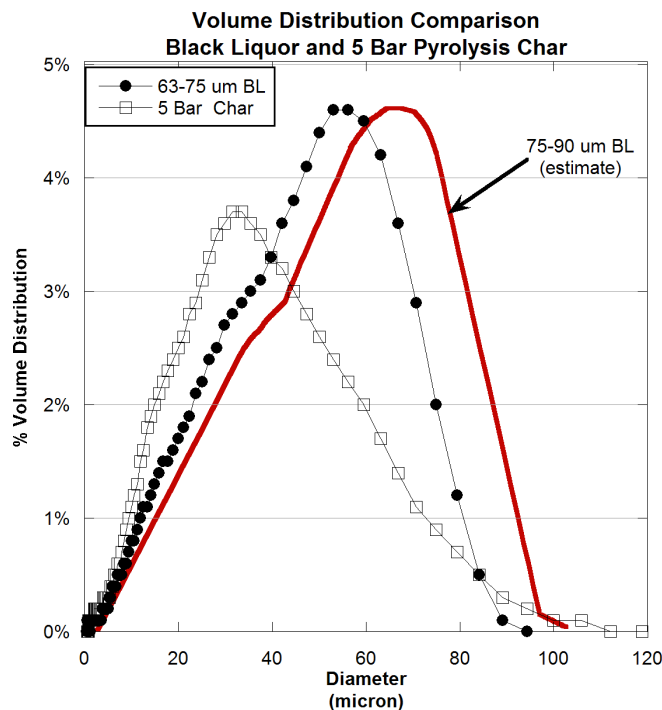
Figure 32: Size comparison of spray dried black liquor and short residence time pyrolysis char, generated in PEFR at $900^{o}C$, 5 bar, 100% N_2

As can be clearly seen in Figure 32, the size distribution of the 5 bar char is significantly smaller than the black liquor from which is was created. Additional data provided from mercury porosimetry (Figures 35 and 37) show that the short residence time pyrolysis chars have bulk densities approximately 5% of the feed black liquor. Therefore, it can be surmised that the only way to conserve mass in a system where the product particles are less dense *and* smaller than the feed particles is to have product particles being generated in the system.

This supposition can be further supported by other data obtained from the short residence time pyrolysis experiments. By knowing:

- Mass of black liquor fed

- Size distribution of black liquor

- Bulk density of black liquor

- Mass of char collected

90

- Size distribution of char

- Bulk density of char

- Mass closure of experiment

one can calculate the ratio of the number of black liquor particles fed in the experiment to the number of char particles collected in the experiment. Results of these calculations are shown in Table 25.

Table 25: Char and black liquor particle number comparisons for short residence time pyrolysis experiments

Pressure Bar	Mass BL g	ρ BL kg/m^3	Mass Char g	ρ Char kg/m^3	# Char Particles # BL Particles
5	10.5	618	6.8613	30.3	6.8
10	11.2	618	4.3614	54.6	0.79
15	10.1	618	5.6172	65.6	0.49

The two main assumptions made in the calculations from Table 25 are 1) spherical geometry for the black liquor and char, and 2) black liquor size distribution for the 63-75 μm size fraction is representative of the actual 75-90 μm size fraction used in the experiment. From the optical and SEM pictures of the black liquor and char the first assumption is not unrealistic. The second assumption will have an effect on the ratio of char to black liquor particles. By assuming a smaller size fraction than what was actually fed, the number of black liquor particles is over estimated, causing the ratio of char to black liquor particles to be under estimated. These two assumptions, however, would have no effect whatsoever on the overall trends shown, as both assumptions would introduce the same error in all calculations.

The trend shown in Table 25 can have two interpretations. The first interpretation is that the tendency for the black liquor to physically blow apart occurs at all pressures, and that the larger zone of separated flow created by the higher gas Reynolds numbers causes these individual small particles to coalesce by collision. The second interpretation is that higher pressure prevents the black liquor particles from blowing apart in the first place, due to the greater PV work needed to expand the particle and the smaller specific volume of the

devolatilization gases at higher pressure. Given the fact that increasing coalesence has been shown with increasing pressure by other methods it is believed that the first interpretation is more accurate.

The size reduction of black liquor particles is due mainly to the high heating rate found in the PEFR, resulting in a rapid evolution of devolatilization gases. There are very small temperature gradients across these particles, as exhibited by their low Biot numbers. Therefore, these gases would be generated throughout the cross-section of the particle. The rapid appearance of these gases, with their extremely high specific volumes in relation to their solid or liquid phases, would create pressures inside the particle that would cause porosity and possibly blow the initial black liquor particle apart as the gases escape. This mechanism of physical ejection has been proposed by Verrill and Wessel [79, 80] for the introduction of sodium into the gas phase during combustion of black liquor.

Experiments were conducted by Frederick [23] in which the effects of solids content on the swelling properties of black liquor was investigated. The study showed that for pine kraft liquors, such as the one used in these experiments, increasing the solids content increased the rate of swelling. Increasing temperature was found to decrease the tendency to swell [24]. These experiments, however, were conducted with much lower heating rates (approx. 10^2 ^{o}C/min) than what is experienced in the PEFR (approx. 10^4 ^{o}C/min). The higher rate of heating would cause a much more rapid and therefore violent evolution of gases, increasing the tendency of the particles to physically blow apart.

6.3   Mercury Porosimetry

Two methods are commonly used to characterize pore sizes: gas adsorption and mercury porosimetry. Gas adsorption is used to characterize microporous structures, and is limited to a maximum pore diameter of approximately 150 Angstroms. Mercury porosimetry is a useful method for materials with meso or macropores, and is valid for pore size characterization from 300 μm to 30 Angstroms in diameter, and is therefore a complementary method to gas adsorption. Materials with a preponderance of micropores also have specific surface areas of several hundred square meters per gram, while materials with larger pores have

much lower surface areas. Given the range of surface areas (approximately 4-19 m^2/g, as measured by N_2 adsorption) for the short residence time pyrolysis chars, it was decided to use mercury porosimetry for pore size characterization.

In addition to pore size information, mercury porosimetry gives information regarding bulk and particle densities. From these measurements the porosity of the particles can be measured. This information is very useful in modeling the reactor and in the calculation of particle properties.

6.3.1 Pyrolysis Char

<u>Pore Size</u>

Figure 33 shows incremental mercury intrusion data for the short residence time pyrolysis chars generated at each pressure. The incremental volume, with units of milliliters of mercury per gram of char, is useful for determining the relative volumes associated with each pore size. The first thing to note in Figure 33 is the presence of pores in the char that are larger than the diameters of the individual particles shown in Figure 27. This can be explained by the fact that these chars exist primarily as clusters of spheres, as shown in Figure 28. During the initial pressurization of the cell, mercury will envelop these clusters of spheres very loosely, not penetrating areas with a dimension smaller than approximately 300 μm. Increasing the pressure will cause this envelope of mercury to tighten around the cluster of spheres, eventually penetrating pores in individual spheres once the pressure is sufficient to do so. The amount of "pores" that are larger than the diameter of the spheres decreases with increasing pressure, which is consistent with the previously stated observation that the higher pressure chars tend to consist of larger, individual spheres as opposed to clusters of smaller spheres.

The 5 bar char contains significant volumes of intrusion from 200 to 0.3 μm with no discernible trends in that range. The 10 bar char appears to contain the emergence of a bimodal distribution, which becomes readily apparent with the 15 bar char. The fact that the bimodal trend emerges as the char formation pressure increases can also be explained by the observation that increasing the char formation pressure decreases the formation of

(a) 5 Bar

(b) 10 Bar

(c) 15 Bar
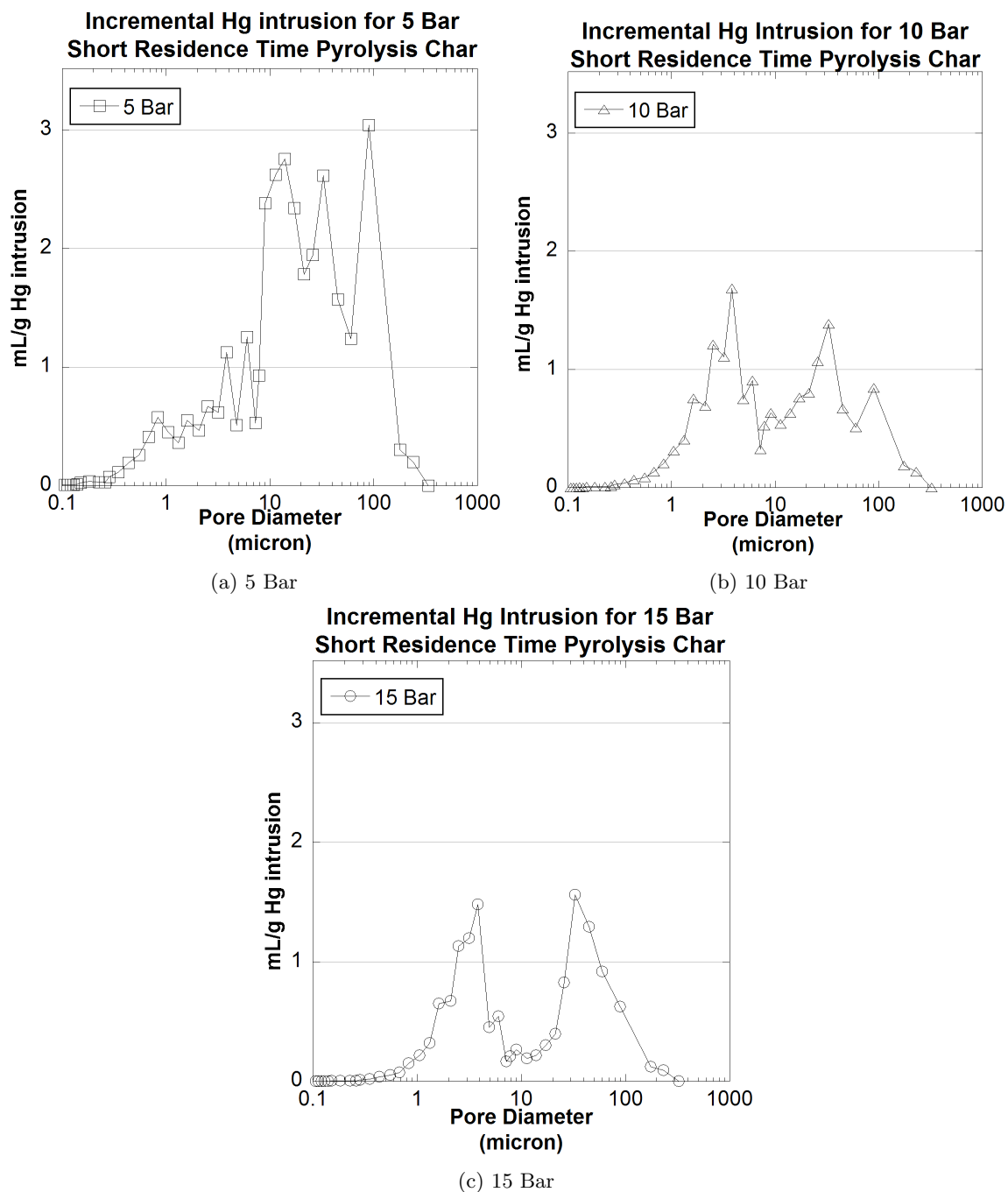
Figure 33: Incremental mercury intrusion data for short residence time pyrolysis chars, generated in PEFR at 900oC, 100%N$_2$

clusters of spheres. The 5 bar char has a continuous region of mercury intrusion because of the high importance of interparticle (as opposed to intraparticle) mercury intrusion in the clusters. Increasing the pressure decreases the amount of interparticle intrusion and

increases the amount of intraparticle intrusion. The right hand node of the 15 bar char signifies the presence of broken, mainly hollow spheres, while the left node signifies the pore sizes present in a relatively continuous hollow sphere. See Figure 22 for SEM pictures of 15 bar char that further illustrate this point.

The statement that the spheres are mainly hollow is supported by other methods as well. First is the mercury extrusion data, which is included in the cumulative mercury data shown in Figure 34. Just as systematically increasing pressure will force mercury into smaller and smaller pores, decreasing the pressure will cause mercury to come out of larger and larger pores. If, however, the pore is not perfectly cylindrical, a hysteresis will occur between the mercury intrusion and extrusion data. This is due to the fact that if there is a localized constriction in the pore, mercury will be trapped in the pore on the side of the constriction closest to the center of the particle. The magnitude of the hysteresis is one way to indicate the number of pores which have such a constriction. As can be seen in Figure 34, the horizontal line of cumulative mercury in the particle indicate that as the pressure is released on the cell almost no mercury is released from the particle. This would be consistent with mercury filling a primarily hollow sphere and then being unable to leave due to the constriction of the particle surface.

The second piece of data that supports the idea that these spheres are hollow is the surface area calculated for the short residence time pyrolysis chars with the assumption of cylindrical pores. By knowing the volume of mercury that penetrates the pore at a given pressure, the surface area of that pore can be calculated by equations 74 and 75,

$$l_i = \frac{\pi D_i^2}{4V_i} \tag{74}$$

$$S.A._i = \pi D_i l_i \tag{75}$$

where D_i is the pore diameter as determined by the pressure, V_i is the volume of mercury penetrated at that pressure, l_i is the length of the cylinder, and $S.A._i$ is the surface area of the cylinder.

When compared with the surface area measured directly from nitrogen adsorption (see Table 26), the surface area calculated with the assumption of cylindrical pores is an order

Cumulative Hg Data for Short Residence Time Pyrolysis Chars
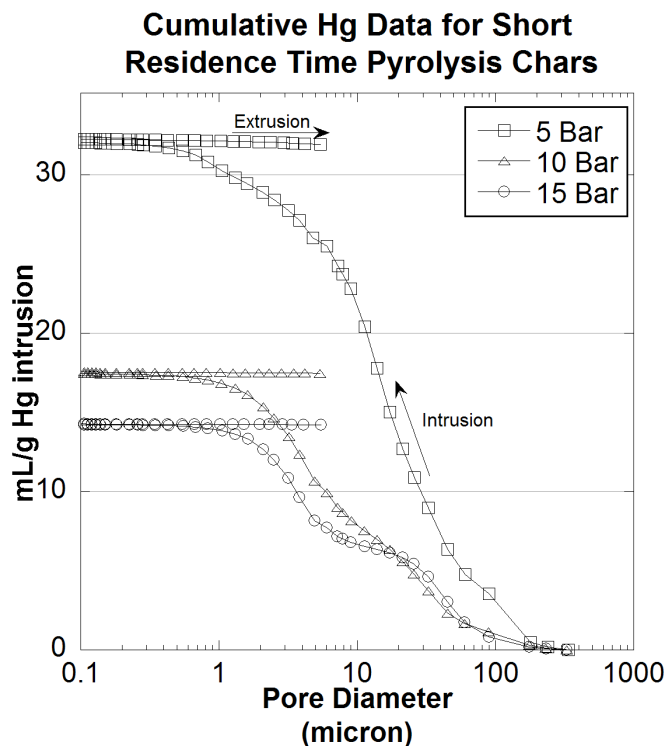
Figure 34: Cumulative mercury intrusion and extrusion data for short residence time pyrolysis chars, generated in PEFR at 900oC, 100%N_2

Table 26: Surface area comparisons for short residence time pyrolysis chars, generated in PEFR at 900°C, 100%N_2. Hg surface area assumes cylindrical pores, BET surface area measured with nitrogen.

Pressure Bar	BET Surface Area m^2/g	Hg Surface Area m^2/g
5	19.0	188.0
10	10.4	203.9
15	4.3	88.1

of magnitude greater, indicating that not only are the pores not cylindrical, but that the volume may exist as one or more large cavities inside the particle. Additional data that supports the supposition of hollowness for the char particles include the ratio of total surface area to external surface area and SEM micrographs, both of which will be discussed later.

Density and Porosity

Figure 35 shows the particle (or skeletal) density, bulk density, and porosity of the short residence time pyrolysis chars. Particle density, or the density of the solid portion

of the black liquor char particle, exhibits no particular trend with respect to pressure and varies between 1100 kg/m^3 at 15 bars to 1600 kg/m^3 at 10 bars. For reference, amorphous carbon has a density between 1800 and 2100 kg/m^3 [63]. No mechanistic explanation can be attributed to this variation in particle density. Given the actual char weights used in the experiments and the particle densities calculated, the volumes used for the particle density measurements were between 0.034 and 0.095 mL. Even a slight fluctuation in volume caused by a sealed pore or other anomaly could easily impact this calculation.
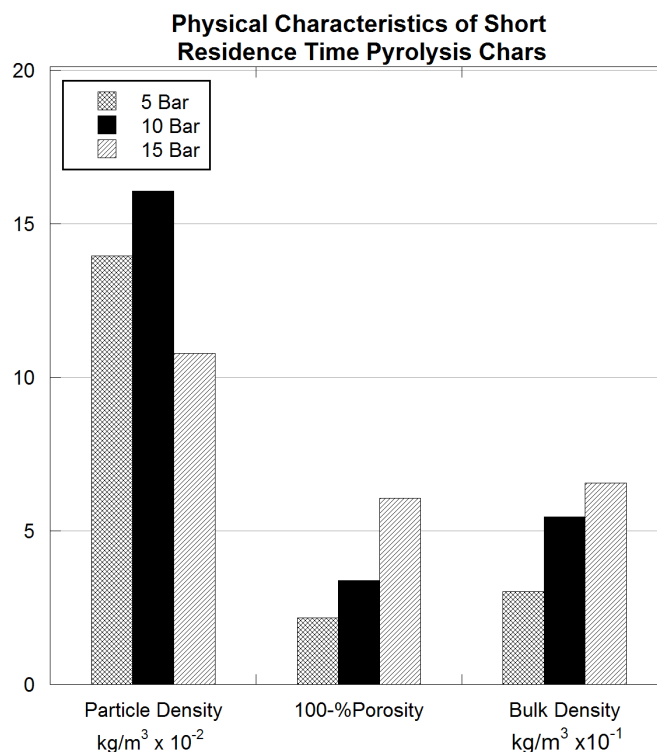
Figure 35: Density and porosity of short residence time pyrolysis chars generated in PEFR at 900°C, 100% N$_2$. From mercury porosimetry data.

The bulk density and porosity measurements are related to each other via equation 76

$$\%Porosity = 1 - \frac{\rho_b}{\rho_p} \tag{76}$$

where ρ_b is the bulk density and ρ_p is the particle density, as described in Table 11. As can be seen in Figure 35, increasing the pyrolysis pressure decreases the porosity. The mechanism is thought to be two-fold. First, increasing the pressure decreases the specific volume of pyrolysis gases generated. If the same number of moles of pyrolysis gas are generated at

higher pressures, less volume of gas would escape the particle. This lower volume of gas would tend to decrease the particle porosity. Second, increasing the pressure would decrease the volume change in the particle. The PV work to expand the particle to a given swollen volume would be greater at higher pressures. However, the amount of energy available for particle expansion would be less, due to the lower volume of pyrolysis gases. Therefore, increasing the total pressure will decrease the change in volume and result in higher bulk densities.

These chars would be classified as cenospheric under commonly accepted coal char classification [82]. SEM pictures show that these chars are primarily hollow spheres, with porosities much greater than the 70% minimum of cenospheric coal chars (see Figure 4). The morphology of this black liquor char is also consistent with the observed tendency of coal chars to have increasing percentages of cenospheric particles with increasing vitrinite content, which is derived from woody biomass and other organics. Black liquor has a very high organic content, making the percentage of hollow, low density, cenospheric char particles very large.

6.3.2   Black Liquor

Pore Size

Figure 36 shows the incremental and cumulative mercury intrusion data for the black liquor used in these experiments. Both plots differ significantly from the short residence time pyrolysis chars. Subfigure (a) shows a single, large increase in mercury intrusion at around 7 μm, as opposed to broad or bimodal distributions in mercury intrusion with the chars (shown in Figure 33) . This indicates that the spray dried black liquor primarily exists as individual particles, with little clustering as seen in the 5 bar short residence time pyrolysis chars. Subfigure (b) shows that approximately 20% of the mercury penetrates the black liquor in less than 0.1 μm pores, as opposed to all of the mercury penetrating the char particles by this point (shown in Figure 34). This indicates a much finer pore structure in the spray dried black liquor than in the char. The replacement of this fine pore structure with much larger pores in the pyrolysis chars further supports the fact that

(a) Incremental   (b) Cumulative
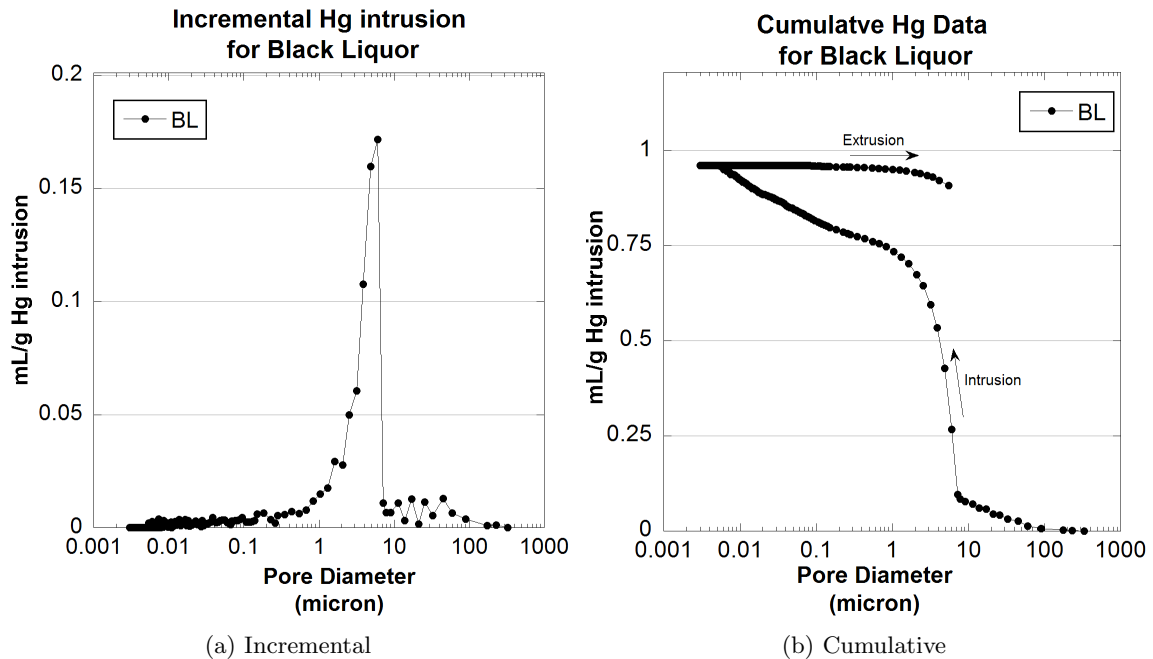
Figure 36: Incremental and cumulative mercury intrusion data for 63-75μm spray dried black liquor

these chars are plastic when they enter the reactor. The evolution of pyrolysis gases causes the relatively dense black liquor with fine pore structure to distend into a hollow, spherical shape. The walls of these spheres have stretched and plasticized to the point where this fine pore structure has been removed. The pores that are remaining consist of holes or broken sections of these spheres. The lower range of the mercury intrusion in Figure 36 verses Figures 33 and 34 is due to the higher density of the black liquor.

Density and Porosity

Figure 37 show the density and porosity of the black liquor used in these experiments. While the particle density is similar to those of the short residence time pyrolysis chars, the porosity is only 62%, as opposed to the 90+% porosity of the pyrolysis chars (shown in Figure 35).
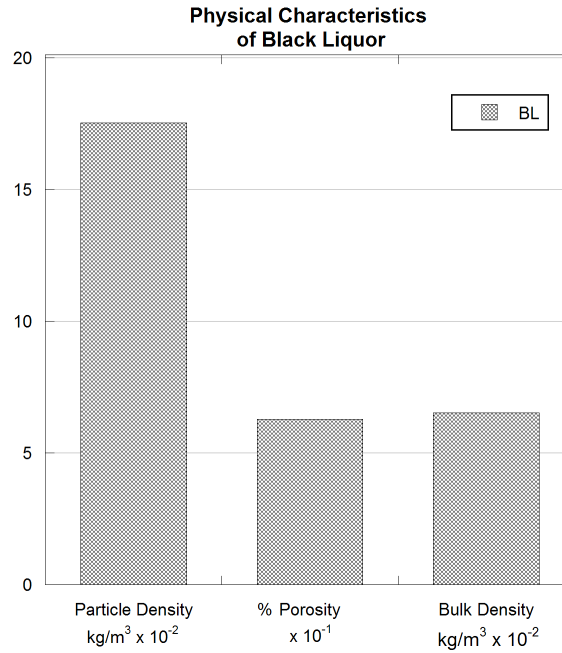
Figure 37: Density and porosity of 63-75μm spray dried black liquor. From mercury porosimetry data
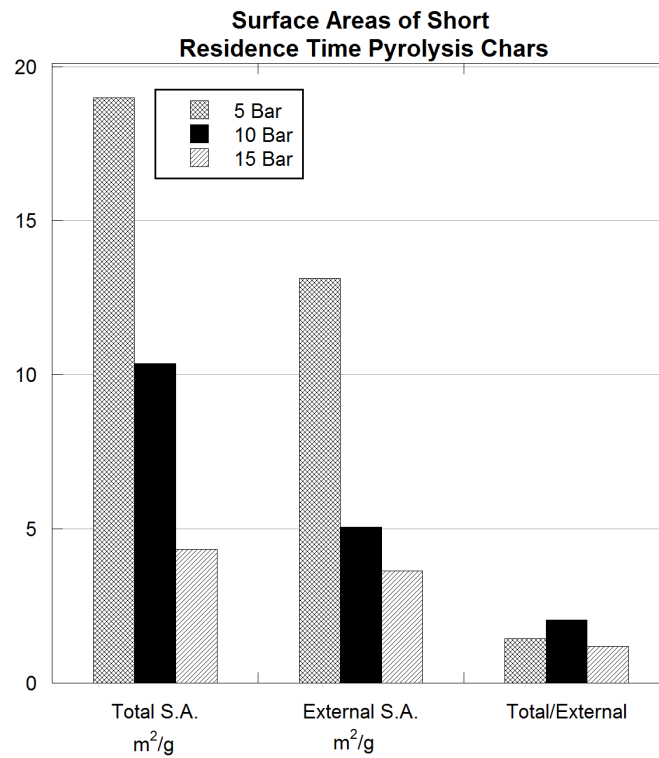
Figure 38: Total and external specific surface area of short residence time pyrolysis chars. Total specific surface area by nitrogen adsorption, external surface area assuming spherical geometry, ρ_b from porosity data, and particle size distribution from light scattering.

6.4   Surface Area

6.4.1   Pyrolysis Char

Figure 38 shows a comparison of total and external specific surface area (assuming spherical geometry) for the short residence time pyrolysis chars. The total specific surface area was determined by nitrogen adsorption using the BET method.

The external specific surface area was calculated by combining light scattering and mercury porosimetry data. First, the total number of spheres was counted from the laser light scattering data using equation 77,

$$n_i = \frac{3V_i}{\pi D_i^2} \tag{77}$$

where n_i is the number of spheres in bin i of the laser light scattering data, V_i is the volume percentage, and D_i is the diameter. The surface area of the spheres, SA_i, for a particular diameter D_i is then calculated,

$$SA_i = n_i \pi D_i^2 \tag{78}$$

Finally, the external specific surface area is calculated using the equation

$$Ext.\ S.A._k = \frac{\sum SA_i}{\rho_k \sum V_i} \tag{79}$$

where ρ_k is the bulk density of the 5, 10, or 15 bar pyrolysis char. As can be seen in Figure 38, the ratio of total to external specific surface areas of the short residence time pyrolysis chars varies between 1.2 and 2.0. This indicates that when the black liquor first enters the reactor and begins to react, the char has very little surface texture or porosity, a fact supported with the scanning electron micrographs shown in Figure 22. The surface area ratio of 1.2 to 2.0 further supports the notion that the short residence time chars are mainly hollow spheres. If these chars were perfect hollow spheres, the ratio of total to external specific surface area would be 2.0.

6.4.2   Gasification Char

Gasification chars were measured using char generated from the constant partial pressure gasification experiments. Five chars from each pressure were selected so that the widest
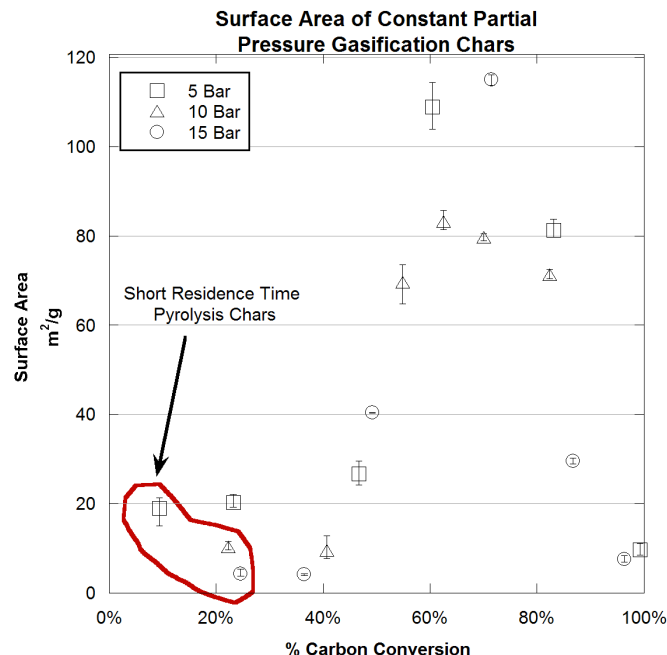
Figure 39: Surface area of constant partial pressure gasification chars generated in PEFR at 900°C, 0.25 bar H_2O, 0.5 bar CO_2, balance N_2.

range of conversions at a given pressure would be measured. The surface area was measured with nitrogen adsorption using the BET method. Figure 39 shows the surface area of these chars as a function of carbon conversion.

A minimum of three replicates were made of each char. The highest and lowest measurement for each specific char are shown with the range indicators. Also included in Figure 39 are the short residence time pyrolysis chars.

The first thing to note in Figure 39 is that the assumption that the pressure effects on char physical characteristics would manifest themselves quickly after the black liquor enters the reactor holds true for surface area. The surface areas of the 5, 10, and 15 bar pyrolysis chars are very similar to the lowest conversion gasification chars at the same pressures. This dependence of surface area on pressure and not conversion seems to hold until about 40% carbon conversion.

After approximately 40% carbon conversion is achieved, surface areas begin to increase quickly until a maximum is reached around 60% conversion. After the maximum surface area is reached, it decreases to approximately 10 m^2/g as conversion approaches 100%. This

increase and decrease in surface area occurs at all pressures. In fact, after 40% conversion the surface area no longer appears to be a function of pressure but instead solely of conversion.

The fact that at low conversions surface area is independent of conversion and a function of pressure is because of the initial devolatilization and pyrolysis of the black liquor. As previously explained, the entrance pressure greatly effects the resultant morphology. Increasing pressure decreases the volume of devolatilization gases created and increases the work required to swell the black liquor. The plastic nature of the char particles is seen in two ways. First, the reduction in fine porous structure of the black liquor (as exhibited by the mercury intrusion characteristics of Figures 36 and 34) shows that the solid phase can plasticize as it expands, sealing the original fine pore structure. Second, the pictures of collided particles (Figures 22, 23, and 29) clearly show that collided particles have the ability to minimize their surface areas by merging together.

This plastic nature of the particles seems to hold true until approximately 40% carbon conversion, when the surface areas begin to increase quickly. At this point the plasticity of the char particles seems to have decreased to the point where surface area minimization is no longer possible. Incremental conversion results in rapid increases in surface area as the fixed carbon is "eroded" away by the gasification reaction. This results in the formation of highly textured, porous structures such as those shown in Figure 24, which shows the maximum surface area of the char at 71% carbon conversion.

Past approximately 71% carbon conversion the surface area begins to decline as the finely textured surface of Figure 24 begins to be gasified and removed. As the fixed carbon is increasingly removed, the ratio of inorganic salts (which are liquid at these conditions) to fixed carbon (which is solid at these conditions) increases. The result is that the particle can again minimize its surface area by the flowing of the liquid salts to a more spherical shape, as shown by Figure 25. The free-flowing ability of the inorganic salts would explain the fact that at 100% conversion the 5 and 15 bar chars have approximately the same surface areas, even though they began the process with a five-fold difference. The predominance of carbonate at high conversions would cause the formation of carbonate crystals on the surface, as seen in Figure 25.
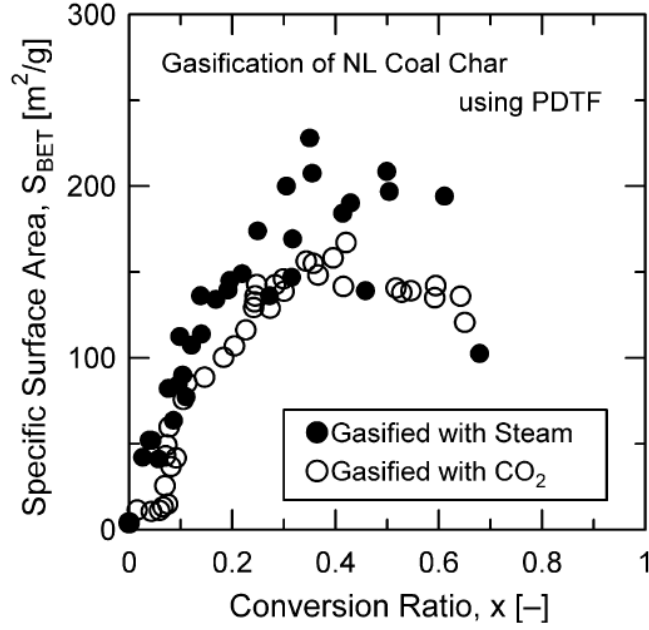
Figure 40: Surface area of coal char at various conversions
Source: [36]

Figure 40 shows a surface area vs. conversion plot generated for coal char in a reactor similar to the one used in this study [36]. The char was pyrolyzed at 1400^oC and atmospheric pressure, collected, and then put into a pressurized drop tube furnace. While the specific gasification conditions for this figure were not listed in the paper, it was somewhere between 2 and 20 bar pressure and 1100 to 1500^oC. Note the similarity between Figures 39 and 40, both in terms of total surface area and the trends exhibited. The coal char achieves a maximum surface area near 40% conversion, while black liquor seems to reach a maximum of near 60% conversion. The black liquor surface area curve occurs under a much tighter conversion range, possibly indicating that black liquor char has a longer plastic stage than coal char. This longer plastic stage would allow conversion to progress further before the char lost plasticity and incremental conversion began to increase the surface area.
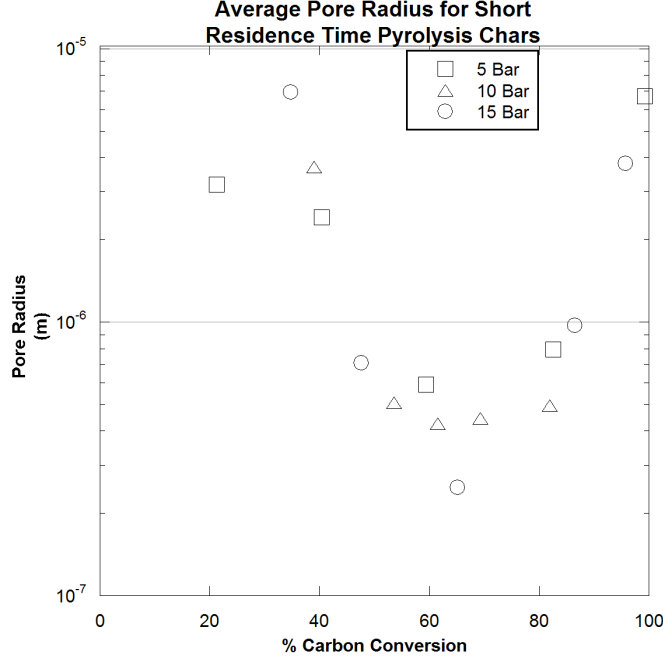
Figure 41: Average pore radius of constant partial pressure gasification chars generated in PEFR at 900^oC, 0.25 bar H_2O, 0.5 bar CO_2, balance N_2. Calculated using equation 80.

6.5   Average Pore Radius

Figure 41 shows the average pore radius of the constant partial pressure gasification chars as calculated by equation 2.61 of Hines and Maddox [32],

$$r_{i,k} = \frac{2\epsilon_k}{S_{i,k}\rho_k} \tag{80}$$

where r is the average pore radius of the ith constant partial pressure gasification char formed at pressure k, ϵ is the porosity of the short residence time pyrolysis char formed at pressure k, S is the surface area of the gasification char, and ρ is the density of the short residence time pyrolysis char formed at pressure k. This equation assumes a constant, cylindrical pore throughout the char particle. While this has been shown to not be true, these calculations can serve to give a worst case scenario regarding diffusion characteristics of these chars.

As can be seen in Figure 41, the average pore radius for the chars changes by over an order of magnitude across the full range of conversion, from a maximum of approximately 7 μm to a minimum of near 0.3 μm. Even though the pore radius decreases by a factor

105

of 20, they are still large enough so that bulk diffusion dominates over Knudsen diffusion, as shown in Figure 55. This decrease in pore diameter can be seen visually in Figures 23 through 25, which show SEM micrographs of 15 bar char at various conversions. The assumptions made in Figure 41 are that the gasification chars have the same porosity and density as the short residence time pyrolysis chars that were formed at the same pressure. The assumption of constant porosity was necessary due to a lack of porosity data versus conversion, and given the previous discussion this may not be correct. The assumption of constant density reflects the observed tendency of higher pressure chars having higher densities across all conversions.

CHAPTER VII

CARBON CONVERSION DURING PYROLYSIS

Oxygen is present in very high quantities in black liquor. The liquor used in this study had an oxygen to carbon ratio of 0.73:1. This high ratio results in a significant amount of carbon being converted to CO without the addition of any oxidizing gases at all (see Figure 16). Therefore, in order to elicit the differences between the conversion of carbon due to internal (in black liquor) vs. external (in CO_2 and H_2O) sources of oxygen, a separate study of black liquor pyrolysis is required.

The study of black liquor pyrolysis also serves to determine the mechanisms for carbon loss, especially at short residence times. By analyzing char collected near the entrance of the reactor, the amount of carbon that was lost during devolatilization can be determined. The amount of devolatilized carbon is important for determining the required residence times for gasification reactors.

7.1   Char Yield

Figure 42 shows the pyrolysis char yields for the experiments conducted under 100% N_2 and 900°C. The points shown are the averages of at least two data points, with the error bars representing the high and low value of each individual point. Yield seems to be independent of pressure, with the 5, 10, and 15 bar data points intermingled at shorter residence times. This finding is consistent with what was found by Whitty and Sandelin [91], whose study is outlined in Table 3. At longer residence times the yield points are more scattered. A slight trend could be found with increasing pressure resulting in a decrease in the rate of yield loss, which is primarily due to differences in the carbon conversion rates between pressures. More will be discussed on this subject later.

With the exception of the shortest five bar residence time, the pyrolysis char yield stays constant at around 90% until approximately two seconds. Based on mass closure
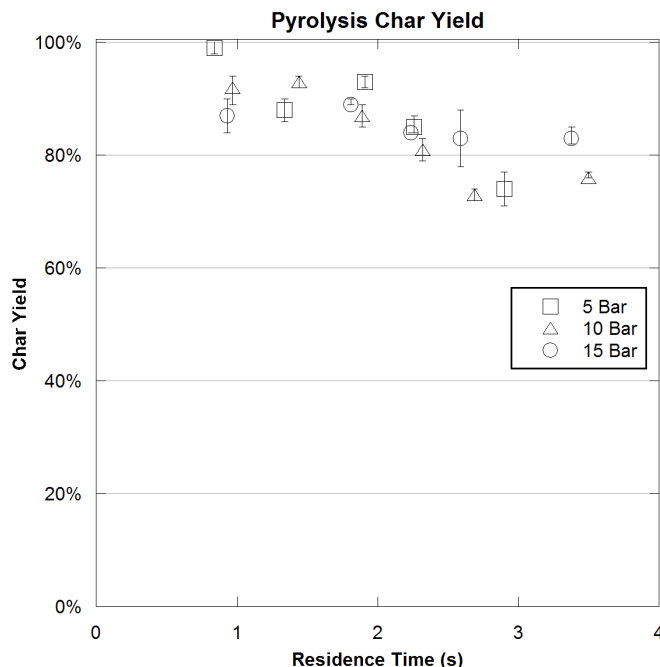
Figure 42: Pyrolysis char yield generated in PEFR at 900^oC, 100% N$_2$

calculations, the 10% mass lost at these short residence times consists mainly of carbon, oxygen, and sulfur, probably lost to the gas phase during the initial devolatilization and swelling of the black liquor.

Yields found for this liquor are approximately 25% higher than those found at similar heating rates under atmospheric pressure [73]. One possible explanation for this is the formation of significant amounts of carbonate reducing the loss of carbon to the gas phase during initial devolatilization. Pyrolysis char yields determined by captive drop experiments, which have lower heating rates and longer residence times, have been shown to be 10-35% lower than the yields in Frederick and Sricharoenchaikul's experiments [22, 73]. Sulfate and carbonate reduction, as well as oxidation of fixed carbon by these reduction products, could be possible for the additional yield loss in these experiments.

After the initial 10% mass loss, however, the yield appears to remain constant until approximately two seconds. This constant char yield is the result of the formation of intermediate carbonates, as shown in Figure 43, which plots the percent of carbonate in the char as a function of residence time. The points are averages of at least two separate
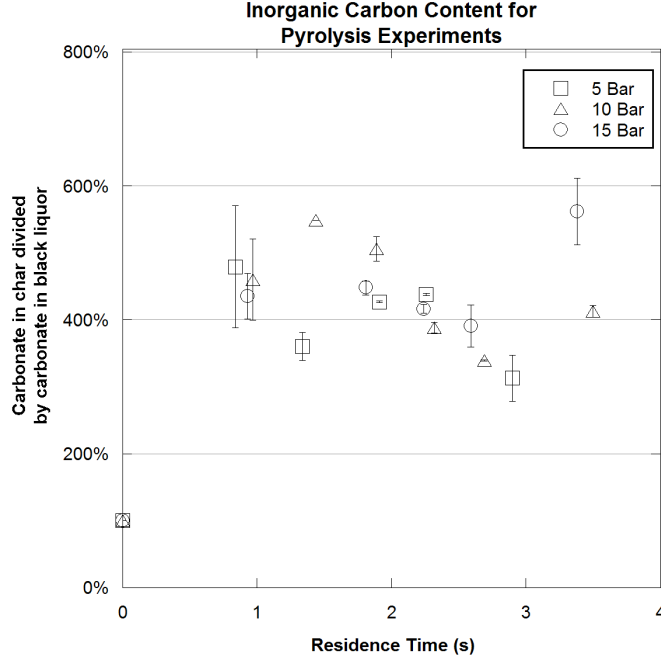
Figure 43: Carbonate content of pyrolysis char as percent of carbonate in black liquor. Char generated in PEFR at 900^oC, 100% N_2

experiments, with the error bars showing the highest and lowest value in each average. In Figure 43 the Y-axis is defined as the amount of carbonate remaining in the char divided by the amount of carbonate originally in the black liquor. The definition of the Y-axis is shown by equation 81,

$$Y = CY_j \times \frac{C_{i,j}}{C_{i,bl}} \tag{81}$$

where CY is the char yield of char j and C_i is the carbonate content of the sample, as determined by GCHS or coulometric techniques. This phenomenon has been observed in atmospheric black liquor gasification under similar heating rates, temperatures, and residence times [76]. The transient nature of the carbonate implies that both formation and destruction reactions occur. Various formation reactions involving the reduction of oxidized or partially oxidized sulfur species, or the reaction of reduced sulfur with CO_2, CO, or H_2O, have been proposed for the formation of carbonates [10, 47, 75] and are shown in equations 82 through 84.

$$Na_2S + 2CO_2 \longrightarrow Na_2CO_3 + COS \tag{82}$$

$$Na_2S + H_2O + CO_2 \longrightarrow Na_2CO_3 + H_2S \tag{83}$$

$$Na_2S_2O_3 + CO_2 \longrightarrow Na_2CO_3 + SO_2 + S \tag{84}$$
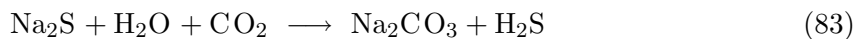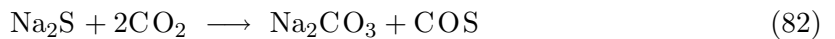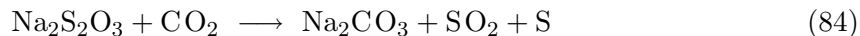
Based on the black liquor analysis provided by Weyerhauser (Table 5) the reactions of sulfide or thiosulfate illustrated above could account for no more than 50% of the carbonate formed during pyrolysis. Therefore, other reactions involving organically bound oxygen must also contribute to the formation of carbonate or carbonate-like compounds. For example, Wag et al. [81] suggested a mechanism for carbonate formation in black liquor char from alkali carboxylates present in the black liquor.

The destruction of carbonates can occur from reduction with solid carbon to form CO, CO_2, and $Na_{(v)}$, shown in equations 85 and 86 [27, 45].

$$2C + Na_2CO_3 \longrightarrow 2Na_{(v)} + 3CO \tag{85}$$

$$C + Na_2CO_3 \longrightarrow 2Na_{(v)} + CO + CO_2 \tag{86}$$
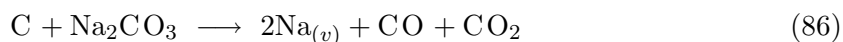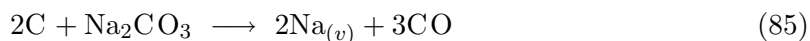
At thermodynamic equilibrium there is no carbonate present in the system, a fact that is reflected in the decreasing carbonate concentration as residence time increases in Figure 43. There are two points at long residence times that have high carbonate content. The sodium retention for these points were high as well, indicating that they are accurate data and not mistakes in the carbonate measurement. The exact reason for these points is unknown, but it could be due to condensation of Na_v on the surface of the char, resulting in an increase in carbonate at the surface. The presence of carbonate crystals on the char surface at high conversions can be seen in Figure 25.

Fixed carbon conversion is calculated as one minus the concentration of fixed carbon remaining in the char divided by the total carbon in the black liquor. This is shown by equation 87, which uses the same definitions as equation 81.

$$\% \ C_f \ Conv = 1 - CY_j \times \frac{C_{tot,j} - C_{i,j}}{C_{tot,bl}} \tag{87}$$

The use of total carbon in the black liquor for this conversion calculation is consistent with previously published literature. It reflects the fact that the high sodium content in black liquor results in ash carbon being present in forms other than sodium carbonate. A rigorous calculation of the theoretical inorganic carbon content in black liquor requires evaluation

of the thermodynamic equilibrium concentration of inorganic salts present. The sodium carbonate to sulfide ratio of these salts depends on the amount of water present, which varies across the range of experiments. In order to facilitate comparisons between reaction conditions the simplifying assumption of total carbon in the black liquor was used.

Percentage of C_f Conversion Due to CO_3 Formation for Pyrolysis Experiments
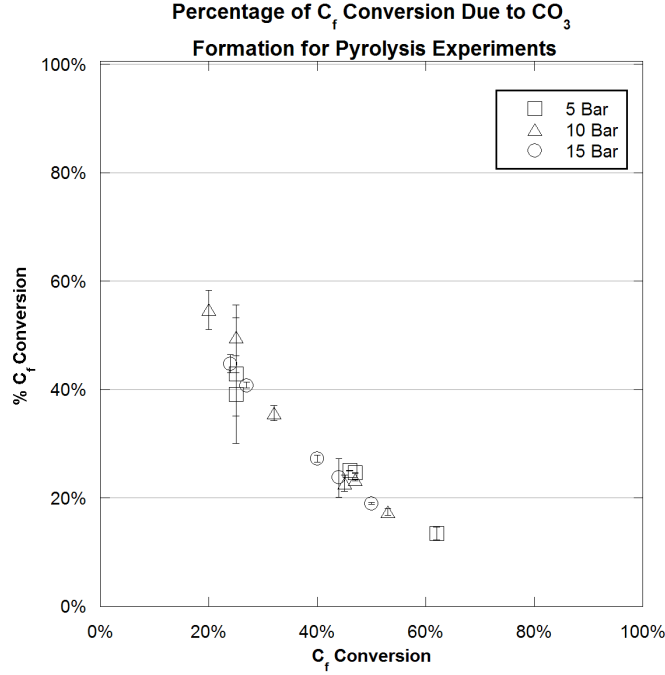
Figure 44: Percent of fixed carbon conversion due to carbonate for pyrolysis char. Generated in PEFR at 900°C, 100% N_2.

Figure 44 shows the percentage of fixed carbon conversion due to the presence of carbonate in the pyrolysis chars. This value is calculated by first rearranging equation 87 into equation 88,

$$\% \ C_f \ Conv = 1 - \left[CY_j \frac{C_{tot,j}}{C_{tot,bl}} - CY_j \frac{C_{i,j}}{C_{tot,bl}} \right] \tag{88}$$

which has the same definitions as equations 87 and 81. The first term in equation 88 is the definition of the fraction of total carbon remaining in the char, or $\%C_{tot}$. The percentage of conversion that is due to the loss of total carbon can be expressed by equation 89.

$$\% \ of \ C_f \ conversion \ due \ to \ total \ carbon \ loss = \frac{1 - \%C_{tot}}{\%C_f \ Conv} \tag{89}$$

The only other source of fixed carbon loss is to carbonate, so the percentage of fixed carbon conversion due to the presence of carbonate and the percentage of fixed carbon conversion

due to total carbon loss must sum to unity.

$$\% \ of \ C_f \ conversion \ due \ to \ total \ carbon \ loss + \% \ of \ C_f \ conversion \ due \ to \ carbonate = 1$$

$$(90)$$

Combining equations 89 and 90 gives equation 91,

$$\% \ of \ C_f \ conversion \ due \ to \ carbonate = 1 - \left[\frac{1 - \%C_{tot}}{\%C_f \ Conv} \right] \tag{91}$$

which is represented on the Y-axis of Figure 44.

At short residence times the fixed carbon conversion is low and the carbonate content is at a maximum (see Figure 43). These two facts combine so that at low fixed carbon conversions the formation of transient carbonates account for a significant portion of the initial fixed carbon conversion, shown in Figure 44. Immediately after entering the reactor some of the organic carbon that does not volatilize begins to transform into carbonate via equations 82 through 84, as well as others. After approximately two seconds of residence time, irrespective of pressure, the carbonate then begins to decompose via equations 85 and 86, shown in Figure 43. This reduction in carbonate content, coupled with the increasing total carbon loss due to reaction of fixed carbon with secondary CO_2, reduces the impact of this carbonate formation as conversion progresses. There seems to be a negligible effect of total pressure on this phenomenon at the conditions measured.

7.2   Carbon Conversion

Figure 45 shows fixed carbon conversion as a function of residence time for the pyrolysis experiments. As can be seen in the figure, increasing the pressure from 5 to 10 bars results in an approximately 40% decrease in conversion rate, as indicated by the slopes. The further increase of pressure from 10 to 15 bars results in a negligible decrese in the slope.

The fixed carbon conversion of pyrolysis char can be divided into three distinct regimes: devolatilization, carbonate formation/destruction, and pyrolysis gas reactions. The first regime, devolatilization, occurs immediately upon the char entering the reactor and heating. A percentage of carbon, in these experiments between 10% and 15% of the total carbon, is lost to low molecular weight carbon gases such as CO_2, CO, and CH_4, or tars. Based on

112

Carbon Conversion for Pyrolysis Experiments

$y = 7.78 + 18.7x$ $R^2 = 0.921$
$y = 13.2 + 11.9x$ $R^2 = 0.714$
$y = 14.5 + 11x$ $R^2 = 0.881$
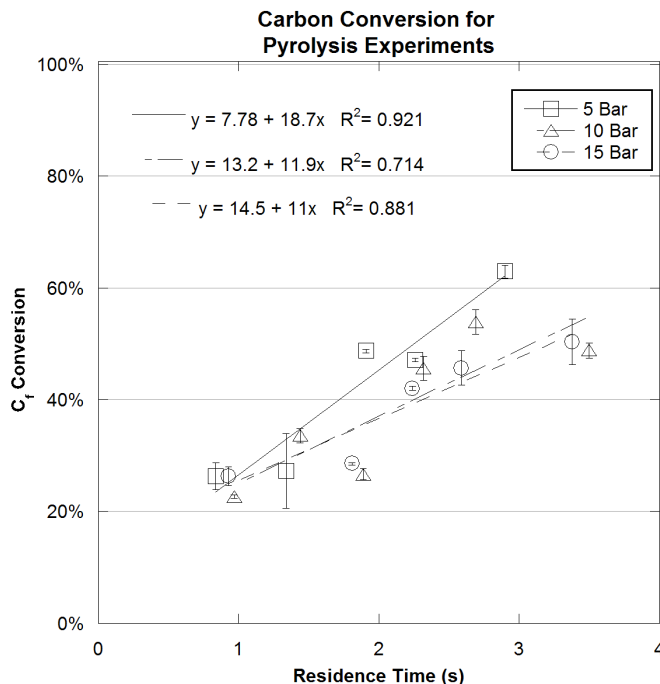
5 Bar
10 Bar
15 Bar

Figure 45: Fixed carbon conversion of pyrolysis char, generated in PEFR at 900^oC, 100% N_2

the inital pyrolysis char yields shown in Figure 42, increasing the pressure from 5 to 15 bars has little effect on this phase.

Near the same time devolatilization occurs, the second regime of carbon conversion commences, the formation and destruction of carbonates. These reactions occur via equations 82 to 86 and appear to be unaffected by the total pressure of the system. This invariance with total pressure is shown in Figure 43, which shows both the formation and destruction of the carbonate occurring at the same rate at all pressures indicated. At low fixed carbon conversions this carbonate formation mechanism accounts for a significant portion of the total fixed carbon loss, as illustrated in Figure 44. This destruction of carbonates continues through the range of residence times measured and is a source of CO_2 for reaction with fixed carbon.

The third regime of pyrolysis conversion involves the reaction between CO_2 and solid carbon. The CO_2 will be present from the initial devolatilization of the liquor, the reduction

of carbonate via equation 86, or the reduction of sulfate via reaction 92.

$$Na_2SO_4 + 2C \longrightarrow Na_2S + 2CO_2 \qquad (92)$$

$$Na_2SO_4 + 4C \longrightarrow Na_2S_2 + 4CO \qquad (93)$$
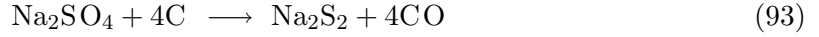
Other studies [35] show that at 900°C, 80% of the carbon lost to the gas phase during initial devolatilization is in the form of CO_2, which would provide a supply of reacting gas immediately after entering the reactor. As this CO_2 reacts with the fixed carbon and becomes depleted, the secondary source of CO_2 from the reduction of carbonates and sulfates in the char comes into play. Work done by Sricharoenchaikul [72] shows that at 900°C the all the sulfate in black liquor reduces in approximately 1.8 seconds, indicating that the kinetics are fast enough that sulfate reduction must be taken into account.

The scatter in the 10 bar data (as exhibited by the R^2 of the best fit line of 0.7) makes for somewhat uncertain interpretation of the data. A trend is seen where increasing pressure decreases the rate of pyrolysis carbon conversion. There is a 76% chance that the slopes between five and ten bar pressure are different, making the difference in the slopes statistically insignificant. The difference in slope between five and ten bar is likely due to the gas velocity differences in the experiments. This will be discussed more in the next chapter. There is no statistical significance to the difference in the slope between ten and fifteen bar. The calculations involving slope comparisons are outlined in Appendix D.

It is reasonable to assume that the surface area of pyrolysis chars behave similarly with respect to conversion as the gasification chars shown in Figure 39, which show large changes in surface area as a function of conversion. It can therefore be assumed that the rate of carbon conversion of pyrolysis chars is not a function of their surface area, as the rate is constant across a wide range of conversions. The most likely cause of decreased rate with increased pressure is the partial pressure of CO near the particle, through product-gas inhibition of the gasification rate. This is shown in equations 6 and 7 for CO_2 and H_2O gasification, respectively. However, there are two sources of CO: the devolatilization of black liquor and the product of the gasification reaction between C_f, CO_2, and H_2O (equations 4 and 5). Reference [31] shows that the gas phase for similar temperatures and pressures is at

water gas shift equilibrium. Therefore any H_2O generated during the initial devolatilization or pyrolysis prior to the first data point will probably have been reacted with fixed carbon prior to the first data point.

The primary method of pyrolysis carbon conversion at the residence times in Figure 45 is the reduction of carbonate and sulfate. These reduction reactions not only consume carbon from the matrix, but depending on the path (equation 86 or 93), it could generate secondary CO_2. There is direct experimental evidence of carbonate destruction at these residence times, as shown in Figure 43. The kinetics of sulfate reduction at atmospheric pressure, 900^oC, and similar heating rates is shown in [72], which shows sulfate reduction occurring between 0.7 and 1.8 seconds.

The currently accepted rate expressions for black liquor gasification by CO_2 and H_2O are given by equations 6 and 7, shown again here.

$$-r = \frac{K_1[CO_2]}{[CO_2] + K_2[CO]}$$

$$-r = \frac{K_3}{1 + \frac{K_4[H_2]}{[H_2O]} + K_5[CO]}$$

Regardless of what form it is in ($SO_4{}^{2-}$, $CO_3{}^{2-}$, $S_2O_3{}^{2-}$, or organically bound), the only source of oxygen is the black liquor. Devolatilization and pyrolysis reactions of the black liquor will put that oxygen into the gas phase primarily as CO_2, H_2O, and CO. Therefore, according to the above equations, both the reaction and inhibiting gases are from the particles. This is in contrast to the gasification experiments, which have an external source for the reaction gases.

Figure 46 shows the beginning of the reaction section of the PEFR in detail. The black liquor enters the reactor via the injector and immediately devolatilizes upon exposure to the radiant heat present in the reactor. This devolatilization creates a certain amount of CO_2 and CO near the particles, which is available for reaction with the fixed carbon.

The large difference between the ID and the OD of the injector causes a zone of separated flow to be present where the liquor devolatilizes. This separated flow zone will serve to draw CO_2 and CO away from the particles via the recirculating eddies formed in the zone,
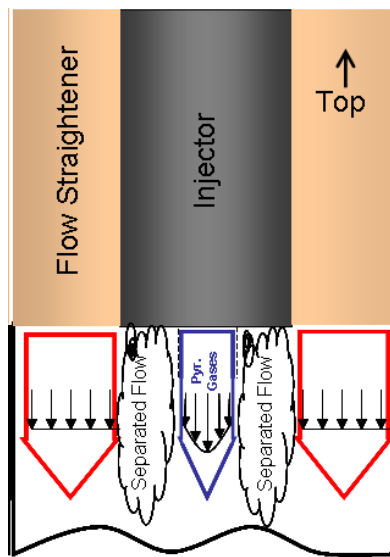
Figure 46: Detail of PEFR reaction zone entrance

decreasing their concentration. Direct evidence of this zone of separated flow can be seen in the physical characteristics of the char as discussed in Chapter V. At a fixed gas velocity and collector position, increasing the pressure had the effect of creating larger particles with a greater size distribution (Figures 27, 28, and 29) due to the increased zone of separated flow. Increasing pressure caused the zone of separation to be larger, increasing the tendency for the initially plastic char particles to collide. These collision then caused individual char particles to coalesce into larger particles, as shown in Table 25.

As the liquor travels down the reactor and away from the separated flow zone at the end of the injector, the radial component of flow decreases, as shown by Figure 30. Figure 43 showed that carbonate present in the black liquor reduced at a rate independent of pressure. It could be assumed from this observation that the reduction of sulfate would also reduce at a rate independent of pressure. With the reduction of carbonate and sulfate providing a major portion of the secondary CO_2 for the residence times investigated, this means that CO_2 was being provided at approximately the same rate at all pressures. Assuming that the rate of gasification is characterized by equations 6 and 7, the rate of conversion may then be dictated by the rate at which CO can be transported away from the particle. Diffusivity decreases as a function of $1/P$, so as the pressure increases the rate of CO diffusion away from the particle decreases and the overall carbon conversion rate decreases.

116

Due to the fact that both CO_2 and CO are being generated at the same location, experimental validation of this separated flow zone-diffusion theory for the local concentration of CO is difficult with pyrolysis experiments. Any attempt to change the zone of separated flow at the beginning of the reactor will change the concentration of both CO_2 and CO near the particle. However, in the gasification experiments a much greater source of reaction gases is available from the secondary gases. Since the underlying principle is consistent with both pyrolysis and gasification, this mechanism, along with experimental support, is further discussed in the next chapter.

CHAPTER VIII

CARBON CONVERSION DURING GASIFICATION

In addition to the previously mentioned reactions that occur during the pyrolysis (equations 82 to 86), the gasification of black liquor involves reactions due to the presence of external CO_2 and H_2O. While CO_2 is generated in the pyrolysis experiments due to devolatilization and destruction of carbonates, its formation is limited by the amount of oxygen present in the black liquor. In the gasification experiments excess CO_2 and H_2O (with respect to carbon in the black liquor) was added to the system so that all of the carbon in the black liquor will be reacted at equilibrium. The presence of CO_2 in the gasification gases has the additional effect of suppressing the destruction of carbonates via equation 86. Due to the oxygen limited situation present in the pyrolysis experiments very little water will be produced.

Two groups of gasification experiments were performed: one at a constant partial pressure of reacting gases and one at a constant mole fraction of gases. While the constant partial pressure experiments allow the elucidation of the true effect of pressure on black liquor gasification, industrial gasifiers do not have the ability to independently manipulate total and partial pressures. The main operational variable for high temperature oxygen (or air) blown gasifiers is the stoichiometric ratio (λ) of oxygen to black liquor carbon. Therefore the industry is more concerned with the effect of increased pressure at a constant mole fraction.

As previously discussed, the presence of water necessitated the presence of CO and H_2 for the constant mole fraction experiments only. The rate at which the water gas shift reaction (equation 66) approaches equilibrium is a function of the partial pressures of all gases involved. For the constant partial pressure experiments these were constant, but for the constant mole fraction experiments the partial pressures will increase with the total pressure. Therefore, for the constant mole fraction experiments CO and H_2 were added in

sufficient amounts so that the gas phase was at equilibrium with respect to water gas shift from the beginning. The partial pressure of water was limited by its saturation pressure due to condensation issues. Increasing the partial pressure of water beyond 0.25 bar will result in condensation along the liquid cooled collector, exhaust piping, cyclone, and mass flow controllers. The major problem with this is poor mass closures due to char loss along the piping. Additionally, a liquid phase present in the exhaust mass flow controllers prevents them from working properly, resulting in an inability to control the pressure of the reactor.

8.1 Char Yield

(a) Constant partial pressure. 0.25 bar H_2O, 0.5 bar CO_2.

(b) Constant mole fraction. 10%CO_2, 2%H_2O, 1.7%CO, 0.3%H_2
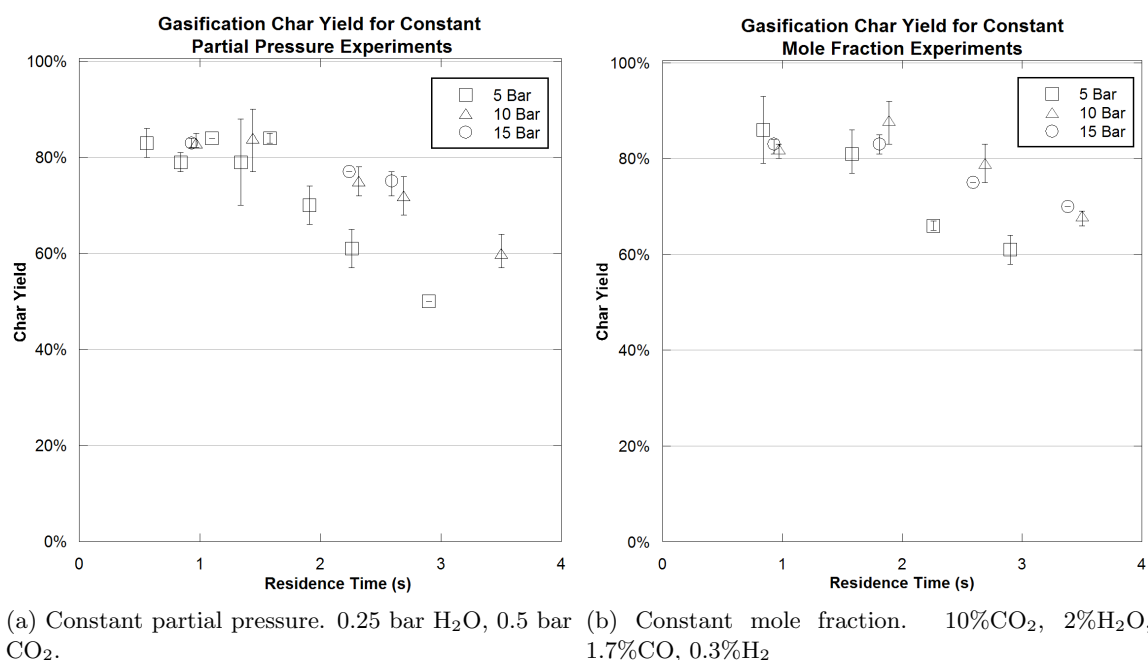
Figure 47: Gasification char yields, generated in PEFR at 900^oC.

Figure 47 shows the gasification char yields for both the constant partial pressure (a) and constant mole fraction (b) experiments. When compared with the yields shown in Figure 42, several observations can be made. First, the initial yield for both gasification conditions are approximately 80%, lower than the approximately 90% yield for the initial pyrolysis data points. The lower yield of the gasification experiments is likely due to the presence of CO_2 and H_2O causing a larger mass loss due to their reaction with the black liquor at residence times less than 0.6 seconds. That being said, the initial yield for the

gasification experiments appears to be independent of the partial pressure of the reacting gases, since the yields shown in Figure 47 were obtained under four different partial pressures of CO_2 and H_2O.

Second, the same phenomenon of constant char yield until approximately two seconds that was seen in the pyrolysis experiments is observed for the gasification experiments as well. This can again be attributed to carbonate formation from the reaction with sulfur species or organically bound oxygen, as described in the pyrolysis section. There will be no effect on the char yield by the exchange of oxygen from sulfates or thiosulfates to form carbonates. The total carbon loss steadily increases over the period of constant yield, meaning that gasification reactions are ongoing. The accepted Langmuir-Hinshelwood mechanism for gasification involves CO_2 chemisorbing onto an active catalyst site (equations 14 through 18). Therefore, the weight of the chemisorbed CO_2 must offset the weight of the carbon lost to gasification.

Past the two second point the yields begin to decrease due to the loss of carbon from gasification, unlike the pyrolysis chars which lost additional mass due to the reduction of carbonates. The addition of H_2O to the gas phase causes a higher equilibrium level of carbonate to be established in the system due to sulfur loss to the gas causing excess sodium in the char. This high carbonate equilibrium reduces the effect of the destruction reactions that were present during pyrolysis. For the gasification reactions, any yield loss due to the volatilization of sulfur occurs prior to the first data point. As the residence time increases no sulfur returns to the condensed phase. This is in contrast to the pyrolysis chars, which initially lose sulfur that is later recaptured. The fate of sulfur will be further discussed in Chapter 8.

Figure 48 shows the amount of carbonate present in the char as a percentage of initial carbonate. Note the higher levels of carbonate present in the gasification chars(500-800% of black liquor carbonate) than in the pyrolysis chars (300-550% of black liquor carbonate) shown in Figure 43. The same rapid formation of carbonate as was seen in the pyrolysis experiments is shown here. Once the gasification carbonate is formed it will remain un-reacted because of the high carbonate equilibrium present at these conditions, also shown

(a) Constant Partial Pressure. 0.25 bar H_2O, 0.5 bar CO_2.

(b) Constant Mole Fraction. 10% CO_2, 2% H_2O, 1.7% CO, 0.3% H_2
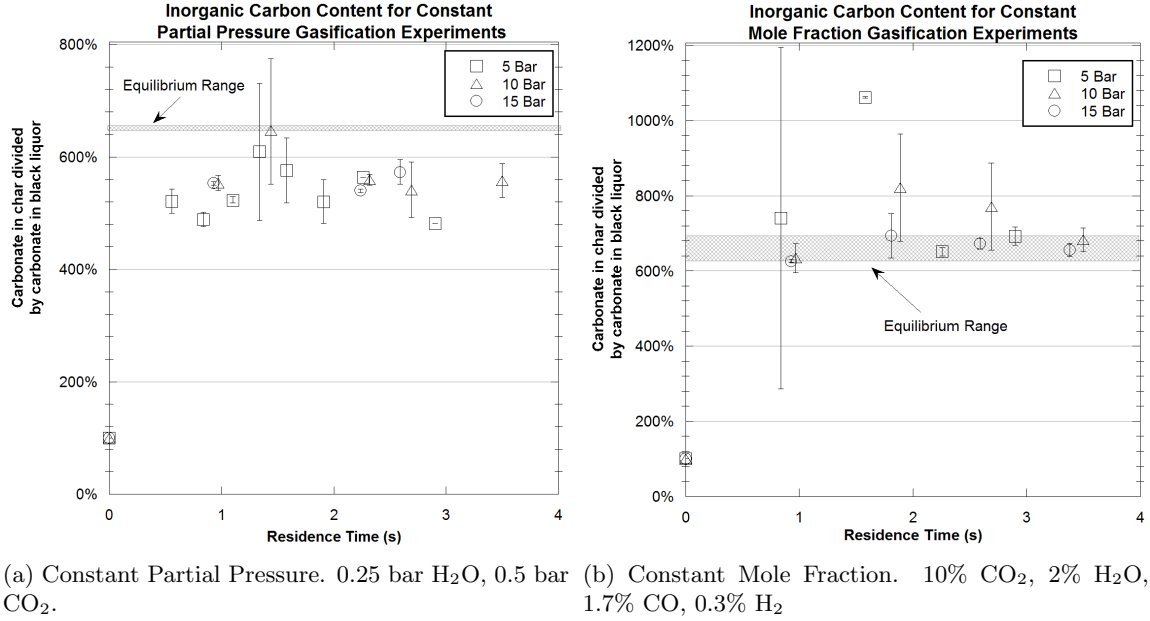
Figure 48: Carbonate content of gasification char as percent of carbonate in black liquor. Generated in PEFR at 900^oC

in in Figure 48. Subfigure (b) has a higher carbonate concentration than subfigure (a). This is due to both the higher partial pressure of CO_2 and the presence of CO. The higher CO_2 partial pressure will inhibit carbonate destruction via equation 86. The CO that was added to the gas phase in the constant mole fraction experiments will inhibit carbonate destruction equations 85 and 86. The variation of carbonate equilibrium values shown in subfigure (b) is due to the varying partial pressure of CO_2 and H_2O in the constant mole fraction experiments.

The presence of carbonate plays a significant role in the fixed carbon conversion of gasification char (see Figure 49), just as it does in the pyrolysis chars (shown in Figure 44). The lower slope in Figure 49 versus Figure 44 is due to the persistence of carbonate in the gasification system. Higher fixed carbon conversions have a decreased percentage of carbonate contribution because all the carbonate is formed prior to the first data point and does not contribute to the overall conversion in the residence times investigated.
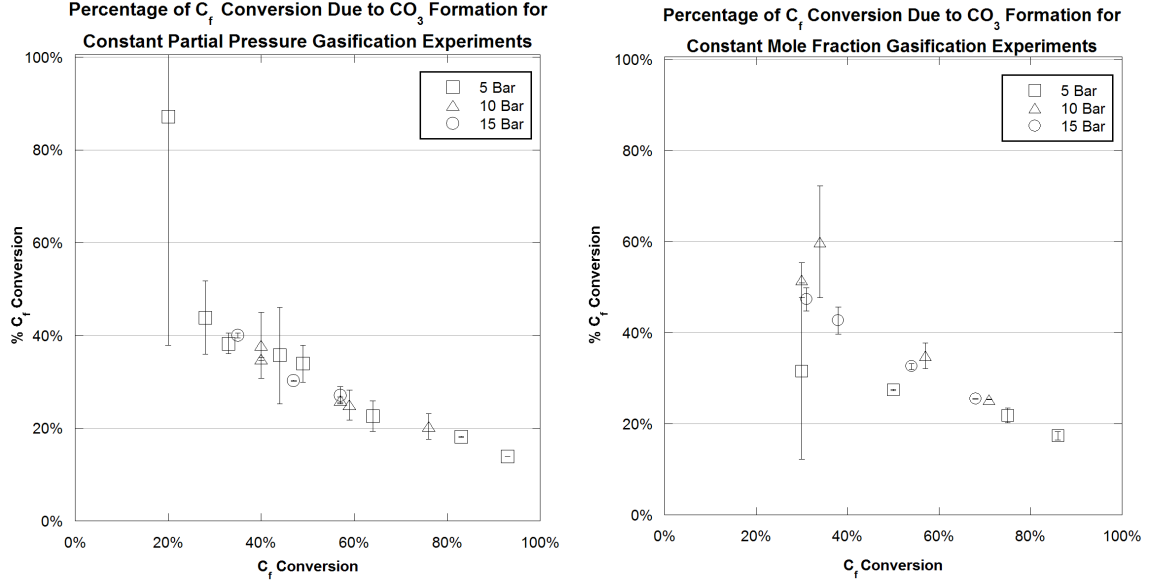
(a) Constant Partial Pressure. 0.25 bar H_2O, 0.5 bar CO_2.

(b) Constant Mole Fraction. 10% CO_2, 2% H_2O, 1.7% CO, 0.3% H_2

Figure 49: Percent of fixed carbon conversion due to carbonate for gasification chars generated in PEFR at 900^oC

8.2 Carbon Conversion

According to the commonly accepted mechanism for black liquor gasification, demonstrated by Li and van Heiningen [45] and Whitty et al [90], the kinetic expressions for CO_2 and H_2O gasification can be represented by equations 6 and 7, respectively, shown again here,

$$-r = \frac{K_1[CO_2]}{[CO_2] + K_2[CO]}$$

$$-r = \frac{K_3}{1 + \frac{K_4[H_2]}{[H_2O]} + K_5[CO]}$$

where $-r$ is the rate of carbon loss due to gasification and K_1 through K_5 are constants. These equations state that increasing the presence of CO_2 or H_2O will increase the rate of carbon gasification, while the presence of CO and H_2 will inhibit the rate of carbon gasification.

Figure 50 shows fixed carbon conversion data for the constant partial pressure gasification experiments, conducted under 0.25 bar H_2O, 0.5 bar CO_2, with the balance of nitrogen.
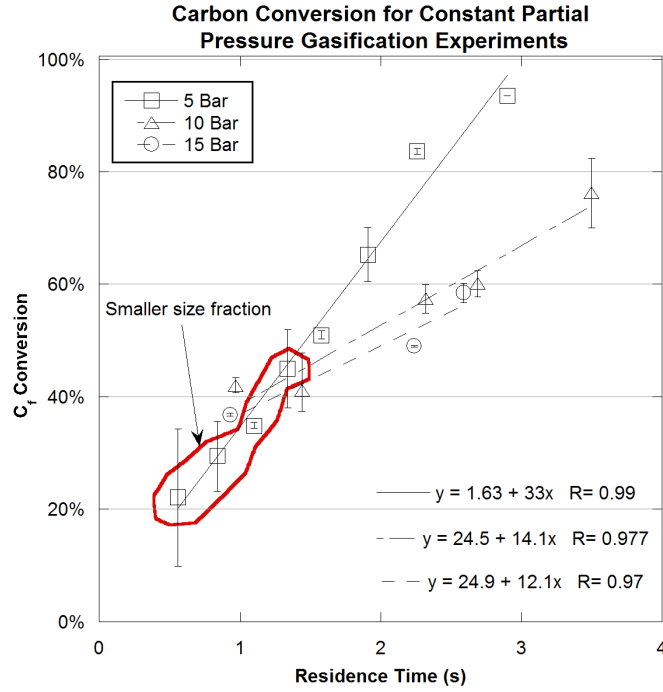
Figure 50: Fixed carbon conversion for constant partial pressure gasification char. Generated in PEFR at 900^oC, 0.25 bar H_2O, 0.5 bar CO_2, balance N_2.

Linear best fit lines and their associated equations are also shown in the figure. The rates of fixed carbon conversion at each pressure, with units of percent fixed carbon per second, are shown by the slopes of these lines. It should be noted that the five bar experiments (gasification as well as pyrolysis) had a "superficial" velocity ($V_{gas}/A_{reactor}$) of 30 cm/s, while the 10 and 15 bar experiments were conducted at a 20 cm/s superficial velocity. This difference in velocity was accounted for when calculating the residence times in Fluent, as explained in Chapter 4.

The first thing to notice about Figure 50 is that at each pressure, the fixed carbon conversion is highly linear with respect to time, as evidenced by the high R^2 (all > 0.96) values of the best fit lines. Interestingly, across these same conversions the surface area of the gasification char varied from approximately 4 m^2/g to 115 m^2/g, shown in Figure 39. If the rate of carbon conversion was proportional to the surface area of the particles, then the rates would follow the surface area curves in Figure 39. The rate would start out relatively constant until 40% conversion, reach a maximum at near 60% conversion, and then decrease as conversion approaches 100%. Since the rates are linear across the entire

range investigated it can be concluded that rate is not proportional to surface area at these conditons.

Secondly, the first four points of the 5 bar gasification data (circled) were generated using the smaller size particle of 38-53 μm diameter. The main size fraction used in these experiments was a 75-90 μm size fraction, and the estimated size difference between these two fractions is shown in Figure 31. The fact that both size fractions give conversions on exactly the same line give experimental support that there are not any significant internal concentration gradients at these small particle diameters. Numerical analysis using the Weisz modulus also support this observation. Critical particle diameters using the Weisz modulus will be discussed later in this chapter.

Figure 50 does show a decrease in gasification rate with increasing total pressure. Increasing the pressure from 5 to 10 bars shows a 57% decrease in the gasification rate. Further increasing the pressure from 10 to 15 bars decreases the rate by a much smaller 15%. The same trend of a large decrease in conversion between 5 and 10 bars and a smaller decrease between 10 and 15 bars was observed in the pyrolysis runs as well (see Figure 45). The reason for this decrease in rate is due to the local concentration of inhibiting gases of H_2 and CO near the particle. This mechanism, along with experimental validation, will be discussed in the next section.

Figure 51 shows fixed carbon conversion data for the constant mole fraction experiments, conducted at 10.0% CO_2, 2.0% H_2O, 1.7% CO, and 0.3%H_2. The same linear relationship between fixed carbon conversion and residence time is seen, with R^2 for the best fit lines greater than 0.96 in all cases. This again suggests that the rate of carbon conversion is not a function of surface area at these conditions. The same general trend with respect to pressure and carbon conversion is observed in Figure 51 as in Figures 45 and 50: a large decrease in rate between 5 and 10 bars, with a smaller decrease in rate between 10 and 15 bars. As in Figures 45 and 50, Figure 51 has a higher superficial velocity for the five bar experiments (30cm/s) than the ten and fifteen bar experiments (20cm/s).

Figure 52 shows recent work published by Harris [31] in which different types of coal chars were gasified in a PEFR very similar to the one used for this thesis. Note the similarity

124
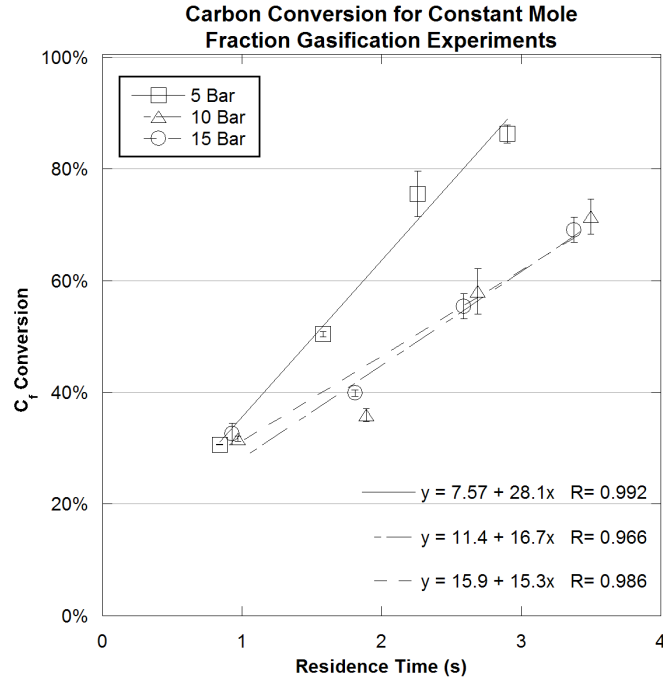
Figure 51: Fixed carbon conversion for constant mole fraction gasification char. Generated in PEFR at 900°C, 10%CO_2, 2%H_2O, 1.7%CO, 0.3%H_2, balance N_2.
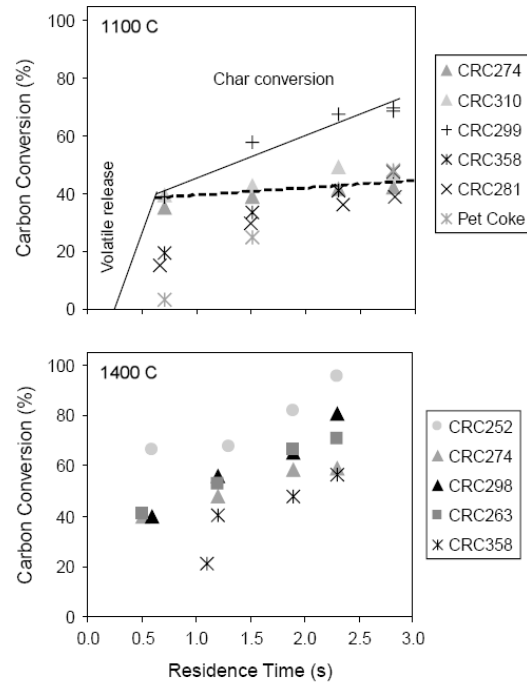
Figure 52: Carbon conversion of coal char for various types. 20 bar, PEFR, O_2 balance N_2, O:C ratio 1:1

Source: [31]

between the conversion curves of Figures 50, 51, and 52. All three plots show an initial sizable conversion due to devolatilization effects, followed by a slower constant slope due to the gasification reaction. The rates of coal gasification at 1400^oC and the conditions investigated are similar to those of black liquor gasification at 900^oC in this study. While it is acknowledged that the reaction conditions are somewhat different, the sodium catalyzed nature of black liquor gasification is largely responsible for the ability of black liquor to be gasified at the same rate at a much lower temperature.

8.3   Conversion Rate Limiting Step

The similarity of Figures 45, 50, and 51 suggest a common rate limiting step. Increasing the pressure does result in a decrease in the surface area of the resultant chars, but this difference is quickly eliminated once fixed carbon conversion nears 40% (Figure 39). The linear rate vs. time curves shown in 45, 50, and 51 clearly show that the rate of carbon conversion is not a function of surface area, as previously discussed.

The constant partial pressure experiments shown in equation 50 are particularly useful in eliciting a mechanism, as the gas concentrations of CO_2 and H_2O shown in equations 6 and 7 are constant at all pressures. The conditions for the experiments were chosen so that a sufficient excess of oxidizing gases (at least a 15:1 molar ratio of CO_2 and H_2O to black liquor carbon) would be present at all pressure (shown in Table 21), so the concentration of CO_2 and H_2O can be assumed to be constant in all cases as well.

Equations 6 and 7 suggest another source for the difference in rates: the local concentration of CO and H_2 near the particle. CO and H_2 will be generated by two primary sources: initial devolatilization of the black liquor and the gasification reactions between CO_2 and H_2O and the fixed carbon in the black liquor. The fact that there are two sources of inhibiting gases, coupled with the geometry of the reactor, allows for experimental investigation.

The devolatilization of black liquor begins at approximately 200^oC, which is 700^oC below the experimental temperature. The radiant heat flux from the walls of the reactor, coupled with the preheated secondary gases, heat the black liquor particles to the reaction temperature within the first several millimeters of the reactor. It can therefore be assumed that

126

black liquor devolatilization and the evolution of inhibiting gases associated with it will occur in this region as well. The large difference between the inner and outer diameter of the injector (Figure 46) creates a zone of separated flow near the tip of the injector (Figure 30). In addition to having physical effects on the char structure (Figure 27 and Table 25), this zone of separated flow will serve to remove the inhibiting devolatilization gases that are generated in the same region.

The second source of inhibiting gases is the formation of product gases from the gasification reaction themselves. At the isothermal experimental conditions the diffusivity of these inhibiting product gases will be a function of 1/P.

Since the slopes (therefore the carbon conversion rates) of the 10 and 15 bar experiments are very similar to each other it can be assumed that there is a more complex explanation to the concentration of inhibiting gases near the particles than diffusion rates alone. Inhibiting gas concentrations near the particles will also be a function of the zone of separation that is formed at the tip of the injector.

If the presence of CO and H_2 limit the rate of reaction, the rate of reaction at isothermal, constant partial pressure conditions will be a function of the gas phase Reynolds number and the diffusivity of the gases. Algebraically this can be expressed by equation 94

$$-r = K(Re)^a(D_{ab})^b \tag{94}$$

where Re is the gas phase Reynolds number, D_{ab} is the diffusivity of the inhibiting gases, and K, a, and b are unknown constants.

While it is impossible to change the fact that diffusivities scale with 1/P, it is possible to change the size of the separated flow zone, and therefore the amount of CO and H_2 removed from near the particles at the beginning of the reactor. At a fixed geometry the separated flow zone that is generated at the entrance of the reactor is a function of Reynolds number of the gas, shown in equation 73. Increasing density (via pressure) or increasing velocity (via mass flow) will change this value. Therefore an additional set of experiments were performed at 5 bar total pressure and 0.25 bar H_2O, 0.5 bar CO_2 in which the mass flow of gases was reduced to 2/3 of the original 5 bar experiments. While the mass flow of gases

were decreased, there was still a 15:1 ratio of oxidizing gases to fixed carbon in the black liquor, so the concentration of gases can still be assumed to be constant throughout the length of the reactor.

Using the slopes of the best fit lines from the constant partial pressure data (shown in Figure 50), it was possible determine the values of the unknown constants in equation 94. The values for these constants are shown in Table 27. Once the values of the unknowns were determined it was possible to predict the rate of carbon gasification of the lower flow rate 5 bar experiment. As can be seen in the table, the model predicts the slope of the 5 bar lower flow rate experiment very well.

Table 27: Constants for gasification empirical equation $-r = K(Re)^a (D_{ab})^b$

Experimental Conditions	Re #	D_{ab} cm^2/s	Act. Slope g/g-s	Calc. Slope g/g-s	% Error
5 bar 30cm/s	790.5	0.4	0.330	0.330	
10 bar	1054	0.2	0.141	0.141	
15 bar	1581	0.13	0.121	0.121	
5 bar 20cm/s	527	0.4	0.186	0.185	0.58%

$$K = 1.31 \times 10^{-4} \text{ g-sec}^{b-1}/\text{cm}^{2b}$$
$$a = 1.42$$
$$b = 1.81$$

Figure 53 compares the slopes of the two constant partial pressure five bar gasification experiments. The data from both experiments are very linear, with R^2 of the best fit lines 0.99 and 0.97 for the 30 cm/s and 20 cm/s gas velocities, respectively. Decreasing the velocity by a factor of 2/3 had the effect of decreasing the rate of gasification by 44%. There was at least a 15:1 excess of H_2O and CO_2 to black liquor carbon for the experiments, so this was not a factor in the rate difference. Both experiments had the same partial pressures of CO_2 and H_2O, making their concentrations in equations 6 and 7 the same. Since both experiments were conducted at the same pressure and temperature, the diffusivity of the product gases from the gasification reaction will be the same for both conditions. Decreasing the velocity of the gas will, however, result in a smaller zone of separated flow at the entrance of the reactor. This smaller zone of separated flow will draw away less of the CO and H_2 that were generated from the initial devolatilization of the black liquor from near the particles

Carbon Conversion for 5 Bar Constant Partial Pressure Experiments

Legend: 5 Bar 30 cm/s, 5 Bar 20 cm/s

y = 21.3 + 18.6x   R= 0.971

y = 1.63 + 33x   R= 0.99
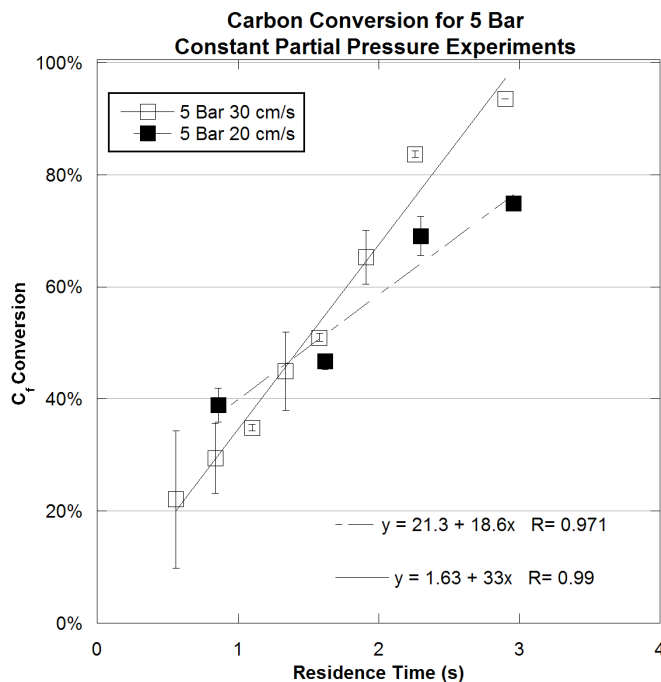
Figure 53: Fixed carbon conversion comparison for 5 bar constant partial pressure gasification at two Reynolds numbers. Generated in PEFR at 900^oC, 5 bar total pressure, 0.25 bar H_2O, 0.5 bar CO_2, balance N_2.

at the entrance of the reactor. This higher concentration of CO and H_2 will result in a lower rate of carbon gasification in the experiment, vis á vis equations 6 and 7. Therefore, at these conditions the rate of inhibiting gas removal from near the particle will dictate the rate of gasification.

Figure 54 is a plot combining the lower flow rate 5 bar gasification experiments with the 10 and 15 bar gasification experiments, so that the superficial velocity at all pressures is equal. The slope of the five bar gasification data is much closer to the ten and fifteen bar data than in Figure 50. This significant decrease is due to the smaller zone of separated flow at the beginning of the reactor removing less of the inhibiting CO and H_2 that was generated during the initial devolatilization of the liquor. Increasing the pressure still decreases the overall gasification rate, however, shown by decreasing slopes with increasing pressure. Statistical analysis of the data in Figure 54 reveals that the differences in slopes are not significant, with only a 75% chance that the slopes between the five and ten bar data in Figure 54 are different. The procedure for this analysis is shown in Appendix D.

Carbon Conversion for Constant Partial Pressure Gasification Experiments

Legend:
- 5 Bar 20cm/s
- 10 Bar
- 15 Bar

$y = 21.3 + 18.6x$ R= 0.971
$y = 24.5 + 14.1x$ R= 0.977
$y = 24.9 + 12.1x$ R= 0.97

Y-axis: C_f Conversion
X-axis: Residence Time (s)
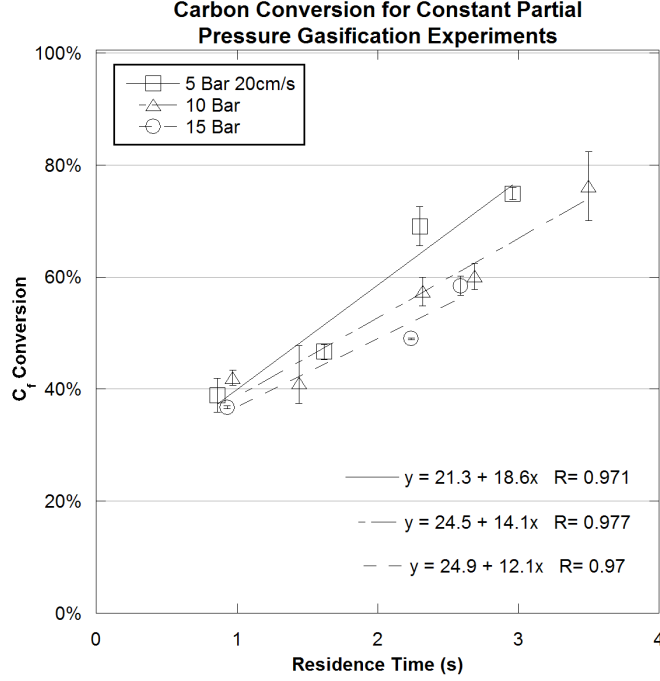
Figure 54: Fixed carbon conversion for constant partial pressure gasification char at fixed gas velocity. Generated in PEFR at 900^oC, 0.25 bar H_2O, 0.5 bar CO_2, balance N_2.

This empirical equation shown in equation 94 explains the effect of only pressure on the rate of gasification, and under the geometry constraints of the PEFR. The effect of reactant gas concentration is not included, as evidenced by the lack of concentration terms. Changing the geometry of the entrance will effect gas flows and consequently the values of the constants in equation 94.

The rate of diffusion, D_{AB}, is characterized by the Chapman-Enskog equation [8]

$$D_{AB} = \frac{KT^{3/2}}{P\sigma_{AB}^2\Omega_D}\sqrt{\frac{1}{M_A} + \frac{1}{M_B}} \tag{95}$$

where K is a constant, T is temperature, σ_{AB} is the collision diameter, Ω_D is the collision integral, and M is molecular weight. Substituting $\rho = \text{P/RT}$ in equation 73 results in

$$Re = \frac{vPL}{RT\mu} \tag{96}$$

where v is velocity, P is pressure, L is a characteristic length, R is the ideal gas constant, T is temperature, and μ is viscosity. Combining equations 95 and 96 into equation 94 at constant temperature, gas concentrations, and geometry results in equation 97

$$-r = Kv^aP^{a-b} \tag{97}$$

130

where r is the fixed carbon gasification rate, K, a, and b are constants, v is gas velocity, and P is pressure. Substituting the values for a and b from Table 27 gives equation 98,

$$-r = K\frac{v^{1.42}}{P^{0.39}} \tag{98}$$

which has the same definitions as equation 97. Equation 98 indicates that at a given pressure increasing the gas velocity will increase the rate of gasification, and at a fixed gas velocity increasing the pressure will decrease the rate of gasification. These two observations are consistent with what has been seen in other studies and in industry.

8.4 Critical Diameters

With the information that has been collected regarding gasification rates and char characteristics, it is possible to calculate estimates of critical diameters for char particles. The critical diameters are the diameters at which the Weisz Modulus (equation 50), shown again below, has values less than 0.15, meaning that there are negligible internal concentration gradients of reacting gases in the particle.

$$M_w = \frac{r\rho_{c_f}L^2}{M_c C_{gas} D_{eff}}$$

The effective diffusivities used in the critical diameter calculations use the average pore diameter of the constant partial pressure gasification chars to account for pore diffusion resistance. The average pore diameters for these chars were calculated by equation 80, and are shown in Figure 41.

The mean free path of a gas molecule can be calculated by equation 99 [43]

$$\lambda = \frac{RT}{\sqrt{2}\pi d^2 P N_o} \tag{99}$$

where λ is the mean free path of a gas molecule, R is the ideal gas constant, T is temperature, d is the molecular diameter of the molecule, P is pressure, and N_o is Avogadro's number. Comparing the average pore radius to the mean free path of the gas molecules gives an indication as to the relative importance of Knudsen verses Fickian diffusion. This ratio is shown in Figure 55 for CO_2 and H_2O molecules.
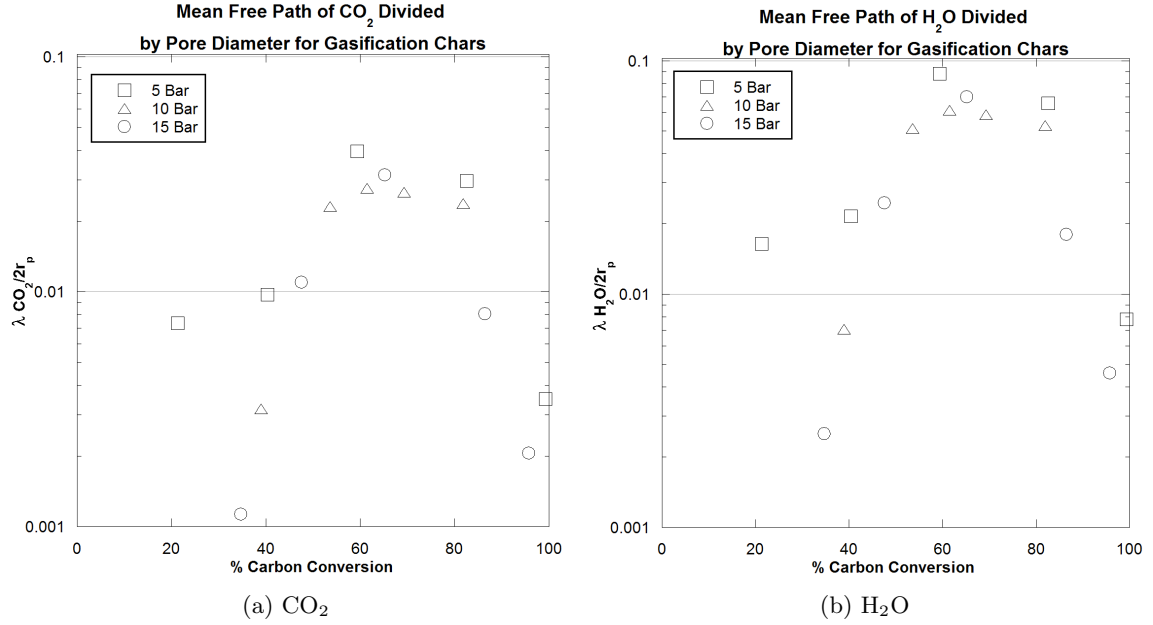
Figure 55: Ratio of mean free path to pore diameter for chars in constant partial pressure gasification experiments. Generated in PEFR at 900^oC, 0.25 bar H_2O, 0.5 bar CO_2, balance N_2.

The higher values for $\lambda/2r_p$ for H_2O reflect the smaller diameter of the water molecule and therefore a longer path length. In no instance, however, does the path length approach more than 10% of the average pore diameter, so the importance of Knudsen diffusion is very limited in the overall calculation for effective diffusion. The effective diffusivities in the particles were calculated using equation 43 with the worst case assumption of a tortuosity of 7.

Table 28: Critical diameters for constant partial pressure gasification chars

Pressure Bar	Porosity %	Minimum Pore Radius μm	Minimum Critical Diameter mm
5	97.8	0.59	0.91
10	96.6	0.43	0.74
15	93.9	0.25	0.59

Using the modified Weisz Modulus shown in equation 50, the critical diameters for 5, 10, and 15 bar gasification char are shown in Table 28. The critical diameter is the diameter at which internal diffusion resistance is negligible to the overall resistance to reaction. A particle smaller than the critical diameter will have constant reacting gas concentrations

along its radius, while a particle larger than the critical diameter will have decreasing reactant gas concentration toward the center of the particle. Since the average pore diameter is a function of the surface area of the char (see equation 80), only the minimum pore radii and critical diameters for each pressure are shown in Table 28.

Other assumptions that were made in the calculations of the critical diameters shown in Table 28 include:

- Constant char porosity which is equal to the short residence time pyrolysis char porosity determined at the given pressure

- Constant char bulk density which is equal to the short residence time pyrolysis char density determined the given pressure

- Constant diffusion coefficients along the entire radius of a char particle

- Reaction conditions and rates equal to those of Figure 50.

CHAPTER IX

SULFUR PHASE DISTRIBUTION

In addition to producing a high quality syngas, a gasifier in a pulp mill will have the additional constraint of producing a green liquor suitable for recovery of the pulping chemicals. Of particular importance to this is the ultimate phase distribution of sulfur in the gasifier. In combustion the stoichiometric amount of oxygen allows the sulfur to remain oxidized as Na_2SO_4 until its eventual reduction in the smelt bed prior to leaving the boiler. In gasification, however, sulfur is split between the gas and condensed phases. There are advantages and disadvantages to this split of sulfur between the phases.

The kraft pulping process derives its name from the german word for "strong". One of the main reasons that the kraft process produces a stronger fiber is the presence of Na_2S in the pulping liquor. Na_2S is known to selectively attack and degrade lignin molecules over cellulose to a much greater extent than NaOH. The presence of sulfur in the gas phase in gasification allows for its separate recovery. This sulfur can then be used to produce liquors with different sulfidities or polysulfide liquor in order to take full advantage of sulfur's selective pulping properties. Several alternative pulping processes have been developed that require separation of sulfur and sodium, such as polysulfide anthraquinone (PSAQ), mini-sulfide sulfite anthraquinone (MSSAQ), and alkaline sulfite anthraquinone (ASAQ) [14, 34, 49, 50].

The disadvantage of the sulfur split between phases is the generation of additional carbonate in the process. While the sulfur is split between the phases, sodium remains completely in the condensed phase. Therefore, for every mole of sulfur that enters the gas phase there are two moles of sodium that are left behind. Extra carbonate must be formed to make up for the loss of sulfur to the gas phase, so that the remaining sodium has an anion associated with it. Overall, for every mole of sulfur that leaves the condensed phase an extra mole of carbonate is formed to replace it. The extra formation of carbonate means that

134

much more energy must be spent in the recausticization process, which uses heat to drive off CO_2 from calcium carbonate. The remaining lime, or CaO, is used to convert sodium carbonate to sodium hydroxide via reaction 2. This extra energy is very cost prohibitive and significant work is being done to ameliorate the additional causticizing load associated with the phase split of sulfur. Most of this work revolves around the use of titanates, borates, or manganates which bind sodium in the gasifier and prevent the formation of carbonates [59, 60, 61, 96].

While increasing energy efficiency, pressurization of the gasifier may also result in more sulfur converted to the gas phase. The primary equilibrium of interest in the production of gas phase sulfur is shown in equation 8 [48], shown again here,

$$Na_2S + CO_2 + H_2O \longleftrightarrow Na_2CO_3 + H_2S$$
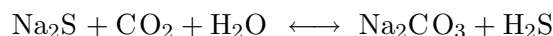
where two moles of gas are in equilibrium with one mole of hydrogen sulfide and sodium carbonate. With two mole of gas on the reactant side and only one on the product side, increasing the pressure will result in the equilibrium shifting to the right via Le Châtelier's principle.

9.1 Sulfur Distribution During Pyrolysis

Figure 56 shows the sulfur in the chars generated in the pyrolysis experiments. At t=0, 100% of the sulfur will be in the liquor. For all pressures, the minimum amount of sulfur retained occurs at the shortest residence time, indicating that upon initial devolatilization and pyrolysis a significant portion of the sulfur is vaporized. The equilibrium level of sulfur in the char is 100%, as shown in Figure 56. The sulfur in the char asymptopically approaches this equilibrium at all pressures with increasing residence time. The five bar char reaches equilibrium first, somewhere between 1.0 and 1.2 seconds. The ten bar char reaches its equilibrium level of sulfur around 2.5 seconds, and the fifteen bar char reaches its equilibrium near 3.5 seconds.

This increased time for the sulfur to return to the condensed phase with increased pressure indicates a diffusion-type process is involved, since increasing pressure decreases diffusion rates. These observations are entirely consistent with previously published results

135
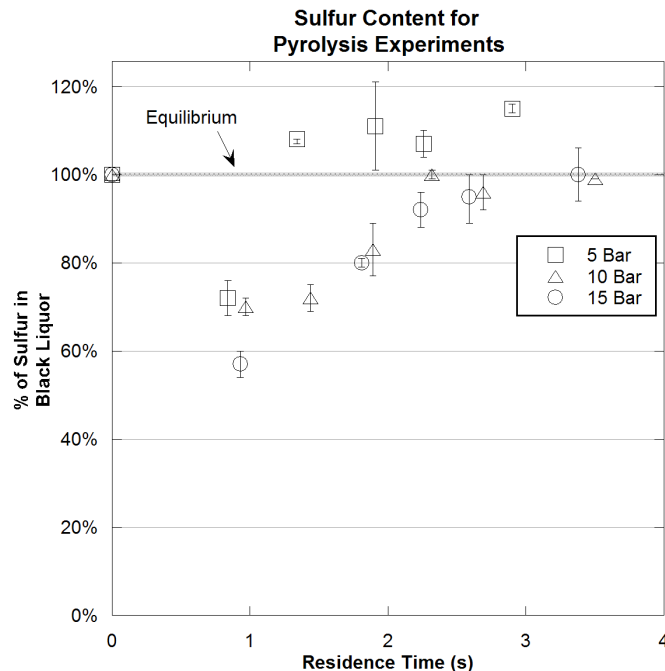
Figure 56: Sulfur phase distribution for pyrolysis char

by Sricharoenchaikul et al. [72], in which time dependent data was obtained for sulfur

species evolved during pyrolysis of kraft black liquor in both the gas and condensed phases.

The authors concluded that large amounts of organic sulfur gases were generated during

the initial devolatilization of liquor by both the vaporization of organically bound sulfur

and the insertion of elemental sulfur (produced by the decomposition of $Na_2S_2O_3$ to S via

equations 23, 24, or84) into hydrocarbon fragments.

The elemental sulfur could then react with the sodium catalyst sites present in the black

liquor char to form Na_2S. Another mechanism for Na_2S formation could be the gas phase

reaction between elemental sulfur and volatilized sodium. While the sulfur is converted to

gaseous species very rapidly, sodium volatilizes more slowly. This is shown in Figure 57,

which clearly shows a decrease in the sodium content of the pyrolysis chars at all pressures.

A minimum is reached between 2 and 3 seconds for the 10 and 15 bar chars, after which

sodium returns to the condensed phase. Given the fact that sulfur has been shown to return

to the condensed phase under conditions in which sodium volatilization is minimal the gas

phase reaction is thought to be of secondary importance.
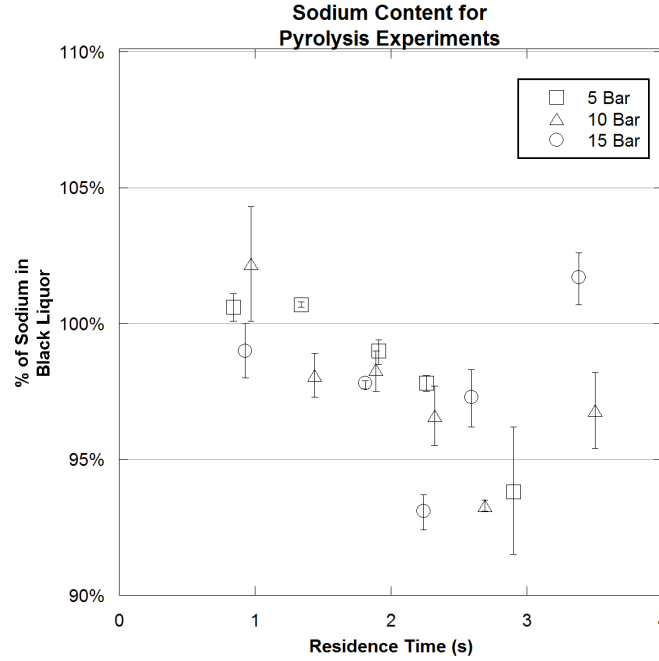
Figure 57: Sodium phase distribution for pyrolysis char, generated in PEFR at 900°C.

9.2 Sulfur Distribution During Gasification
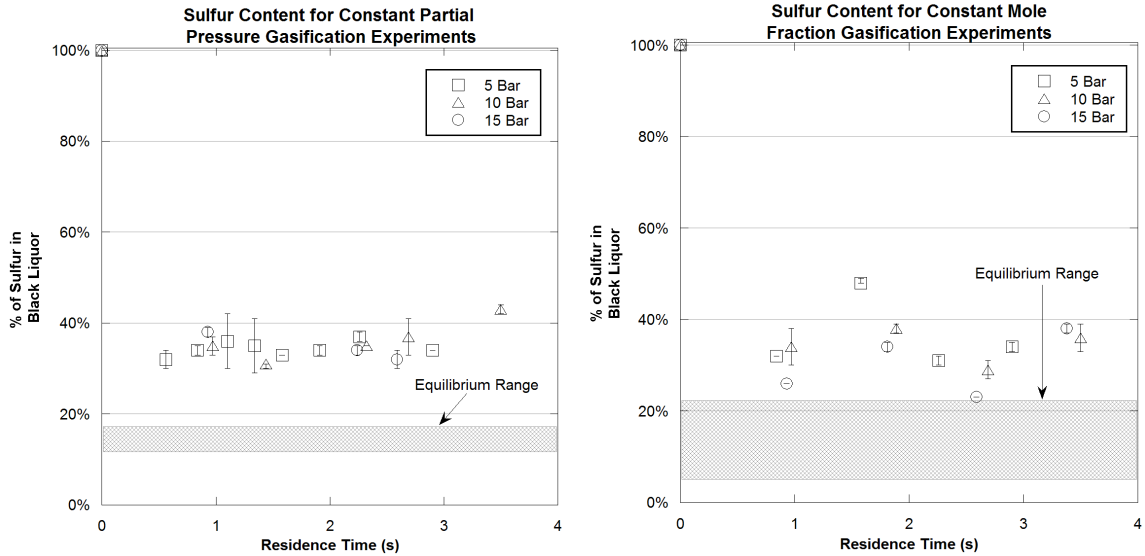
(a) Constant partial pressure. 0.25 bar H$_2$O, 0.5 bar CO$_2$, balance N$_2$

(b) Constant mole fraction. 10%CO$_2$, 2% H$_2$O, 1.7% CO, 0.3 % H$_2$, balance N$_2$

Figure 58: Sulfur phase distribution for gasification chars, generated in PEFR at 900°C.

The sulfur phase distributions for the gasification experiments are shown in Figure 58. Subfigure (a) refers to the constant partial pressure experiments, while subfigure (b) refers

137

to the constant mole fraction experiments. The equilibrium fraction of sulfur remaining in the condensed phase are included in each figure as well. The wider sulfur equilibrium found in the constant mole fraction experiments (subfigure (b)) is due to the range of H_2O partial pressure associated with those experiments. The constant partial pressure experiments had a much smaller condensed phase sulfur equilibrium since the partial pressure of water was invariant with total pressure. The broader sulfur equilibrium in the constant mole fraction experiments seems to be reflected in the broader range of sulfur remaining in the char. A very definite equilibrium seems to be established with the constant partial pressure experiments, while a broader distribution of sulfur is shown in the constant mole fraction experiments.

For analysis of the mechanism in Figure 58 it is useful to observe the behavior shown in Figure 56. The pyrolysis char showed a significant loss of sulfur to the gas phase during the devolatilization of black liquor, which was consistent with previous research [72]. Since the liquors devolatilize similarly whether in the presence of reacting gases or not, what appears to be happening is that the gas phase organic sulfur compounds that were created during devolatilization are reacting with the gas phase. The products of these reactions are thermodynamically stable, probably H_2S or COS. The sulfur associated with these gases does not return to the condensed phase in these experiments, shown by the constant level of sulfur in the char at increasing residence times in Figure 58.

The equilibrium that seems to be established is greater than what was predicted by the thermodynamic modeling. There are two possible explanations for this. The most probable explanation is that the assumption of ideality of the molten phase solution of K_2S, K_2CO_3, Na_2S, and Na_2CO_3 is incorrect. This system is not very well understood at this time, and small changes in the activities of components in the solution can have large effects on the ultimate destination of sulfur. Work is ongoing in Sweden to better characterize this system. A second possibility is that the kinetics of the reaction between Na_2S, CO_2, and H_2O (shown in equation 8) are sufficiently slow as to not significantly effect the sulfur distribution at these residence times.

CHAPTER X

SUMMARY AND RECOMMENDATIONS

10.1   Char Physical Characteristics

A series of experiments were conducted in which pyrolysis chars were created at 5, 10 and 15 bars of pressure and at approximately one second residence time. These chars were then analyzed for their physical characteristics using a suite of analytical techniques, including surface area analysis, porosimetry, size distribution, and microscopy.

1. **Effects of pressure on char physical characteristics occur primarily at short residence times.**

   It was found that the effect of pressure on the physical characteristics of black liquor char manifest themselves primarily at short residence times. The reason for this is two-fold. First, it is well documented that black liquor swells upon devolatilization [18, 21, 23, 24, 33]. This swelling is due to the generation of gases from the volatile portions of black liquor. These gases have a very large specific volume and their rapid evolution causes the swelling of the black liquor particle. Second, black liquor char is plastic in nature when it is generated under pressurized, high heating rate conditions. This correlation between pressure, heating rate, and plasticity has been found in biomass and coal chars as well [12, 51, 82, 95]. The mechanism that is currently believed to cause this phenomenon is the partial thermal degradation of the carbon matrix into aromatic radicals which remain in the matrix for a limited time [26]. The presence of these radicals in the carbon matrix decreases its viscosity and allows the particle to become plastic when stresses such as those created by the devolatilization gases are placed upon it. These aromatic radicals are present in the carbon matrix only for a short time before they become stabilized and form primary tars. Increasing the pressure increases the amount of time that these primary tar precursors are present

in the matrix, resulting in a decrease in the softening temperature and viscosity of the carbon matrix.

2. **Increasing pressure decreases the porosity of the char.**

   Increasing the pressure of the reactor had the effect of increasing the bulk density of the resultant pyrolysis char. This conclusion could also be stated as increasing pressure decreased the porosity of the pyrolysis char, since porosity is calculated as $1 - \rho_b/\rho_p$, where ρ_b is the bulk density and ρ_p is the particle density of the char. The porosity present in these chars is caused by the evolution of volatile gases during devolatilization. Increasing the pressure of the reactor will decrease the specific volume of these devolatilization gases, resulting in less total volume to generate void spaces in the char particles. Another reason for the decrease in porosity is that increasing pressure will increase the amount of PV work required to expand the particle. At a given volumetric expansion, doubling the pressure under which that expansion will take place will double the amount of work required, as shown by equation 100.

$$W = \int_{V_1}^{V_2} P dV \tag{100}$$

   Along with increasing the work required to expand the particle, higher pressure results in lower specific volumes of gases, decreasing the amount of energy available for expansion. The same amount of char mass in a smaller expanded volume will result in higher bulk density and lower porosity.

3. **Pressure affects the swelling and reagglomeration of char particles.**

   The inverse relationship between pressure and swelling manifested itself in a unique way: the physical size reduction of black liquor into smaller char particles at five bar pressure. At the conditions investigated, under five bar pyrolysis it was observed that at least seven times as many individual char particles were collected as black liquor particles were fed. This is thought to be due to the high heating rates of the PEFR causing sufficiently fast generation of devolatilization gases as to physically tear the char particle apart. This size reduction must have occurred immediately after the

black liquor entered the reactor since the five bar short residence time pyrolysis char consists of small spheres clustered together. This means that the size reduction of the black liquor occurred early enough that the smaller particles continued to devolatilize in a plastic state and generate additional hollow spheres.

Increasing the pressure to ten and fifteen bar resulted in less char particles being collected in the cyclone than black liquor particles fed into the reactor. There could be two possible explanations for this fact. First, the higher pressure of the ten and fifteen bar runs result in increased PV work required to expand the particle and smaller specific volumes of devolatilization gases. These factors result in insufficient energy for the black liquor to physically blow apart. The second explanation is the char particles blew apart at ten and fifteen bars and coalesced into larger particles prior to being collected. This coalescence of particles would be a function of the frequency and intensity of collisions, and thus the Reynolds number of the gas phase, which increased with increasing pressure in these experiments. Coalescence would also be a function of char plasticity. If black liquor chars behave similarly to coal chars with respect to pressure and plasticity, then increased pressure would make the char more plastic and better able to form larger particles.

A secondary effect of increasing pressure is an increase in the average size and wider size distribution of the char particles. This phenomenon was quantified by the volume distributions of the pyrolysis chars and supported by visual and electron microscopy of the char particles. The five bar chars consist of small spheres clustered together. Increasing the pressure to 10 bars results in slightly larger, individual spheres, with some amorphous char particles. Increasing the pressure to 15 bar results in a char that is almost exclusively larger, individual spheres and large amorphous particles.

This finding is classified as a secondary effect because it is largely thought to be due to the larger zone of separated flow present at the higher pressure experiments. This zone became larger with increasing pressure due to higher gas phase Reynolds numbers. The larger separated flow zone resulted in more char particles colliding

141

together at the entrance to the reactor, when they are in their initial plastic state. Increasing pressure may increase the plasticity of black liquor char in a manner similar to that observed in coal char [82, 95]. This would increase the tendency for the higher pressure chars to coalesce into larger particles.

4. **Pressure affects char surface area only at low carbon conversions.**

Black liquor pyrolysis char exists primarily as smooth, hollow spheres at short residence times. These chars would be classified as cenospheric under currently used coal terminology [82]. Direct evidence for this can be seen by scanning electron micrographs of the short residence time pyrolysis chars. All pictures show the existence of relatively smooth, spherical particles. Many pictures show broken particles which appear to have primarily hollow interiors.

As stated previously, the density of these pyrolysis char particles increase with increasing pressure. This increase in density results in a decrease in the specific surface area of these chars due to their mainly hollow, spherical geometry.

By comparing total surface area determined by nitrogen adsorption to the calculated external surface area of the chars (using their experimentally determined size distribution and density, and assuming spherical geometry), it was discovered that the total to external surface area ratio was between 1.2 and 2.0 for these chars. For a perfectly smooth and hollow sphere this ratio would be 2.0. This data indicates that the black liquor char initially consists of relatively smooth hollow spheres with little microporosity.

Further physical changes occur with the char as carbon conversion continues. Surface areas for gasification chars were shown to stay close to the short residence time pyrolysis char surface area until approximately 40% carbon conversion. Five bar gasification char had surface areas of approximately 19 m^2/g, ten bar gasification char of approximately 10 m^2/g, and fifteen bar approximately 4 m^2/g. After 40% carbon conversion the surface areas all increased irrespective of pressure to a maximum of around 115 m^2/g near 60% carbon conversion. This increase in surface area is due to

the reduction in char plasticity at higher carbon conversion. This reduction in plasticity may be due to the loss of aromatic radicals in the carbon matrix (as explained by Gadiou for coal chars [26]), or some other mechanism of thermal degradation of the carbon matrix. Once char plasticity is lost, increasing conversion from gasification results in an "erosion" of the relatively smooth surface of the char. This is supported by SEM micrographs of the black liquor char made at several different carbon conversions. After approximately 60% conversion, increasing carbon conversion results in the removal of the non-plastic carbon and allows for the molten inorganic salts to begin to dominate the surface characteristics of the char. As conversion approaches 100% chars from all pressures return to approximately 10 m^2/g and an approximately spherical shape.

10.2 Carbon Conversion

10.2.1 Carbon Conversion During Gasification

1. **The rate of carbon conversion is limited by inhibiting gas concentration near the char particles.**

   The commonly accepted Langmuir-Hinshelwood rate expressions for black liquor gasification are shown in equations 6 and 7 and are repeated here.

   $$-r = \frac{K_1[\mathrm{CO_2}]}{[\mathrm{CO_2}] + K_2[\mathrm{CO}]}$$

   $$-r = \frac{K_3}{1 + \frac{K_4[\mathrm{H_2}]}{[\mathrm{H_2O}]} + K_5[\mathrm{CO}]}$$

   The constant partial pressure experiments were particularly useful in determining the rate limiting step for carbon gasification because in these experiments the concentration of H_2O and CO_2 were equal at all pressures. The rate of carbon gasification, however, decreased from 33%/sec at 5 bar to 12.1%/sec at 15 bar. With a decreasing carbon conversion rate at constant reactant gas partial pressures, the next area that needed to be investigated was product gas inhibition of the reaction.

   The inhibiting gases near the particle are generated in devolatilization as well as gasification of black liquor. Increasing the pressure will decrease the ability of

CO to diffuse away from the gasification site due to decreased diffusivity, this fact is unavoidable. However, the presence of a zone of separated flow created by the black liquor injector wall allowed for experimentally investigating the effect of removing CO from the devolatilization stage. Decreasing the gas phase Reynolds number by 2/3 had the effect of lowering the rate of carbon gasification at five bar total pressure and fixed partial pressure from 33%/sec to 18.6%/sec. Given the R^2 values and difference in slopes of the linear best fit lines associated with these data there is a greater than 99.7% probability that these two slopes are not equal [94].

At both conditions there was a sufficient excess of CO_2 and H_2O to black liquor carbon present (at least 15:1 molar ratio), so there were no issue regarding limited amounts of reactant gas. The diffusivities of CO and H_2 in the gas phase will be the same since they are a function of temperature and pressure, both of which remained constant. It was therefore concluded that the decrease in carbon conversion rate associated with the decrease in gas phase Reynolds number was due to the smaller zone of separated flow created at the tip of the injector. This smaller zone of separated flow drew away less of the inhibiting gases that were generated by the black liquor when it rapidly devolatilized upon entering the reactor. This higher concentration of inhibiting gases inhibited the rate of carbon gasification vis á vis equations 6 and 7. When the gasification rates were compared at a constant superficial velocity no statistical difference was found.

This same phenomenon of separated flow zone removal of devolatilization CO can be used to explain the behavior of the constant mole fraction experiments. In these experiments, a large decrease in carbon gasification rate was seen between five and ten bar (28.1%/sec to 16.7%/sec), with a much smaller decrease at fifteen bar (15.3%/sec). As in the consant partial pressure experiments, the five bar experiments at constant mole fraction were at a higher gas velocity than the ten and fifteen bar experiments.

Since the mole fraction of CO_2, H_2O, CO, and H_2 were varied at a constant

molar ratio, the partial pressures of these gases increased with the total pressure. Despite the very different gas environments between the constant partial pressure and constant mole fraction experiments almost the same trends were seen regarding carbon gasification rate and pressure. This further supports the conclusion that the zone of separated flow at the injector tip plays an important role in the rate of carbon gasification at these conditions.

If both the gas phase Reynolds number and diffusivity play a role in the rate of carbon conversion, then at a fixed geometry, temperature, and gas composition an expression for gasification rate may be presented by equation 94, shown again here.

$$-r = K(Re)^a(D_{ab})^b$$

In equation 94 the constants K, a and b were solved for using actual gas phase Reynolds numbers and diffusivities and the experimentally determined gasification rates for the constant partial pressure gasification experiments at five, ten, and fifteen bar total pressure. This equation was then able to predict the slope of the five bar constant partial pressure gasification experiment at the lower Reynolds number to within 1% error.

2. **Increasing pressure decreases the critical diameter of char particles at a constant partial pressure.**

The rates of gasification for the constant partial pressure experiments were used to determine critical diameters of char particles using the Weisz modulus. The critical diameter is the diameter that a particle has to be less than in order to not have any significant intraparticle concentration gradients. Using experimentally determined porosities, surface areas, and gasification rates, diameters were calculated so that the Weisz modulus would be equal to 0.15, the commonly accepted value above which intraparticle concentration gradients become significant. It was found that increasing the total pressure from 5 to 15 bar at 0.25 bar H_2O and 0.5 bar CO_2 resulted in a critical diameter decrease from 0.91 to 0.59 millimeters at the experimental conditions investigated.

The decrease in critical diameter with increasing pressure is particularly important in light of the previously mentioned phenomenon of increasing particle size with increasing pressure. The increase in particle size is because of more char particle collisions due to a larger zone of separated flow, increased plasticity of the char due to tar precursors remaining in the solid char matrix for a longer period, or a combination of the two. Increasing pressure also decreases the diffusivity of the reactant and product gases. These two factors are contradictory to each other and will be an important consideration for black liquor nozzle design in future pressurized gasification reactors.

10.2.2 Carbon Conversion During Pyrolysis

3. <u>**Pyrolysis char yields are independent of pressure.**</u>

Carbon conversions under pyrolysis conditions of $900^{o}C$, $100\%N_2$, and 5, 10, and 15 bar were investigated. There was no effect seen of increasing pressure on the initial pyrolysis char yield, indicating that yield is independent of pressure. At residence times longer than approximately two seconds yields began to decrease more rapidly at lower pressures, but this was due to the faster carbon loss from secondary pyrolysis reactions at these pressures.

4. <u>**Pyrolysis carbon conversion rates are independent of pressure.**</u>

As with both groups of gasification experiments, increasing the pressure of pyrolysis decreased the rate of pyrolysis conversion. However, there was no statistical significance to the decrease in rates from five to ten bars of pressure. Furthermore, the five bar pyrolysis experiments were conducted at a higher gas velocity than the ten and fifteen bar experiments. Decreasing the velocity of the five bar experiment would further decrease the difference in pyrolysis conversion rates between five and ten bars. The conversion rates for the ten and fifteen bar pyrolysis experiments were almost identical.

The independence of pressure on pyrolysis conversion can also be explained by the zone of separated flow. Since the black liquor is the source of both the reaction and

inhibiting gases, changing the gas phase Reynold's number will affect the concentration of both equally. The overall difference in slopes for the pyrolysis runs is smaller than the gasification runs because the zone of separation removes any CO_2 or H_2O, as well as inhibiting gases, that are generated during devolatilization from near the particles.

10.3 Sulfur Phase Distribution

1. <u>Significant amounts of sulfur are lost to the gas phase at the pyrolysis conditions investigated.</u>

    The effect of pressure on the phase distribution of sulfur was determined by first analyzing the sulfur distribution under pyrolysis conditions. Under pyrolysis conditions 100% of the sulfur exists in the condensed phase at equilibrium, primarily as Na_2S. It was found that at short residence times a significant portion (up to 45%) of the sulfur was lost to the gas phase. At all pressure the first data point had the least amount of sulfur remaining in the condensed phase, with each increasing residence time having more sulfur until 100% of the sulfur returned to the condensed phase. This suggests that the actual maximum amount of sulfur lost occurred prior to the first residence time investigated.

    This observation is consistent with previous studies [72], in which concentrations of sulfur species in the gas and condensed phases were determined as a function of time and temperature at similar conditions. It was found by Sricharoenchaikul et al. that a significant portion of the sulfur (greater than the amount of organically bound sulfur) formed organic sulfur species in the gas phase. This was thought to occur through decomposition of thiosulfate to elemental sulfur, with that sulfur being inserted into hydrocarbon gases. Further reactions of the organic sulfur gases resulted in the sulfur returning to the condensed phase.

    In this work, higher pressures increased the time that it took for the sulfur to return to the condensed phase, indicating that a diffusional process was involved in the recapture of the sulfur. The sulfur containing gases could diffuse back to the char

surface, where they would react with the catalytic sodium and form Na_2S. Analysis of the sodium concentrations of pyrolysis char also showed that as the amount of sodium decreased in the char, the amount of sulfur increased. The presence of volatilized sodium and organic sulfur gases would also cause the formation of Na_2S, although this is probably of secondary importance in this study.

2. **Pressure has no effect on sulfur loss at the gasification conditions investigated.**

   Sulfur phase distributions under constant partial pressure gasification conditions were very consistent. Between 30 and 40% of the sulfur remained in the condensed phase at all pressures and residence times studied. In light of the observed mechanism from the pyrolysis experiments, what appears to happen is that sulfur is initially lost due to initial devolatilization and pyrolysis reactions. These gas phase sulfur species then react with the water also present in the gas phase to produce thermodynamically stable gas phase species, such as H_2S. This sulfur did not return to the condensed phase at the conditions investigated.

   In the constant mole fraction experiments similar sulfur behavior was observed. An equilibrium seemed to be established prior to the first data point, with the level of sulfur remaining in the condensed phase remaining constant across the range of residence times investigated. The amount of sulfur remaining in the char from the constant mole fraction experiments varies more than that in the char from the constant partial pressure experiments. This may be due to the wider sulfur equilibrium range of these experiments because of the varying partial pressure of H_2O. Increasing the pressure appears to slightly decrease the average sulfur remaining in the resultant gasification chars, but no statistical significance can be assigned to this observation.

10.4   Recommendations For Future Work

- Effect of temperature on black liquor gasification at elevated pressures

   This thesis indicates that the presence of inhibiting gases near the black liquor

particles limits the rate of carbon conversion. It has also shown that with careful operation, very good carbon conversion data can be obtained from the PEFR. With the operational knowledge gained from this project it would be interesting to quantify the effect of temperature on various aspects of black liquor gasification, including char yields and carbon gasification rates. Arrhenius plots of carbon conversion could be generated at different pressures and their activation energies compared with those obtained by TGA analysis.

- Effect of gas composition on black liquor gasification at elevated pressure

   The PEFR allows for a very wide range of gas partial pressures to be used for gasification reactions. The systematic variation of CO_2, H_2O, CO, and H_2 partial pressures would serve to better illustrate the relative importance of these gases on accelerating and inhibiting gasification reactions. Currently the system is limited to water partial pressures of approximately 0.25 bar due to condensation issues. Equipment modifications will be required to be able to significantly increase this limit.

- Gas phase analysis of components

   Analysis instruments (FTIR, CO_2/CO analyzers, etc.) are currently located on the exhaust gas train but they are not calibrated. This system should be calibrated and updated prior to the next large investigation conducted on this reactor. Gas phase compositions as a function of residence time and pressure will be very useful in eliciting the mechanisms and transient species involved in black liquor gasification.

- Condensed phase sulfur analysis

   Along with gas phase analysis, sulfur speciation in the condensed phase will be useful in eliciting mechanisms regarding sulfur species transitions and the effect of pressure on them. A capillary electrophoresis unit is now operable, and separate work has shown that it is possible to analyze PEFR char successfully with this unit.

- Collaboration with ETC-Pitea, Georgia Tech, and others to increase visibility of reactor

The PEFR is truly a world-class reactor. Unfortunately is is currently being under utilized. Collaborative efforts have been made in the past with several institutions. This work should increase in order to achieve greater exposure in the scientific world. The IPST should leverage their engineering and experimental expertise in cooperative agreements with ETC-Pitea, Georgia Tech, or others who have strengths in numerical modeling or other areas.

While not directly associated with the paper industry or forest biorefineries, I believe that investigations with coal would also serve as an important source of information. I believe that coal gasification is the technology that will be the major competitor with a thermochemical biorefinery. It would be helpful to have exact comparisons when discussing differences between the competing technologies. While significant amounts of data exist on coal gasification, oftentimes the only way to get the exact data needed is to produce it yourself.

CHAPTER XI

CONCLUSIONS

1. Effects of pressure on char physical characteristics occur primarily at short residence times.

2. Increasing pressure decreases the porosity of the char.

3. Pressure affects the swelling and reagglomeration of char particles.

4. Pressure affects char surface area only at low carbon conversions.

5. The rate of carbon conversion during gasification is limited by inhibiting gas concentration near the char particles.

6. Increasing total pressure decreases the critical diameter of char particles at a constant partial pressure of H_2O and CO_2.

7. Pyrolysis char yields are independent of pressure.

8. Pyrolysis carbon conversion rates are independent of pressure.

9. Significant amounts of sulfur are lost to the gas phase at short residence time at the pyrolysis conditions investigated.

10. Pressure has no effect on sulfur loss at the gasification conditions investigated.

APPENDIX A

TROUBLESHOOTING TIPS

A.1 PEFR

1. **Difficulty keeping constant pressure in reactor**

   There are many reasons why it would be difficult to keep a constant pressure in the PEFR since the reactor does not control to a pressure. Instead of pressure control, the mass coming in and out of the reactor are controlled. Equal flows coming in and out of the reactor should maintain a constant pressure. However, the evolution of gases from the black liquor and the countless places that gas can escape from the reactor make the situation much more difficult.

   When drawing a vacuum on the reactor I usually let the reactor sit at maximum vacuum for a minute or two with the pump off to see if the pressure slowly increases. This technique is only good for showing major leaks, as the pressure differential can be no greater than the atmospheric pressure in the high bay. Once the reactor is at operating conditions it is common for the pressure to decrease slowly. Snooping lines coming in and out of the reactor can isolate leaks. Common leak points include the twin valves, U-tube at the bottom of the collector (swagelock fitting needs to be kept clean of tar), differential pressure transducer between the feed bell and main reactor body, and all the fittings near the feed bell.

   The small size of the feed bell makes it possible to isolate the bell and determine the mass flow loss from the feed bell fittings by estimating the volume of the bell and recording the pressure as a function of time. The feed bell can be pressurized with house air up to approximately 7.5 bar. Snoop all swagelock fittings near the bell, as the daily removal of the bell for each set of runs cause these fittings to loosen over time.

Another problem that was encountered was the increasing of pressure during a run despite the mass flow controllers indicating that more flow was leaving the reactor than was coming into the reactor. This will happen if the quench flow setpoint is greater than 100 NLM (which is the maximum for this controller). Exceeding this setpoint must cause the flow controller to open completely, resulting in an unknown amount of gas entering the reactor. The quench readout on the labview screen, however, never exceeds 100. If this is the case then the pressure will quickly rise immediately after starting the gas flow. Another cause for this can be condensation in the exhaust mass flow controllers. This will occur if there are several runs performed in a row at or near 25kPa P_{H_2O}. The high partial pressure of water causes it to condense on the exhaust lines, which are under the same pressure as the rest of the reactor but not heated. Liquid present in the gas mass flow controllers will cause them to behave incorrectly. If possible, construct the run sequence so that there are pyrolysis or lower water pressure runs interspersed with the high water pressure runs. If this is not possible then blow out the exhaust lines with air at the end of the day, after the reactor is depressurized and cleaned.

2. **"Clean" gas phase in between each run**

At the end of each run (usually after 10 grams of BL were fed) I increased the exhaust gas flow from the reactor to 150% of incoming flow (or 400 NLM, whichever was less). This has the effect of "cleaning" out the product gases generated by gasification and pyrolysis of the black liquor. The FTIR spectra will clean up very quickly, ideally returning to the background spectra.

When conducting an experiment it is best to set the exhaust controller to make the pressure decrease approximately 0.02 bar/min. This slow decrease in pressure will prevent reaction gases from moving to other parts of the reactor, or even out of the reactor section and into the broader pressure vessel. If product gases do escape from the reactor section, then increasing the exhaust flow after stopping the black liquor will clean the FTIR spectra to a certain point, but it will not return to the original

composition.

3. **Pressure and temperature affect operational envelope**

   Changes in both pressure and temperature affect the operational envelope of the reactor. The most important variable in running the reactor is the ratio of primary and secondary velocities. Changing this ratio affects the speed with which the injector will plug. Increasing the ratio increases the time to plug the injector, but it can also result in poor particle capture and uncertain residence times. As a general rule, higher temperatures, lower superficial velocities, and lower pressures make the injector plug quicker. This may be due to heat traveling up the injector, causing the black liquor to swell and react inside the injector, causing a plug. Different liquors also have an effect on the ideal operational settings of the reactor.

4. **Plug blowout procedures**

   When the injector develops a plug it is sometimes possible to blow the plug off the end of the injector. This is done by closing the twin valves while the gas is still flowing to the reactor. The primary nitrogen will build up in the feed bell, causing a differential pressure to build between the bell and the main reactor. Do not let the differential pressure build above 0.3 bars, as this may cause the ceramic liner in the injector to get blown into the reactor as well. At 20 NLM primary nitrogen flow this corresponds to approximately one minute of gas flow after closing the twin valve.

   If the blowout is successful then the differential pressure between the feed bell and reactor will read the normal -0.01 bar value by the time you return to the control room from opening the twin valve. If there is still a positive pressure difference then positive pressure alone will not remove the plug.

   A second alternative that has worked for me is to allow the pressure in the reactor to drop below the setpoint. Shut the equalization valve and then pressurize the reactor. This will cause hot gases to flow up the injector, pushing on the plug from the other side. After pressurization is complete attempt to blow out the plug as before. This

technique works by either dislodging the plug from gas flow in the opposite direction, or by heating the plug and making it brittle when the next pressure pulse comes.

When blowing out a plug make sure that the gas is bypassing the cyclone, or the plug may end up in the cyclone and affect the results. Blowing out a plug with the collector positioned close to the injector may cause the plug to block the collector. This will be indicated by not enough gas leaving the reactor or by very poor char retrieval in the cyclone. Always make sure the control factor on the reactor is less than or equal to 1.0 when blowing out a plug, otherwise the high exhaust mass flow will cause the plug to get sucked toward the collector, increasing the probability of the collector plugging.

5. **Reactor condensation issues**

When running high partial pressures of water, condensation of water on cooled surfaces such as the collector can easily become a problem. Generally I waited until the collector coolant temperature rose above 40^oC before I performed a run at high water pressure. There are two ways of adjusting the temperature of the collector coolant: adjusting coolant flow with the globe valves or changing the number of radiators. I found that the more reliable way to adjust temperature is increasing or decreasing the number of radiators running. This will raise or lower the temperature of the entire coolant loop, so be careful not to overheat other sections of the reactor. I always increased the number of radiators if the temperature of any individual coolant section (injector, preheat, kiln, or collector) exceeded 60^oC. Also, as a rule, increasing pressure increases the temperature of the coolant loop by better heat transfer across the gas.

6. **Water pump issues**

The phase distribution of sulfur is very sensitive to the amount of water present in the gas phase. Therefore, when running water in a gasification experiment it is important to make sure the water addition rate is correct. After starting the gas and turning on the water pump I usually double-checked that the water pump was

running by going upstairs and checking that the lobed impeller on the water pump was moving. Sometimes the water pump kicks off, with no outside indication given short of looking at the impeller.

For the first run of the day involving water, allow the water to run for at least a couple of minutes before starting to feed the black liquor. This will give time for the water to fill the tubes leading to the water gas header and establish a constant level in the reactor. After the first run of the day the tubes are full and the delay is not necessary.

A.2 Surface Area Analyzer

1. **Vacuum cannot be established**

   Prior to adding nitrogen for measuring surface area, the surface area analyzer evacuates the sample to a pressure of less than 0.01 bar. Once this pressure is reached the vacuum pump is turned off and it is maintained for a user-specified period of time. If the pressure rises during this time then the run is aborted.

   The main reason why runs are aborted on this unit is inability to hold a vacuum. The placement of the O-ring in the compression fitting at the top of the glass sample tube is vitally important. It must be placed the correct distance down or proper seating of the fitting will not occur. Placing the O-ring too far down the tube may cause the ring to roll or twist when the fitting is tightened, again causing leakage. Finally, continue to tighten the fitting until it stops, or air will leak into the sample.

2. **Loss of liquid nitrogen during experiment**

   If the experiment goes longer than one hour it is important to keep the dewar filled with liquid nitrogen. A funnel is available for adding more nitrogen while the dewar is in position. When measuring P_o at the beginning of a day I usually added nitrogen in between the P_o measurement and the actual experiment. In between these two measurements the dewar comes back down, giving opportunity to refill it.

3. **Make sure glassware is clean and dry**

Never try to run the analyzer with glassware that has been cleaned that day. I tried cleaning the glass, rinsing with methanol, drying, heating the tubes in the degasser for an hour, and then doing experiments, but the readings were still bad. Always clean the day before, rinse with methanol, and dry overnight. Always handle clean glassware with gloves.

4. **Measuring dense or low surface area substances**

The instrument generally likes to have at least one square meter of material present in it for repeatable results. Very dense or very low surface area material may require additional sample to get the total area up to one meter.

APPENDIX B

CALCULATIONS

Gas Characteristics

	Diffusivity Constants		μ_g	ρ_g	ρ_g	ν_g	$[n_g]$	$[n_g]$	κ_g
Pressure (bar)	H_2O (m^2/sec)	CO_2 (m^2/sec)	N_2 (Pa-s)	N_2 (kg/m^3)	N_2 (mol/m^3)	N_2 (m^2/s)	H_2O (mol/m^3)	CO_2 (mol/m^3)	N_2 (W/mK)
5	5.77E-05	3.61E-05	4.61E-05	1.43E+00	51.207143	3.22E-05	2.56E+00	5.13E+00	7.49E-02

Film MT Calculations

Input	Value	Units	Comments
Y H2O	0.05		
Y CO2	0.1		
BLS Total C	0.33528	g C_{tot}/g BLS	average of all BL samples
BLS Carbonate	0.0426	g CO3/g BLS	average of all BL samples
molar conc C_{fix} in BLS	0.027	mol C_{fix}/g BLS	
Char particle diameter	3.02E-05	m	mean LLS diameter
Char particle surface area	2.87E-09	m^2	mean LLS diameter
Char particle volume	1.45E-14	m^3	mean LLS diameter
Char skeletal density	1.396E+03	kg/m^3	from Hg data
Char bulk density	3.030E+01	kg/m^3	from Hg data
Char Porosity	97.83%		from Hg data
Particle V_{term}	3.27E-04	m/s	$F_{drag} = F_{gravity}$
Reynolds #	3.07E-04		
Schmidt # H2O	0.56		
Schmidt # CO2	0.89		
Sherwood # H2O	2.01		Hines and Maddox Eq. 6.149
Sherwood # CO2	2.01		Hines and Maddox Eq. 6.149
k_c H2O	2.30E+01	m^3/(m^2-s)	Characteristic length =r/3
k_c CO2	1.44E+01	m^3/(m^2-s)	Characteristic length =r/3
C_{fix} MT limited gasification rate	3.81E-07	mol C_{fix}/s	
Time to burnout	**3.13E-05**	**seconds**	

Biot #, HT   9.69E-05
Biot #, MT   1.61E+01

5 Bar Kinetic Resistance Calculations

Film HT Calculations

$$\Delta H^o = \Delta H_0^o + R \int_{T_0}^{T} \frac{\Delta C_p^o}{R} \, dT$$

H_2O+C rate of reaction	1.69E-07	mol C$_{org}$/s	
CO$_2$+C rate of reaction	2.12E-07	mol C$_{org}$/s	
H2O+ C heat of reaction	1.36E+05	J/mol	Smith, Van Ness, and Abbot Eq. 4.18
CO2 + C heat of reaction	1.69E+05	J/mol	Values from Sm.V.N. &A. App. C
Reaction heat	**5.89E-02**	**W**	
Convective Heat Transfer term	1.51	W/m^2-K	Kreith and Bohn, Eq. 7.10
Surface Temperature	**1173.142**	**K**	
Gas Temp	1173.15	K	
Convection heat	**-3.36E-11**	**W**	
Stefan-Boltzmann Constant	5.67E-08	W/m^2-K^4	
emissivity	0.8		
View Factor	1		
Radiative Area	2.59E-02	m^2	Assume 0.1 meter of wall exposure
Wall Temp	1173.15	K	
Radiation Heat	**-5.89E-02**	**W**	Kreith and Bohn, Eq. 1.18
Energy Balance	**9.00E-13**	**W**	9.00E-03

Intra-Particle HT Calculations

Initial BLS thermal Conductivity	0.238	W/m-K	Kreith and Bohn, Anthracite Coal, A11
Swelled BLS thermal cond	7.84E-02	W/m-K	(1-porosity)*BLS+porosity*gas
Volumetric Heat Generation	4.07E+12	W/m^3	
Number of shells	2.00E+01		
del r	7.06E-07	m	

Shell #	r	T	
	1.00E-06	1161.03	From Spherical Shell Balance
1	1.71E-06	1161.13	
2	2.41E-06	1161.29	
3	3.12E-06	1161.49	
4	3.82E-06	1161.75	
5	4.53E-06	1162.07	
6	5.23E-06	1162.43	
7	5.94E-06	1162.85	
8	6.65E-06	1163.33	
9	7.35E-06	1163.85	
10	8.06E-06	1164.43	
11	8.76E-06	1165.07	
12	9.47E-06	1165.75	
13	1.02E-05	1166.49	
14	1.09E-05	1167.28	
15	1.16E-05	1168.12	
16	1.23E-05	1169.02	
17	1.30E-05	1169.97	
18	1.37E-05	1170.98	
19	1.44E-05	1172.03	
20	1.51E-05	1173.14	

$$T_r = T_s + \frac{Q}{6k}(R^2 - r)$$

5 Bar Kinetic Resistance Calculations (cont.)

Gas Characteristics

	Diffusivity Constants		μ_g	ρ_g	ρ_g	ν_g	$[n_g]$	$[n_g]$	κ_g
Pressure (bar)	H_2O (m^2/sec)	CO_2 (m^2/sec)	N_2 (Pa-s)	N_2 (kg/m^3)	N_2 (mol/m^3)	N_2 (m^2/s)	H_2O (mol/m^3)	CO_2 (mol/m^3)	N_2 (W/mK)
10	2.91E-05	1.79E-05	4.62E-05	2.87E+00	102.41429	1.61E-05	2.56E+00	5.13E+00	7.49E-02

Film MT Calculations

Input	Value	Units	Comments
Y H2O	**0.025**		
Y CO2	**0.05**		
BLS Total C	0.33528	g C_{tot}/g BLS	average of all BL samples
BLS Carbonate	0.0426	g CO3/g BLS	average of all BL samples
molar conc C_{fix} in BLS	0.027	mol C_{fix}/g BLS	
Char particle diameter	4.01E-05	m	mean LLS diameter
Char particle surface area	5.05E-09	m^2	mean LLS diameter
Char particle volume	3.38E-14	m^3	mean LLS diameter
Char skeletal density	1.606E+03	kg/m^3	from Hg data
Char bulk density	5.460E+01	kg/m^3	from Hg data
Char Porosity	96.60%		from Hg data
Particle V_{term}	1.03E-03	m/s	$F_{drag} = F_{gravity}$
Reynolds #	2.58E-03		
Schmidt # $_{H2O}$	0.55		
Schmidt # $_{CO2}$	0.90		
Sherwood # $_{H2O}$	2.02		Hines and Maddox Eq. 6.149
Sherwood # $_{CO2}$	2.03		Hines and Maddox Eq. 6.149
$k_{c\ H2O}$	8.80E+00	m^3/(m^2-s)	Characteristic length =r/3
$k_{c\ CO2}$	5.43E+00	m^3/(m^2-s)	Characteristic length =r/3
C_{fix} MT limited gasification rate	2.54E-07	mol C_{fix}/s	
Time to burnout	**1.97E-04**	**seconds**	

Biot #, HT   7.93E-04
Biot #, MT   1.59E+01

10 Bar Kinetic Resistance Calculations

Film HT Calculation

$$\Delta H^{o} = \Delta H_0^{o} + R \int_{T_0}^{T} \frac{\Delta C_p^{o}}{R} dT$$

H_2O+C rate of reaction	1.14E-07	mol C_{org}/s	
CO_2+C rate of reaction	1.40E-07	mol C_{org}/s	
H2O+ C heat of reaction	1.36E+05	J/mol	Smith, Van Ness, and Abbot Eq. 4.18
CO2 + C heat of reaction	1.69E+05	J/mol	Values from Sm.V.N. &A. App. C
Reaction heat	**3.93E-02**	**W**	
Convective Heat Transfer term	9.55	W/m^2-K	Kreith and Bohn, Eq. 7.10
Surface Temperature	**1173.145**	**K**	
Gas Temp	1173.15	K	
Convection heat	**-2.50E-10**	**W**	
Stefan-Boltzmann Constant	5.67E-08	W/m^2-K^4	
emissivity	0.8		
View Factor	1		
Radiative Area	2.59E-02	m^2	Assume 0.1 meter of wall exposure
Wall Temp	1173.15	K	
Radiation Heat	**-3.93E-02**	**W**	Kreith and Bohn, Eq. 1.18
Energy Balance	**2.73E-08**	**W**	2.73E+01

Intra-Particle HT Calculations

Initial BLS thermal Conductivity	0.238	W/m-K	Kreith and Bohn, Anthracite Coal, A11
Swelled BLS thermal cond	8.05E-02	W/m-K	(1-porosity)*BLS+porosity*gas
Volumetric Heat Generation	1.17E+12	W/m^3	
Number of shells	2.00E+01		
del r	9.53E-07	m	

Shell #	r	T	
	1.00E-06	1166.88	From Spherical Shell Balance
1	1.95E-06	1166.92	
2	2.91E-06	1167.00	$T_r = T_s + \dfrac{Q}{6k}(R^2 - r)$
3	3.86E-06	1167.10	
4	4.81E-06	1167.23	
5	5.76E-06	1167.38	
6	6.72E-06	1167.57	
7	7.67E-06	1167.78	
8	8.62E-06	1168.03	
9	9.57E-06	1168.30	
10	1.05E-05	1168.59	
11	1.15E-05	1168.92	
12	1.24E-05	1169.28	
13	1.34E-05	1169.66	
14	1.43E-05	1170.07	
15	1.53E-05	1170.52	
16	1.62E-05	1170.98	
17	1.72E-05	1171.48	
18	1.81E-05	1172.01	
19	1.91E-05	1172.56	
20	2.01E-05	1173.14	

10 Bar Kinetic Resistance Calculations (cont.)

Gas Characteristics

Pressure (bar)	Diffusivity Constants		μ_g	ρ_g	ρ_g	ν_g	$[n_g]$	$[n_g]$	κ_g
	H_2O (m^2/sec)	CO_2 (m^2/sec)	N_2 (Pa-s)	N_2 (kg/m^3)	N_2 (mol/m^3)	N_2 (m^2/s)	H_2O (mol/m^3)	CO_2 (mol/m^3)	N_2 (W/mK)
15	1.94E-05	1.19E-05	4.62E-05	4.29E+00	1.53E+02	1.08E-05	2.56E+00	5.13E+00	7.50E-02

Film MT Calculations

Input	Value	Units	Comments
Y H2O	**0.017**		
Y CO2	**0.033**		
BLS Total C	0.33528	g C_{tot}/g BLS	average of all BL samples
BLS Carbonate	0.0426	g CO3/g BLS	average of all BL samples
molar conc C_{fix} in BLS	0.027	mol C_{fix}/g BLS	
Char particle diameter	4.77E-05	m	
Char particle surface area	7.15E-09	m^2	mean LLS diameter
Char particle volume	5.69E-14	m^3	mean LLS diameter
Char skeletal density	1.079E+03	kg/m^3	mean LLS diameter
Char bulk density	6.560E+01	kg/m^3	from Hg data
Char Porosity	93.92%		from Hg data
Particle V_{term}	1.76E-03	m/s	from Hg data
Reynolds #	7.78E-03		$F_{drag} = F_{gravity}$
Schmidt # $_{H2O}$	0.56		
Schmidt # $_{CO2}$	0.91		
Sherwood # $_{H2O}$	2.04		Hines and Maddox Eq. 6.149
Sherwood # $_{CO2}$	2.04		Hines and Maddox Eq. 6.149
k_c $_{H2O}$	4.97E+00	m^3/(m^2-s)	Characteristic length =r/3
k_c $_{CO2}$	3.06E+00	m^3/(m^2-s)	Characteristic length =r/3
C_{fix} MT limited gasification rate	2.03E-07	mol C_{fix}/s	
Time to burnout	**5.00E-04**	**seconds**	

Biot #, HT   2.27E-03
Biot #, MT   1.67E+01

15 Bar Kinetic Resistance Calculations

Film HT Calculations

			$$\Delta H^o = \Delta H_0^o + R\int_{T_0}^{T}\frac{\Delta C_p^o}{R}\,dT$$
H_2O+C rate of reaction	9.11E-08	mol C_{org}/s	
CO_2+C rate of reaction	1.12E-07	mol C_{org}/s	
H2O+ C heat of reaction	1.36E+05	J/mol	Smith, Van Ness, and Abbot Eq. 4.18
CO2 + C heat of reaction	1.69E+05	J/mol	Values from Sm.V.N. &A. App. C
Reaction heat	**3.14E-02**	**W**	
Convective Heat Transfer term	24.23	W/m^2-K	Kreith and Bohn, Eq. 7.10
Surface Temperature	**1173.146**	**K**	
Gas Temp	1173.15	K	
Convection heat	**-7.18E-10**	**W**	
Stefan-Boltzmann Constant	5.67E-08	W/m^2-K^4	
emissivity	0.8		
View Factor	1		
Radiative Area	2.59E-02	m^2	Assume 0.1 meter of wall exposure
Wall Temp	1173.15	K	
Radiation Heat	**-3.14E-02**	**W**	Kreith and Bohn, Eq. 1.18
Energy Balance	**-1.65E-09**	**W**	-1.65E+00

Intra-Particle HT Calculations

Initial BLS thermal Conductivity	0.238	W/m-K	Kreith and Bohn, Anthracite Coal, A11
Swelled BLS thermal cond	8.49E-02	W/m-K	(1-porosity)*BLS+porosity*gas
Volumetric Heat Generation	5.52E+11	W/m^3	
Number of shells	2.00E+01		
del r	1.14E-06	m	

Shell #	r	T	
	1.00E-06	1168.71	From Spherical Shell Balance
1	2.14E-06	1168.73	$$T_r = T_s + \frac{Q}{6k}(R^2 - r)$$
2	3.29E-06	1168.78	
3	4.43E-06	1168.85	
4	5.57E-06	1168.94	
5	6.72E-06	1169.05	
6	7.86E-06	1169.18	
7	9.00E-06	1169.33	
8	1.01E-05	1169.50	
9	1.13E-05	1169.69	
10	1.24E-05	1169.90	
11	1.36E-05	1170.14	
12	1.47E-05	1170.39	
13	1.59E-05	1170.66	
14	1.70E-05	1170.96	
15	1.81E-05	1171.27	
16	1.93E-05	1171.60	
17	2.04E-05	1171.96	
18	2.16E-05	1172.33	
19	2.27E-05	1172.73	
20	2.39E-05	1173.15	

15 Bar Kinetic Resistance Calculations (cont.)

$$D_{A,mix} = \frac{1-X_A}{\dfrac{X_B}{D_{AB}} + \dfrac{X_C}{D_{AC}}}$$

$$D_{B,mix} = \frac{1-X_B}{\dfrac{X_A}{D_{AB}} + \dfrac{X_C}{D_{BC}}}$$

5 Bar

Binary Diffusion Constants (cm^2/sec)

Specie	A CO_2	B H_2O	C N_2
D_{i-A}		0.516	0.355
D_{i-B}	0.516		0.585
X_i	0.1	0.05	0.85

Mixture Diffusion Constants

	m^2/sec
$D_{CO2,mix}$	3.61E-05
$D_{H2O,mix}$	5.77E-05

10 Bar

Binary Diffusion Constants (cm^2/sec)

Specie	A CO_2	B H_2O	C N_2
D_{i-A}		0.258	0.178
D_{i-B}	0.258		0.293
X_i	0.050	0.025	0.925

Mixture Diffusion Constants

	m^2/sec
$D_{CO2,mix}$	1.79E-05
$D_{H2O,mix}$	2.91E-05

15 Bar

Binary Diffusion Constants (cm^2/sec)

Specie	A CO_2	B H_2O	C N_2
D_{i-A}		0.172	0.118
D_{i-B}	0.172		0.195
X_i	0.0333	0.0167	0.95

Mixture Diffusion Constants

	m^2/sec
$D_{CO2,mix}$	1.19E-05
$D_{H2O,mix}$	1.94E-05

Diffusion Constant Calculations

Pressure	λ.H2O (m)	λ.CO2 (m)
5	1.05E-07	4.70E-08
10	5.23E-08	2.35E-08
15	3.49E-08	1.57E-08

Pressure Bar	5	
Porosity %	0.978	
Bulk Density (g/m^3)	30300	

Conversion	S. A. (m^2/g)	Avg. Pore Radius. (m)
21.3	2.03E+01	3.19E-06
40.4	2.67E+01	2.42E-06
59.4	1.09E+02	5.93E-07
82.6	8.13E+01	7.94E-07
99.3	9.62E+00	6.71E-06

	λ.H2O/2Rp	λ.CO2/2Rp
21.3	1.64E-02	7.37E-03
40.4	2.16E-02	9.72E-03
59.4	8.82E-02	3.96E-02
82.6	6.58E-02	2.96E-02
99.3	7.79E-03	3.50E-03

Pressure Bar	10	
Porosity %	0.966	
Bulk Density (g/m^3)	54600	

Conversion	S. A. (m^2/g)	Avg. Pore Radius. (m)
39	9.59E+00	3.69E-06
53.6	6.96E+01	5.08E-07
61.5	8.32E+01	4.25E-07
69.3	7.97E+01	4.44E-07
81.9	7.14E+01	4.96E-07

	λ.H2O/2Rp	λ.CO2/2Rp
39	7.09E-03	3.18E-03
53.6	5.14E-02	2.31E-02
61.5	6.15E-02	2.76E-02
69.3	5.89E-02	2.65E-02
81.9	5.28E-02	2.37E-02

Pressure Bar	15	
Porosity %	0.939	
Bulk Density (g/m^3)	65600	

Conversion	S. A. (m^2/g)	Avg. Pore Radius. (m)
34.7	4.13E+00	6.93E-06
47.6	4.04E+01	7.09E-07
65.2	1.15E+02	2.49E-07
86.5	2.95E+01	9.70E-07
95.8	7.53E+00	3.80E-06

	λ.H2O/2Rp	λ.CO2/2Rp
34.7	2.52E-03	1.13E-03
47.6	2.46E-02	1.10E-02
65.2	7.00E-02	3.14E-02
86.5	1.80E-02	8.07E-03
95.8	4.58E-03	2.06E-03

Pressure Bar	5			Gas Concentrations			
Porosity %	0.978			H2O	CO2	Total Oxidizing Gas	Avg. BL Fixed C Conc (Wt%)
Bulk Density (g/m^3)	30300		%	5.00%	10.00%	15.00%	
	H2O	CO2	mole/m^3	2.56	5.13	7.69	32.2%
$\mathcal{D}_{ab\,(m^2/s)}$	5.77E-05	3.61E-05					
$\mathcal{T}_{ortuosity}$	7						

Conversion	S. A. (m^2/g)	Avg. Pore Radius. (m)	$\mathcal{D}_{H2O,k}$ (m^2/s)	$\mathcal{D}_{CO2,k}$ (m^2/s)	$\mathcal{D}_{H2O,eff}$ (m^2/s)	$\mathcal{D}_{CO2,eff\,(m^2/s)}$	Critical Diameter (m)
21.3	2.03E+01	3.19E-06	2.49E-03	1.60E-03	7.88E-06	4.93E-06	9.56E-04
40.4	2.67E+01	2.42E-06	1.89E-03	1.21E-03	7.82E-06	4.90E-06	9.53E-04
59.4	1.09E+02	5.93E-07	4.64E-04	2.97E-04	7.17E-06	4.50E-06	9.13E-04
82.6	8.13E+01	7.94E-07	6.22E-04	3.98E-04	7.38E-06	4.62E-06	9.26E-04
99.3	9.62E+00	6.71E-06	5.26E-03	3.36E-03	7.97E-06	4.99E-06	9.62E-04

Pressure Bar	10			Gas Concentrations			
Porosity %	0.966			H2O	CO2	Total Oxidizing Gas	Avg. BL Fixed C Conc (Wt%)
Bulk Density (g/m^3)	54600		%	2.50%	5.00%	7.50%	
	H2O	CO2	mole/m^3	2.56	5.13	7.69	32.2%
$\mathcal{D}_{ab\,(m^2/s)}$	2.91E-05	1.79E-05					
$\mathcal{T}_{ortuosity}$	7						

Conversion	S. A. (m^2/g)	Avg. Pore Radius. (m)	$\mathcal{D}_{H2O,k}$ (m^2/s)	$\mathcal{D}_{CO2,k}$ (m^2/s)	$\mathcal{D}_{H2O,eff}$ (m^2/s)	$\mathcal{D}_{CO2,eff\,(m^2/s)}$	Critical Diameter (m)
39	9.59E+00	3.69E-06	2.89E-03	1.85E-03	3.98E-06	2.45E-06	7.71E-04
53.6	6.96E+01	5.08E-07	3.98E-04	2.55E-04	3.74E-06	2.31E-06	7.48E-04
61.5	8.32E+01	4.25E-07	3.33E-04	2.13E-04	3.69E-06	2.28E-06	7.43E-04
69.3	7.97E+01	4.44E-07	3.48E-04	2.22E-04	3.71E-06	2.29E-06	7.44E-04
81.9	7.14E+01	4.96E-07	3.88E-04	2.48E-04	3.74E-06	2.30E-06	7.47E-04

Pressure Bar	15			Gas Concentrations			
Porosity %	0.939			H2O	CO2	Total Oxidizing Gas	Avg. BL Fixed C Conc (Wt%)
Bulk Density (g/m^3)	65600		%	1.67%	3.33%	5.00%	
	H2O	CO2	mole/m^3	2.56	5.13	7.69	32.2%
$\mathcal{D}_{ab\,(m^2/s)}$	1.94E-05	1.19E-05					
$\mathcal{T}_{ortuosity}$	7						

Conversion	S. A. (m^2/g)	Avg. Pore Radius. (m)	$\mathcal{D}_{H2O,k}$ (m^2/s)	$\mathcal{D}_{CO2,k}$ (m^2/s)	$\mathcal{D}_{H2O,eff}$ (m^2/s)	$\mathcal{D}_{CO2,eff\,(m^2/s)}$	Critical Diameter (m)
34.7	4.13E+00	6.93E-06	5.43E-03	3.47E-03	2.59E-06	1.59E-06	6.12E-04
47.6	4.04E+01	7.09E-07	5.55E-04	3.55E-04	2.51E-06	1.54E-06	6.03E-04
65.2	1.15E+02	2.49E-07	1.95E-04	1.25E-04	2.37E-06	1.46E-06	5.86E-04
86.5	2.95E+01	9.70E-07	7.60E-04	4.86E-04	2.54E-06	1.56E-06	6.06E-04
95.8	7.53E+00	3.80E-06	2.98E-03	1.90E-03	2.59E-06	1.59E-06	6.11E-04

Constant Partial Pressure Gasification Char Critical Diameter Calculations

		Units
ΔH$_r$ CO$_2$	1.69E+05	J/mol
ΔH$_r$ H$_2$O	1.36E+05	J/mol
C$_{surf}$ H$_2$O	2.56	mol/m^3
C$_{surf}$ CO$_2$	5.13	mol/m^3
T$_{surf}$	1173	K

$$(T_{max} - T_{surf})/T_{surf} = \text{Prater \#}$$

$$\text{Prater \#} = \beta_i = \frac{(-\Delta H_r) D_{eff} c_{surf}}{k_{part} T_{surf}}$$

Pressure	$\mathcal{D}_{H2O,eff}$ (m^2/s)	$\mathcal{D}_{CO2,eff}$ (m^2/s)	$k_{part,eff}$ (W/m*K)	β_{H2O}	β_{CO2}	$\beta_{CO2+H2O}$
5	7.17E-06	4.50E-06	0.078	-0.0271	-0.0424	-0.0696
10	3.69E-06	2.28E-06	0.080	-0.0136	-0.0209	-0.0346
15	2.37E-06	1.46E-06	0.085	-0.0083	-0.0127	-0.0210

Prater Number Calculations for Constant Partial Pressure Gasification Experiments

Pressure Bar	5		Gas Concentrations			
				H2O	CO2	Total Oxidizing Gas	Avg. BL Fixed C Conc (Wt%)

Porosity %	0.978						
Bulk Density (g/m^3)	30300		%	5.00%	10.00%	15.00%	
	H_2O	CO_2	mole/m^3	2.56	5.13	7.69	32.7%
$\mathcal{D}_{ab}$ (m^2/s)	5.77E-05	3.61E-05					
Diameter (m, Vol Avg)	3.02E-05						
r_{obs} (sec-1)	0.3300						
$\mathcal{T}$ortuosity	7						

Conversion	S. A. (m^2/g)	Avg. Pore Radius. (m)	$\mathcal{D}_{H2O,k}$ (m^2/s)	$\mathcal{D}_{CO2,k}$ (m^2/s)	$\mathcal{D}_{H2O,eff}$ (m^2/s)	$\mathcal{D}_{CO2,eff}$ (m^2/s)	m_w Weisz Modulus	Φ_i Theile Modulus	η Effectiveness Factor
21.3	2.03E+01	3.19E-06	2.49E-03	1.60E-03	7.88E-06	4.93E-06	1.52E-04	0.012	9.99990E-01
40.4	2.67E+01	2.42E-06	1.89E-03	1.21E-03	7.82E-06	4.90E-06	1.53E-04	0.012	9.99990E-01
59.4	1.09E+02	5.93E-07	4.64E-04	2.97E-04	7.17E-06	4.50E-06	1.67E-04	0.013	9.99996E-01
82.6	8.13E+01	7.94E-07	6.22E-04	3.98E-04	7.38E-06	4.62E-06	1.62E-04	0.013	9.99989E-01
99.3	9.62E+00	6.71E-06	5.26E-03	3.36E-03	7.97E-06	4.99E-06	1.50E-04	0.012	9.99990E-01

Weisz Modulus, Theile Modulus, and Effectiveness Factors For 5 Bar Constant Partial Pressure Experiments

Pressure Bar	10		Gas Concentrations			
				H2O	CO2	Total Oxidizing Gas	Avg. BL Fixed C Conc (Wt%)
Porosity %	0.966		%	2.50%	5.00%	7.50%	
Bulk Density (g/m^3)	54600		mole/m^3	2.56	5.13	7.69	32.7%
	H_2O	CO_2					
$\mathcal{D}_{ab}$ (m^2/s)	2.91E-05	1.79E-05					
Diameter (m, Vol Avg)	4.01E-05						
r_{obs} (sec-1)	0.1410						
$\mathcal{T}$ortuosity	7						

Conversion	S. A. (m^2/g)	Avg. Pore Radius. (m)	$\mathcal{D}_{H2O,k}$ (m^2/s)	$\mathcal{D}_{CO2,k}$ (m^2/s)	$\mathcal{D}_{H2O,eff}$ (m^2/s)	$\mathcal{D}_{CO2,eff}$ (m^2/s)	m_w Weisz Modulus	Φ_i Theile Modulus	η Effectiveness Factor
39	9.59E+00	3.69E-06	2.89E-03	1.85E-03	3.98E-06	2.45E-06	4.13E-04	0.020	9.9998E-01
53.6	6.96E+01	5.08E-07	3.98E-04	2.55E-04	3.74E-06	2.31E-06	4.38E-04	0.021	9.9998E-01
61.5	8.32E+01	4.25E-07	3.33E-04	2.13E-04	3.69E-06	2.28E-06	4.44E-04	0.021	9.9997E-01
69.3	7.97E+01	4.44E-07	3.48E-04	2.22E-04	3.71E-06	2.29E-06	4.42E-04	0.021	9.9998E-01
81.9	7.14E+01	4.96E-07	3.88E-04	2.48E-04	3.74E-06	2.30E-06	4.39E-04	0.021	9.9998E-01

Weisz Modulus, Theile Modulus, and Effectiveness Factors For 10 Bar Constant Partial Pressure Experiments

Pressure Bar	15		Gas Concentrations				
				H2O	CO2	Total Oxidizing Gas	Avg. BL Fixed C Conc (Wt%)
Porosity %	0.939		%	1.67%	3.33%	5.00%	
Bulk Density (g/m^3)	65600		mole/m^3	2.56	5.13	7.69	32.7%
	H_2O	CO_2					
$\mathcal{D}_{ab}$ (m^2/s)	1.94E-05	1.19E-05					
Diameter (m, Vol Avg)	4.77E-05						
r_{obs} (sec-1)	0.1210						
$\mathcal{T}$ortuosity	7						

Conversion	S. A. (m^2/g)	Avg. Pore Radius (m)	$\mathcal{D}_{H2O,k}$ (m^2/s)	$\mathcal{D}_{CO2,k}$ (m^2/s)	$\mathcal{D}_{H2O,eff}$ (m^2/s)	$\mathcal{D}_{CO2,eff}$ (m^2/s)	m_w Weisz Modulus	Φ_i Theile Modulus	η Effectiveness Factor
34.7	4.13E+00	6.93E-06	5.43E-03	3.47E-03	2.59E-06	1.59E-06	9.25E-04	0.030	9.9994E-01
47.6	4.04E+01	7.09E-07	5.55E-04	3.55E-04	2.51E-06	1.54E-06	9.53E-04	0.031	9.9994E-01
65.2	1.15E+02	2.49E-07	1.95E-04	1.25E-04	2.37E-06	1.46E-06	1.01E-03	0.032	9.9993E-01
86.5	2.95E+01	9.70E-07	7.60E-04	4.86E-04	2.54E-06	1.56E-06	9.45E-04	0.031	9.9994E-01
95.8	7.53E+00	3.80E-06	2.98E-03	1.90E-03	2.59E-06	1.59E-06	9.28E-04	0.030	9.9994E-01

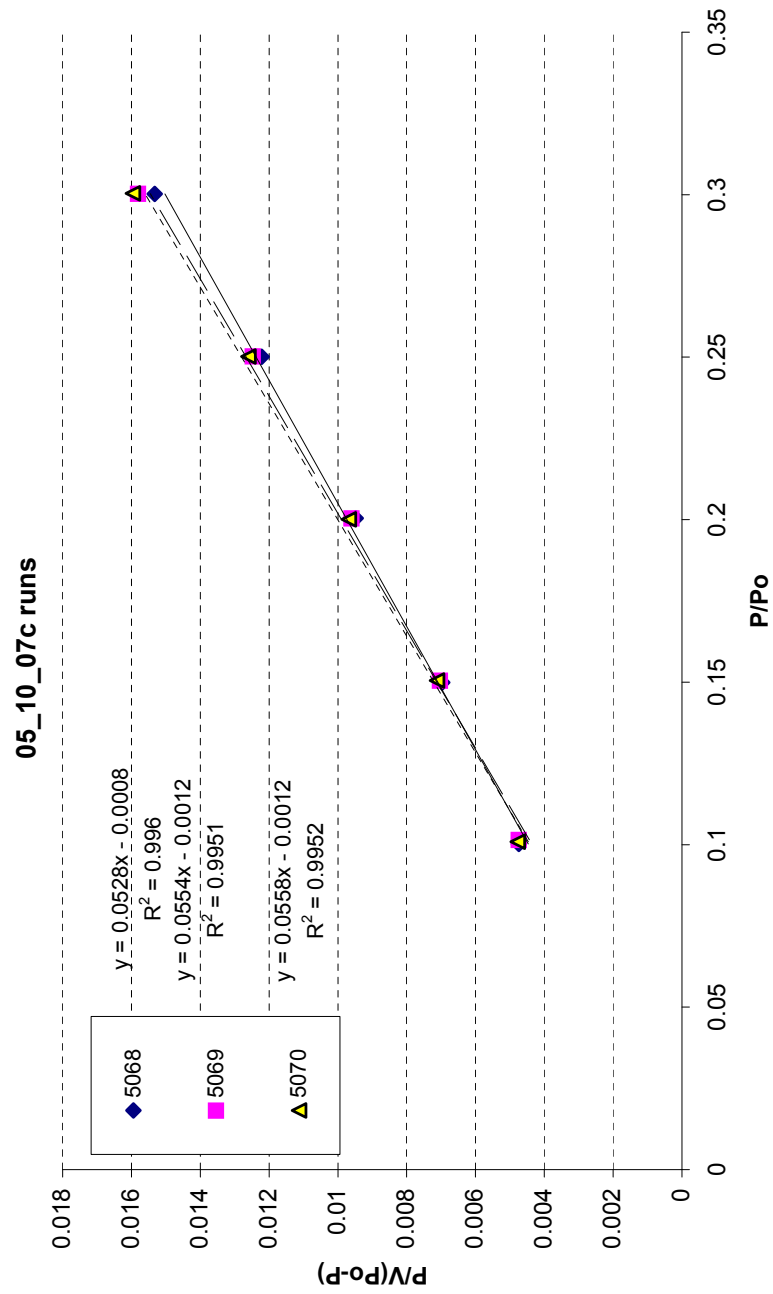Weisz Modulus, Theile Modulus, and Effectiveness Factors For 15 Bar Constant Partial Pressure Experiments

Run #	Pressure	% Conversion	Sample	Slope	Intercept	V_m 1/(S+I)	C 1+S/I	SA m^2/gram
05_10_07c	5	83.1	**5068**	0.0528	-0.0008	19.23	-65.00	83.726
05_10_07c	5	83.1	**5069**	0.0554	-0.0012	18.45	-45.17	80.327
05_10_07c	5	83.1	**5070**	0.0558	-0.0012	18.32	-45.50	79.739

05_10_07c runs

$y = 0.0528x - 0.0008$
$R^2 = 0.996$

$y = 0.0554x - 0.0012$
$R^2 = 0.9951$

$y = 0.0558x - 0.0012$
$R^2 = 0.9952$

Legend: 5068, 5069, 5070

Axis labels: P/Po, P/V(Po-P)

Example Calculation For Surface Area Analysis

5 Bar 30 Gasification

	NLM `@ 273K	mol/min	MW g/mol	kg/sec div by 4	Mass % Input Streams	Mass % At outlet	Mole % At outlet
1' N2	10.51	0.469187	28	5.474E-05	100.0%	9.0%	9.39%
2' N2	84.71	3.781624	28	4.412E-04	80.0%	72.8%	75.66%
CO2	11.16	0.498205	44	9.13375E-05	16.6%	15.1%	9.97%
H2O (mL/min)	4.48	0.248995	18	1.86746E-05	3.4%	3.1%	4.98%
CO	0	0	28	0	0.0%	0.0%	0.00%
H2	0	0	2	0	0.0%	0.0%	0.00%
Secondary Stream	100.35	4.528824		5.512E-04	100%	100%	100%

5 Bar 20 Gasification

	NLM `@ 273K	mol/min	MW g/mol	kg/sec div by 4	Mass % Input Streams	Mass % At outlet	Mole % At outlet
1' N2	7	0.312494	28	3.646E-05	100.0%	9.0%	9.38%
2' N2	56.48	2.52138	28	2.942E-04	80.0%	72.8%	75.67%
CO2	7.44	0.332136	44	6.08917E-05	16.6%	15.1%	9.97%
H2O (mL/min)	2.99	0.166182	18	1.24637E-05	3.4%	3.1%	4.99%
CO	0	0	28	0	0.0%	0.0%	0.00%
H2	0	0	2	0	0.0%	0.0%	0.00%
Secondary Stream	66.91	3.019699		3.675E-04	100%	100%	100%

10 Bar Gasification

	NLM `@ 273K	mol/min	MW g/mol	kg/sec div by 4	Mass % Input Streams	Mass % At outlet	Mole % At outlet
1' N2	14.01	0.625434	28	7.297E-05	100.0%	9.2%	9.39%
2' N2	124.18	5.543644	28	6.468E-04	89.84%	81.6%	83.19%
CO2	7.44	0.332136	44	6.08917E-05	8.46%	7.7%	4.98%
H2O (mL/min)	2.93	0.162847	18	1.22135E-05	1.70%	1.5%	2.44%
CO	0	0	28	0	0.0%	0.0%	0.00%
H2	0	0	2	0	0.0%	0.0%	0.00%
Secondary Stream	134.55	6.038627		7.199E-04	100%	100%	100%

15 Bar Gasification

	NLM `@ 273K	mol/min	MW g/mol	kg/sec div by 4	Mass % Input Streams	Mass % At outlet	Mole % At outlet
1' N2	20	0.89284	28	1.042E-04	100.0%	8.8%	8.93%
2' N2	192.71	8.60296	28	1.004E-03	93.1%	84.9%	86.06%
CO2	7.55	0.337047	44	6.1792E-05	5.7%	5.2%	3.37%
H2O (mL/min)	2.95	0.163959	18	1.22969E-05	1.1%	1.0%	1.64%
CO	0	0	28	0	0.0%	0.0%	0.00%
H2	0	0	2	0	0.0%	0.0%	0.00%
Secondary Stream	203.21	9.103966		1.078E-03	100%	100%	100%

3-D PEFR Residence Time Model Mass Flow Inputs

APPENDIX C

OPERATIONAL PROCEDURES

C.1 Spray Dryer

The liquor used in this thesis was collected by Steve Diperio of Weyerhaeuser during the week of January 3, 2005 via the same sample port as the liquor in Table 5. A 55 gallon drum of liquor arrived via Roadway Freight to the IEC the week of January 10.

Both an agitator and drum pump were used to get the liquor out of the 55 gallon drum. The drum of liquor was allowed to mix for approximately 1/2 hour at room temperature. After ensuring the liquor was well mixed the agitator was removed quickly and the drum pump was installed in the drum. The black liquor was then pumped out of the drum and into ten four-liter plastic bottles for later use. The four-liter plastic bottles of 50% solids black liquor were stored in a refrigerator until they were prepared for spray drying.

One day prior to spray drying, the black liquor was removed from the refrigerator. The lid of the bottle was loosened by running hot water over it prior to removal. The open four-liter bottle of liquor was then placed in a water bath and heated, which served two purposes. First, it decreased the viscosity of the liquor, making it easier to handle. Second, increasing the temperature of the liquor tended to decrease the appearance of crystals on the pre-spray dryer straining screen. An agitator was added to the liquor in the water bath. After approximately 10 minutes of stirring, 2,000 grams of the nominally 50% liquor was added to 1,000 grams of de-ionized water. This diluted black liquor was then placed on a hot plate and stirred until warm. The warm, 33% black liquor was then poured through a 250 μm sieve to separate out any particles that could plug the stationary atomizer in the spray dryer.

The dryer has two main configurations. The first uses a rotating atomizer (model CE-63) located at the top of the dryer. The liquid black liquor is fed into the atomizer via a pump or air pressure. When the black liquor reaches the end of the atomizer it hits

a rotating disk and is accelerated radially outward into the spray dryer. Many attempts were made to spray dry black liquor with the rotary atomizer, but the amperage to the motor would begin vacillating after approximately 10 minutes of feeding. After tearing the atomizer apart it was discovered that black liquor was forcing its way up the center shaft of the atomizer, contaminating the oil in the bearings. Stewart Gibson of Anhydro informed me that product contamination of the bearings is common in CE-63 atomizers due to the differential pressure between the dryer and the ambient atmosphere. Feed contamination can be eliminated by running the atomizer between 75 and 100% of design. I determined that these speeds would create drops that were too small to use in my experiments, since increasing the speed of the atomizer decreases the size of droplets created.

The second configuration involves a stationary nozzle, which was used for this thesis. A 0.04" nozzle was used, which was the larger of two available.

The black liquor was fed to the pump through a 3/8" tube from a stainless steel beaker, which was agitated to prevent settling. It was found that at least two 12-packs of nitrogen (approximately 200 standard cubic meters) connected together were needed to give sufficient run time to achieve good yield through the spray dryer. It was also noted that the flow rate of nitrogen through the high-flow regulator was insufficient to keep up with the draw rate of the induced draft fan in the spray dryer. This resulted in an unknown quantity of ambient air being sucked into the spray dryer as well, and may have resulted in partial oxidation of sulfur species in the liquor.

C.2 PEFR Daily Procedure

The PEFR needs to be turned on and brought up to idling status at least one day before performing an experiment. The following steps were performed to turn on the reactor.

1. On the third level

   (a) Turn on both coolant pumps

   (b) Turn on at least two of the three radiators

   (c) Make sure coolant is flowing through the flow meter immediately after the pumps

(d) Make sure coolant is flowing through the flow meter near the injector

2. In the control room

(a) Make sure both preheat and kiln key switches are in the "On" position

(b) Turn the main panel power key to "On"

(c) Turn the preheat and kiln key switches to the "Run" position

(d) Turn the four preheat and seven kiln controllers to "Manual"

(e) When the secondary thermocouples reach 150^oC, switch the preheat and kiln controllers to "Auto"

(f) Set the preheat and kiln controllers to 600^oC

On the day of an experiment the following steps were performed.

1. Bringing the reactor to conditions

(a) Set preheat and kiln controllers to desired temperature

(b) Open up Labview on PEFR computer and click "Run"

(c) Turn on collector motor and climb to catwalk with collector controller in hand

(d) Press up on collector controller while physically guiding the collector into the pressure vessel

(e) Raise collector to desired position, keeping your hand on the collector to feel for any unexpected resistance

(f) Insert U-tube into bottom of collector, making sure to use two wrenches to isolate the collector from torque while tightening the Swagelock fittings

(g) Make sure main exhaust valve is closed

(h) Make sure yellow handled 3-way valve on wall is going to vacuum pumps

(i) Make sure wall switch for vacuum #1 is on and wall switch for vacuum #2 is off

(j) Install twin valves at the top of the reactor. Make sure only one is closed

(k) Make sure water valve is closed

(l) Open valve from reactor to vacuum line

(m) Make sure purge valve is closed

(n) Engage vacuum contact on electrical panel in control room

(o) Confirm in Labview that pressure in reactor is decreasing

(p) While pressure is decreasing, fill LN bottle from dewar and pour into FTIR

(q) Open gas valve on LN dewar and make sure nitrogen is flowing through the FTIR

(r) When pressure in vessel reaches 0.3 bar turn on vacuum #2 and quickly turn off vacuum #1

(s) When pressure in vessel reaches 0.04 bar close the valve between the vacuum line and the reactor

(t) Disengage the vacuum contact in the control room and wait for at least one minute to make sure the pressure stays constant

(u) Open up 12-pack of nitrogen and valve to reactor

(v) Define experimental conditions in Labview

(w) Once conditions are defined, click proceed to begin pressurizing reactor

2. Putting liquor in the reactor

   (a) Make sure LIW controller is off

   (b) Remove liquor from vacuum oven and place in LIW feeder. Reassemble feeder, making sure that the walls of the cylinder are properly placed in the grooves in the top lid

   (c) Place feeder on strain gauge and hook up wires to power source

   (d) Use electric winch to move feed bell into place, making sure of proper placement of bell and gasket

   (e) Place at least six bolts into holes and hand tighten nuts

   (f) Use ratchet to tighten at least three opposing bolts to ensure proper seating of gasket

(g) Connect vacuum pump to fitting and turn on

(h) Tighten all bolts on feed bell

(i) Look in Labview to ensure that feed bell pressure is decreasing

(j) When pressure in feed bell gets to 0.09 bar, shut valve from pump to bell and turn off pump

(k) Wait at least 1 minute to make sure pressure does not increase

(l) Open pressure equalization valve 1.25 turns and allow the main reactor vessel and feed bell to equilibrate

3. When the reactor is at reaction conditions

(a) Create file on FTIR computer for the spectra to be stored. Reset filename to proper date

(b) Place cyclone into fittings

(c) Position heat gun on collector cross-bar so that it can heat the cyclone

(d) Make sure that the char purge valve and cyclone exhaust valves are closed

(e) Slowly open main exhaust valve

(f) Slowly open cyclone feed valve

(g) Make sure cyclone 3 way valve is toward the mass flow controller

(h) Turn on heat gun

(i) Make sure yellow-handled 3 way valve on wall is going to atmosphere

(j) Make sure reaction gases are turned on. If CO is being used personal monitor should be worn

4. At beginning of experiment

(a) Open twin valves

(b) Affix buzzer to twin valves and turn on

(c) Close equalization valve

(d) Make sure water valve is open if needed

(e) Ensure main exhaust valve open, bypass valve open, sample valve closed

(f) Ensure cyclone inlet valve open, cyclone 3 way valve is toward mass flow controller, and yellow handled 3-way valve on wall is toward atmosphere

(g) Open purge valve

(h) Start gas flow

(i) Turn on water pump if needed

(j) Watch pressure in Labview and make sure it is steady

(k) Open sample valve, close bypass valve, and open FTIR valve

(l) Switch 3 way valve on FTIR from N_2 to sample

(m) Collect background on FTIR

(n) Begin gas sampling

(o) Set desired voltage on feeder controller

(p) Record weight of sample prior to starting feeder

(q) Begin sample log in Labview

(r) Reset timer, begin timing, and turn feed controller to forward

5. At end of experiment

(a) Record time

(b) Turn feed controller to off, pause, then turn to reverse for 3 seconds

(c) Record final sample weight

(d) Turn off water pump

(e) Increase mass flow of exhaust controller to draw down pressure in reactor and remove any product gases

(f) Wait at least 4 minutes after reversing feeder, then turn off gas

(g) Stop sampling on FTIR

179

(h) Switch 3 way valve on FTIR from sample to N_2

(i) Turn off buzzer, close twin valve, and open equalization valve

(j) Close main exhaust valve, close sample valve, open bypass valve

(k) Close cyclone feed valve, move 3 way valve after cyclone toward vent

(l) Place ventilation hose over cyclone vent and slowly relieve pressure on cyclone

(m) Remove cyclone from fittings, quickly placing caps on inlet and outlet fittings

(n) Place sealed cyclone in glove box and turn on N_2. Do not open cyclone until oxygen monitor reads less than 1.0%

(o) Remove char from cyclone in glove box and place in glass jars for later analysis

(p) Place new cyclone in fittings and reset valves

6. At end of day

(a) Isolate feed bell from main reactor by closing one twin valve and equalization valve

(b) Slowly depressurize feed bell by slightly opening exhaust needle valve

(c) Slowly depressurize main reactor by partially opening ball valve to vacuum line

(d) When feed bell is depressurized, remove bolts, raise bell, and remove LIW feeder

(e) Quickly return liquor to vacuum oven, replacing what has been used, and taking a 1 gram sample for analysis

(f) Disassemble LIW feeder, clean with water, and hang to dry

(g) When main reactor has depressurized, remove U-tube from bottom of collector and clean with water

(h) Lower collector, clean with brush, water, and brake cleaner

(i) Place catch pan over top of collector prior to cleaning the injector

(j) Remove twin valves, clean with water, and hang to dry

(k) Clean injector by running a dry brush down to the tip, being careful to stop at the mark indicated on the tube. Repeat three times

(l) Attach a moist rag to brush and run down to the tip, repeat three times, cleaning the rag in between each time

(m) Remove catch pan from collector and visually inspect the injector using a mirror and a monocle

(n) Once injector tip is properly clean, reduce preheat and kiln temperature controllers to 600^oC

(o) Make sure all reaction gases and nitrogen are turned off

(p) Disassemble and clean cyclones with water, lay out to dry

(q) Clean glove box with wet and dry towels

C.3 Surface Area Analyzer

The procedure followed for using the surface area analyzer was as follows:

1. The day before an experiment

   (a) Clean test tubes and stoppers with soap, water and brush

   (b) Rinse with methanol

   (c) Place upside down to dry. Handle stoppers and tubes with gloves after methanol rinse

2. The day of an experiment, instrument setup

   (a) Open He and N_2 gas bottles, set regulators to 18psi

   (b) Turn on degas heater and set degas temp

   (c) Add liquid N_2 to dewar, wait at least 10 minutes for temperature equilibration

   (d) Install blank glass tube into instrument

   (e) Press P_o button to obtain saturation pressure

   (f) Number and obtain tare weight of stoppers and tubes

   (g) Put 0.1 grams of char into tube and place in degas heater

(h) Turn on N_2 gas to degas lance and put in top of tube, replace stopper

3. First run of the day

   (a) Remove sample from heater and let cool for 10 minutes

   (b) Change setup to measure free space

   (c) Get post degas weight of char and place in analyzer

   (d) Press analyze and input required information

   (e) If analysis goes longer than 45 minutes, fill dewar with liquid N_2

4. Other runs

   (a) Change setup to previous free space

   (b) Run experiment the same as the first run

APPENDIX D

SLOPE STATISTICAL COMPARISON

A linear model was used to determine the statistical significance between the different slopes in Figures 45, 50, 51, 53, and 54. The linear model used is of the form shown in equation 101,

$$Y_i = \beta_0 + \beta_1 X_i + \beta_2 I_i + \beta_3 I_i X_i \tag{101}$$

where Y is fixed carbon conversion, X is time in seconds, and I is an indicator (either 1 or 0) depending on the group of data. The data input table for Figure 53 is shown in Table 29.

Table 29: Linear model input table for Figure 53 [94]

Observation	X	Y	Group	I	X×I
1	0.56	22.072	30cm/s	0	0
2	0.84	29.461	30cm/s	0	0
3	1.1	34.821	30cm/s	0	0
4	1.34	44.972	30cm/s	0	0
5	1.58	50.946	30cm/s	0	0
6	1.91	65.301	30cm/s	0	0
7	2.26	83.612	20cm/s	0	0
8	2.9	93.524	30cm/s	0	0
9	0.86	38.926	20cm/s	1	0.86
10	1.62	46.667	20cm/s	1	1.62
11	2.3	69.031	20cm/s	1	2.3
12	2.96	74.91	20cm/s	1	2.96

Using the values for I shown in Table 29 and inserting into equation 101, the equations for the 30 cm/s and 20 cm/s groups simplify to equations 102 and 103, respectively.

$$Y_i = \beta_0 + \beta_1 X_i \tag{102}$$

$$Y_i = (\beta_0 + \beta_2) + (\beta_1 + \beta_3) X_i \tag{103}$$

Table 29 is entered into a statistical program such as JMP. With Y as the dependent variable, a linear model is created using the model effects of X, I, and X×I. This model then gives parameter estimates for β_0 through β_3, shown in Table 30. Substituting the parameter values from Table 30 into equations 102 and 103 gives the result of the best-fit lines in Figure 53.

Table 30: Linear model output table for Figure 53

Variable	Parameter Estimate	Standard Error	t Value	Pr> $|t|$
β_0	1.6303	3.5659	0.46	.6597
β_1	32.9597	2.0723	15.90	<0.0001
β_2	19.7037	6.6947	2.94	0.186
β_3	-14.3295	3.4158	-4.20	0.0030

We are interested in determining if the slopes in equations 102 and 103 are different. This is the case only if β_3 is not equal to zero. To determine this, we use the null hypothesis of $\beta_3=0$. Table 30 shows that P-value for β_3 is equal to 0.003, which means that the probability of $\beta_3 = 0$ is 0.3%. Therefore there is a 99.7% chance that β_3 is not equal to zero and the slopes are different.

REFERENCES

[1] "http://webbook.nist.gov/chemisty/name-ser.html," tech. rep., NIST, April 2006.

[2] "Method 3050b," Method Revison 2, EPA, www.epa.gov/epaoswer/hazwaste/test/pdfs /3050b.pdf, April 2006.

[3] "Method 6010b," Method Revison 2, EPA, www.epa.gov/epaoswer/hazwaste/test/pdfs /6010b.pdf, April 2006.

[4] BACKMAN, R. and HUPA, M., "Gasification of black liquor at elevated pressures - thermodynamic analysis," Tech. Rep. 90-10, Abo Akademi, Turku, Finland, 1990.

[5] BAYARSAIKHAN, B., HAYASHI, J.-I., SHIMADA, T., SATHE, C., LI, C.-Z., TSUTSUMI, A., and CHIBA, T., "Kinetics of steam gasification of nascent char from rapid pyrolysis of a victorian brown coal," *Fuel*, vol. 84, pp. 1612–1621, 2005.

[6] BERTA, Y., *Hitachi S-800 Operating Instructions.* Center for Nanomaterial Characterization, School of Material Science, Georgia Institute of Technology, www.mse.gatech.edu/Research/Equipment-Facilities/CNC/S800/s800.html, April 2006.

[7] BIERMANN, C. J., *Essentials of Pulping and Papermaking.* Academic Press, Inc, 1993.

[8] BIRD, R., STEWART, W., and LIGHTFOOT, E., *Transport Phenomena.* John Wiley and Sons, 2 ed., 2002.

[9] BRUNAUER, S., EMMETT, P., and TELLER, E., "Adsorption of gases in multimolecular layers," *Journal of the American Chemical Society*, vol. 60, p. 309, 1938.

[10] CAMERON, J. H. and GRACE, T. M., "Kinetic study of sulfate reduction with kraft black liquor char," *Ind. Eng. Chem. Fundamen.*, vol. 24, pp. 443–449, 1985.

[11] CENGEL, Y. A. and BOLES, M. A., *Thermodynamics: An Engineering Approach.* McGraw Hill, 2 ed., 1994.

[12] CETIN, E., MOGHTADERI, B., GUPTA, R., and WALL, T., "Influence of pyrolysis conditions on the structure and gasification reactivity of biomass chars," *Fuel*, vol. 83, pp. 2139–2150, 2004.

[13] CHAI, X.-S., LUO, Q., and ZHU, J., "Analysis of nonvolatile species in a complex matrix by gas chromatography," *Journal of Chromatography A*, vol. 909, pp. 249–257, 2001.

[14] DAHLBOM, J., OLM, L., and TEDER, A., "The characteristics of mss-aq pulping - a new pulping process," *Tappi Journal*, pp. 257–261, March 1990.

[15] FLAXMAN, R. and HALLETT, W., "Flow and particle heating in an entrained flow reactor," *Fuel*, vol. 66, pp. 607–611, May 1987.

[16] FOGLER, H. S., *Elements of Chemical Reaction Engineering*. Prentice Hall International Series in the Physical and Chemical Engineering Sciences, Prentice Hall, 3 ed., 1999.

[17] FREDERICK, W. J. and GRACE, T. M., "A study of evaporator scaling calcium carbonate scales," Tech. Rep. 3234, Institute of Paper Chemistry, Appleton, WI, November 1977.

[18] FREDERICK, W. and HUPA, M., "Gasification of black liquor at elevated pressures part 2: Rate data with co_2 and water vapor," Tech. Rep. 90-12, Abo Akademi University, Turku, Finland, 1990.

[19] FREDERICK, W. and HUPA, M., "Gasification of black liquor char with co_2 at elevated pressures," Tech. Rep. 90-14, Abo Akademi University, Turku, Finland, 1990.

[20] FREDERICK, W. and HUPA, M., "Gasification of black liquor char with co_2 at elevated pressures," *Tappi Journal*, vol. 74(7), pp. 177–184, July 1991.

[21] FREDERICK, W. and HUPA, M., "The effects of temperature and gas composition on swelling of black liquor droplets during devolatilization," *Journal of Pulp and Paper Science*, vol. 20(10), pp. J274–J279, 1994.

[22] FREDERICK, W., HUPA, M., and UUSIKARTANO, T., "Volatiles and char carbon yields during black liquor pyrolysis," *Bioresource Technology*, vol. 48, pp. 59–64, 1994.

[23] FREDERICK, W., NOOPILA, T., and HUPA, M., "Combustion behavior of black liquor at high solids firing," *Tappi Journal*, vol. 74(12), pp. 163–170, 1991.

[24] FREDERICK, W., NOOPILA, T., and HUPA, M., "Swelling of spent pulping liquor droplets during combustion," *Journal of Pulp and Paper Science*, vol. 17(5), pp. J164–J170, 1991.

[25] FREDERICK, W., WAG, K., and HUPA, M., "Rate and mechanism of black liquor char gasification with co_2 at elevated pressures," *Industrial Engineering Chemistry Research*, vol. 32, pp. 1747–1753, 1993.

[26] GADIOU, R., BOUZIDI, Y., and PRADO, G., "The devolatilisation of millimetre sized coal particles at high heating rate: the influence of pressure on the structure and reactivity of the char," *Fuel*, vol. 81, pp. 2121–2130, 2002.

[27] GAIRNS, S. A., KUBES, G. J., and VAN HEININGEN, A. R. P., "Sodium loss mechanisms and the formation of reduced sodium during the fast pyrolysis of kraft black liquor," *Pulp and Paper Canada*, vol. 46, 1996.

[28] GRACE, T. M. and MALCOM, E. W., eds., *Pulp and Paper Manufacture: Alkaline Pulping*, vol. 5. Canadian Pulp and Paper Association, 3 ed., 1996.

[29] HARPER, F., GRACE, T., CLAY, D., and McDONOUGH, T., "Sulfur release during the pyrolysis of kraft black liquor," Tech. Rep. 402, The Institute of Paper Science and Technology, October 1991.

[30] HARPER, F. D., *Sulfur Release During the Pyrolysis of Kraft Black Liquor*. PhD thesis, The Institute of Paper Science and Technology, June 1989.

[31] HARRIS, D. J., ROBERTS, D. G., and HENDERSON, D. G., "Gasification behavior of austrailian coals at high temperature and pressure," *Fuel*, vol. 85, pp. 134–142, 2006.

[32] HINES, A. and MADDOX, R., *Mass Transfer Fundamentals*. Prentice Hall, 1985.

[33] HUPA, M., SOLIN, P., and HYOTY, P., "Combustion behavior of black liquor droplets," *Journal of Pulp and Paper Science*, vol. 13(2), pp. J67–J72, 1987.

[34] IISA, K., COURCHENE, C., ANAND, F., REALFF, M., and FREDERICK, J., "Process systems considerations in forest biorefineries with thermochemical processing of wood wastes," in *AICHE Conference Proceedings*, (Cincinnati, OH), November 2005.

[35] IISA, K. and YOUNG, C., "Pyrolysis gas and char compositon as a function of temperature, pressure, and residence time." Contracted work with Chalmers University, January 2006.

[36] KAJITANI, S., HARA, S., and MATSUDA, H., "Gasification rate analysis of coal char with a pressurized drop tube furnace," *Fuel*, vol. 81, pp. 539–546, 2002.

[37] KAPTEIJN, F., ABBEL, G., and MOULJIN, J., "Co_2 gasification of carbon catalysed by alkali metals," *Fuel*, vol. 63, pp. 1036–1042, August 1984.

[38] KAPTEIJN, F. and MOULIJN, J., "Kinetics of the potassium carbonate catalysed co_2 gasification of activated carbon," *Fuel*, vol. 62(2), pp. 221–225, February 1983.

[39] KAPTEIJN, F., PEER, O., and MOULIJN, J., "Kinetics of the alkali carbonate catalysed gasification of carbon 1: Co_2 gasification," *Fuel*, vol. 65(10), pp. 1371–1376, October 1986.

[40] KREITH, F. and BOHN, M., *Principles of Heat Transfer*. PWS Publishing Company, 5 ed., 1997.

[41] LANSDELL, G. M., FREDERICK, W. J., and SCHMIDL, W., "An investigation of the accelerated $caco_3$ fouling in evaporators processing black liquor from displacement batch kraft pulping," in *AIChE Spring Meeting*, March 2000.

[42] LEVENSPIEL, O., *Chemical Reaction Engineering*. John Wiley and Sons, 3 ed., 1999.

[43] LEVINE, I. N., *Physical Chemistry*. McGraw-Hill Book Company, 1978.

[44] LI, J. and VAN HEININGEN, A., "Mass transfer limitations ...black liquor char by co_2," *Journal of Pulp and Paper Science*, vol. 12, no. 5, 1986.

[45] LI, J. and VAN HEININGEN, A., "Kinetics of co_2 gasification of fast pyrolysis black liquor char," *Industrial Engineering Chemistry Research*, vol. 29(9), pp. 1776–1785, 1990.

[46] LI, J. and VAN HEININGEN, A., "Kinetics of gasification of black liquor char by steam," *Industrial Engineering Chemistry Research*, vol. 30(7), pp. 1594–1601, 1991.

[47] LI, J. and VAN HEININGEN, A. R. P., "Sulfur emissions during slow pyrolysis of kraft black liquor," *Tappi Journal*, vol. 74(3), pp. 237–239, 1991.

[48] LI, J. and VAN HEININGEN, A. R. P., "The rate process of h2s emission during steam gasification of black liquor char," *Chemical Engineering Science*, vol. 49(24), pp. 4143–4151, 1994.

[49] LI, Z., LI, J., and KUBES, G. J., "Kinetics of delignification and cellulose degradation during kraft pulping with polysulphide and anthraquinone," *Journal of Pulp and Paper Science*, vol. 27(7), pp. 234–239, 2002.

[50] MACLEOD, J. M., "Alkaline sulfite-anthraquinone pulps from softwoods," *Journal of Pulp and Paper Science*, vol. 13(2), pp. J44–J49, 1987.

[51] MATSUOKA, K., AKIHO, H., XU, W.-C., GUPTA, R., WALL, T. F., and TOMITA, A., "The physical character of coal char formed during rapid pyrolysis at high pressure," *Fuel*, vol. 84, pp. 63–69, 2005.

[52] MEIJER, R., KAPTEIJN, F., and MOULIGN, J., "Kinetics of the alkali-carbonate catalysed gasification of carbon 3: H2o gasification," *Fuel*, vol. 73(5), pp. 723–730, 1994.

[53] MEIJER, R., VAN DER LINDEN, B., KAPTEIJN, F., and MOULIJN, J., "The interaction of h2o, co2, h2, and co with the alkali-carbonate/carbon system: A thermogravimetric study," *Fuel*, vol. 70, pp. 205–214, February 1991.

[54] Micromeritics, One Micromeritics Drive Norcross, GA 30093, *Gemini II 2370 Operating Manual*, October 1996.

[55] Micromeritics, One Micromeritics Drive Norcross GA 30093, *AutoPore IV Operating Manual*, June 2000.

[56] MILLER, P. T., CLAY, D., and LONSKY, W., "The influence of composition on the swelling of kraft black liquor during pyrolysis," Tech. Rep. 169, Institute of Paper Chemistry, Appleton, WI, May 1986.

[57] MOULIJN, J., CERFONTAIN, M., and KAPTEIJN, F., "Mechanism of the potassium catalysed gasification of carbon in co2," *Fuel*, vol. 63, pp. 1043–1047, August 1984.

[58] NENES, A., "Che 6200 advanced transport phenomena." Class Notes, January 2003.

[59] NOHLGREN, I., SCRICHAROENCHAIKUL, V., SINQUEFIELD, S., THELIANDER, H., and FREDERICK JR., W. J., "Black liquor gasification with direct causticization using titanates in a pressurized entrained flow reactor. part 2: Carbon and carbon species transformations," *Journal of Pulp and Paper Science*, vol. 29(10), pp. 348–355, 2003.

[60] NOHLGREN, I., SRICHAROENCHAIKUL, V., SINQUEFIELD, S., FREDERICK, W. J., and THELIANDER, H., "Black liquor gasification with direct causticization using titantes in a pressurized entrained flow reactor. part 1: Kinetics of the causticization reaction," *Journal of Pulp and Paper Science*, vol. 29(4), pp. 107–113, 2003.

[61] NOHLGREN, I. M. and SINQUEFIELD, S. A., "Black liquor gasification with direct causticization using titanates: Equilibrium calculations," *Industrial Engineering Chemistry Research*, vol. 43, pp. 5996–6000, 2004.

[62] OVERACKER, N., WAG, K., FREDERICK, W., and WHITTY, K., "Application of a mechanism-based rate equation to black liquor gasification rate data," Tech. Rep. 95-2, Abo Akademi University, Turku, Finland, 1995.

[63] PERRY, R. H. and GREEN, D. W., *Perry's Handbook of Chemical Engineers*. McGraw Hill, 7 ed., 1997.

[64] RHODES, M., "Fluidization of particles by fluids," tech. rep., Educational Resources for Particle Technologists, http://www.erpt.org/012Q/rhod-04.htm, 2001.

[65] RITTER, H. L. and DRAKE, L. C., "Pore-size distribution in porous materials. pressure porosimeter and determination of complete macropore size distributions.," *Industrial and Engineering Chemistry, Analytical Edition*, vol. 17, pp. 782–6, 1945.

[66] ROBERTS, D., HARRIS, D., and WALL, T., "On the effects of high pressure and heating rate during coal pyrolysis on char gasification reactivity," *Energy and Fuels*, vol. 17, pp. 887–895, 2003.

[67] ROBERTS, D. G., HARRIS, D. J., and WALL, T. F., "Total pressure effects on chemical reaction rates of chars with o_2, co_2, and h_2o," *Fuel*, vol. 79, pp. 1997–1998, 2000.

[68] SAVIHARJU, K., MOILANEN, A., and VAN HEININGEN, A., "New high-pressure gasification rate data for past pyrolysis of black liquor char," *Journal of Pulp and Paper Science*, vol. 24(7), pp. 231–236, 1998.

[69] SINQUEFIELD, S. A., *Standard Operating Procedure for the IPST Pressurized Entrained Flow Reactor*. IPST, 500 10th Street NW Atlanta, GA 30332-0620, 2 ed., March 2002.

[70] SMITH, J., VAN NESS, H., and ABBOTT, M., *Introduction to Chemical Engineering Thermodynamics*. McGraw Hill, 6th ed., 2001.

[71] SMOOK, G. A., *Handbook for Pulp and Paper Technologists*. Angus Wilde, 2nd ed., 1992.

[72] SRICHAROENCHAIKUL, V., FREDERICK, W., and GRACE, T., "Sulphur species transformations during pyrolysis of kraft black liquor," *Journal of Pulp and Paper Science*, vol. 23(8), pp. J394–J400, 1997.

[73] SRICHAROENCHAIKUL, V., HICKS, A. L., and FREDERICK, W. J., "Carbon and char residue yields from rapid pyrolysis of kraft black liquor," *Bioresource Technology*, vol. 77, pp. 131–138, 2001.

[74] SRICHAROENCHAIKUL, V., PHIMOLMAS, V., FREDERICK, W. J. J., and GRACE, T. M., "Pyrolysis of kraft black liquor: Formation and thermal conversion of volatile products and char," *Journal of Pulp and Paper Science*, vol. 24(2), pp. 43–49, February 1998.

[75] SRICHAROENCHAIKUL, V., "Sulfur species transformations and sulfate reduction during pyrolysis of kraft black liquor," Master's thesis, Oregon State University, 1995.

[76] SRICHAROENCHAIKUL, V., *Fate of Carbon-Containing Compounds From Gasification of Kraft Black Liquor with Subsequent Catalytic Conditioning of Condensible Organics*. PhD thesis, Georgia Institute of Technology, August 2001.

[77] TOUT, B., "New bern black liquors/recovery boiler ash solution," Tech. Rep. 05-0037, Weyerhaeuser Analytical and Testing Services, 32901 Weyerhaeuser Way South Federal Way, WA 98001, January 2005.

[78] VERRILL, C., WHITTY, K., BACKMAN, R., and HUPA, M., "The role of sodium in pressurized black liquor char gasification," Tech. Rep. 93-10, Abo Akademi University, Turku, Finland, 1993.

[79] VERRILL, C. L. and WESSEL, R. A., "Detailed black liquor drop combustion model for predicting fume in kraft recovery boilers," *Tappi Journal*, vol. 81:9, pp. 139–147, September 1998.

[80] VERRILL, C. WESSEL, R., "Sodium loss during black liquor drying and devolatilization - application of modeling results to understanding laboratory data," in *International Chemical Recovery Conference*, vol. B, pp. B89–B103, TAPPI, 1995.

[81] WAG, K. J., FREDERICK, W. J., DAYTON, D. C., and KELLY, S. S., "Characterization of black liquor char gasification using thermogravimetry and molecular beam mass spectrometry," in *AIChE Symposium Series No. 315*, vol. 93, 1997.

[82] WALL, T. F., LIU, G.-s., WU, H.-w., ROBERTS, D. G., BENFELL, K. E., GUPTA, S., LUCAS, J. A., and HARRIS, D. J., "The effects of pressure on coal reactions during pulverised coal combustion and gasification," *Progress in Energy and Combustion Science*, vol. 28, pp. 405–433, 2002.

[83] WALLBERG, O., JONSSON, A.-S., and WIMMERSTEDT, R., "Fractionation and concentration of kraft black liquor lignin with ultrafiltration," *Desalination*, vol. 154, pp. 187–199, 2002.

[84] WEBB, P. A., "A primer on particle sizing by static laser light scattering," in *Micromeritics Technical Workshop Series*, Micromeritics, Fall 2000.

[85] WEBB, P. A., "An introduction to the physical characterization of materials by mercury intrusion porosimetry with emphasis on reduction and presentation of experimental data," tech. rep., Micromeritics Instrument Corporation, Norcross, GA, January 2001.

[86] WESTERVELT, H. H. I., *A Study of the Calcium Complex of the Potassium Salt of Catechol-4-Sulfonate in Aqueous Alkaline Media*. PhD thesis, Institute of Paper Chemistry, Appleton, WI, January 1981.

[87] WHITTY, K., BACKMAN, R., and HUPA, M., "Empirical modeling of black liquor char gasification," Tech. Rep. 93-8, Abo Akademi University, Turku, Finland, 1993.

[88] WHITTY, K., BACKMAN, R., and HUPA, M., "An empirical rate model for black liquor char gasification as a function of gas composition and pressure," in *AIChE Symposium Series*, vol. 90, pp. 73–84, 1994.

[89] WHITTY, K., BACKMAN, R., and HUPA, M., "Influence of char formation conditions on pressurized black liquor gasification rates," *Carbon*, vol. 36(11), pp. 1683–1692, 1998.

[90] WHITTY, K., HUPA, M., and FREDERICK, W., "Gasification of black liquor char with steam at elevated pressures," *Journal of Pulp and Paper Science*, vol. 21(6), pp. J214–J221, 1995.

[91] WHITTY, K. and SANDELIN, K., "The influence of black liqor pyrolysis conditions on characteristics of the resulting char," tech. rep., Abo Akademi University, Turku, Finland, 1994.

[92] WHITTY, K. and VERRILL, C. L., "A historical look at the development of alternative black liquor recovery technologies and the evolution of black liquor gasifier design," in *Black Liquor Colloquium*, (Park City, Utah), May 2003.

[93] WOOD, B. and SANCIER, K., "The mechanism of the catalytic gasification of coal char: A critical review," *Catal. Rev.-Sci. Eng.*, vol. 26(2), pp. 223–279, 1984.

[94] YOUNG, G., "Personal communication," April 2006.

[95] YU, J., HARRIS, D., LUCA, J., ROBERTS, D., WU, H., and WALL, F., "Effect of pressure on char formation during pyrolysis of pulverized coal," *Energy and Fuels*, vol. 18, pp. 1346–1353, 2004.

[96] YUSUF, Z. and CAMERON, J., "Decarbonization reactions between sodium metaborate and sodium carbonate," *Industrial Engineering Chemistry Research*, vol. 43, pp. 8148–8154, 2004.

[97] ZENG, L., *Kraft Black Liquor Gasification and Direct Causticization with TiO_2 in a Fluidized Bed.* PhD thesis, University of New Brunswick, 1997.